Durham E-Theses

The aerodynamics and performance of a cross flow fan

Tuckey, Paul R.

THE AERODYNAMICS AND

PERFORMANCE OF A

CROSS FLOW FAN

by

Paul R. Tuckey B.Sc.

Thesis submitted for the degree of Doctor of Philosohy
in the Faculty of Science, University of Durham.

July, 1983

i

Dedicated to my mother, Mrs. R.M. Tuckey and my father, Mr. C. Tuckey B.Sc., C.Eng. for their persuasion, guidance and encouragement.

CONTENTS

iv

ACKNOWLEDGEMENTS

ABSTRACT

The cross flow fan consists of a cylindrical rotor closed at the ends with a cascade of axial blades around its curved surface. The rotor is mounted in a housing which defines the suction and discharge arcs. The housing extends the full length of the rotor and the throughflow is in a plane at right angles to the rotor axis. This fan is a unique type of turbo-machine which differs significantly from axial flow, centrifugal and mixed flow machines, in that each blade passage experiences a continuosly varying flow each time it makes a revolution through the flow field.

In this thesis, experimental results are presented which describe the internal flow regime of a large cross flow fan of rotor length 1.0 m and outside diameter 0.625 m. Details of the flow field are examined for a range of dimensionless flow coefficient Φ between 0.4 and 0.8, which is taken to be the usual operating range for reasons of efficiency and stability of flow. The measurements are transformed into streamlines for the purpose of illustration and the corresponding variations of a dimensionless total pressure coefficient are also given.

Flow visualization techniques have been applied to a dynamically similar model to a reduced scale of 1:6.25 operating in water and photographs representing the flow have been examined both quantitatively and qualitatively.

A Rankine-type vortex centered near the inner periphery is confirmed but the core was found to remain virtually stationary over the flow range investigated. The total pressure distribution indicates the spatial growth and weakened circulation of the forced vortex core as the flow rate reduces. A depression of total pressure has been identified in a region diametrically opposite the vortex core which intensifies as the flow rate increases.

These data are broadly interpreted and are used to improve a previous theoretical model, in which the location of the vortex is used to define the operating point on the fan characteristic.

NOMENCLATURE

Symbol		Units
a	probe calibration factor (chapter 2)	-
a	factor relating radial vortex location (chapter 4)	-
a to 1	regions of flow (chapter 3)	-
A	Area	m^2
b	blockage factor (4.)	-
b	distance (4.)	m
c	chord length	m
C	Local flow velocity	ms^{-1}
d	deflection (appendix 1)	m
d	distance (chapter 2)	m
D	diameter	m
E	energy dissipation (chapter 4)	W
E	Young's modulus (appendix 1)	Pa
F	centrifugal force	N
g	weight per unit mass	ms^{-2}
h	distance	m
H	Total head	Pa
I	second moment of area	m^4
k'	suction region flow function	
K	constant value	-
1	blade length	m
L	fan length	m
m	mass	kg
m	strength of source and sink	m^2s^{-1}
n	integer	-

4

Symbol		Units
N	rotational speed	rev.s^{-1}
N	blade number (chapter 4)	-
p	pressure	Pa
P	pressure rise	Pa
P	power (chapter 4)	W
q	local flow velocity	ms^{-1}
Q	volume flow rate	m^{3}s^{-1}
r	blade curvature	m
r	radius	m
R	reaction force (appendix 1)	N
R	radius	m
t	blade thickness	m
t	time	s
$\tilde{t}$	total pressure coefficient $= \dfrac{p_t - p_{to}}{\frac{1}{2}\rho U_1^2}$	-
U	blade velocity	ms^{-1}
V	fluid velocity	ms^{-1}
w	distributed force	Nm^{-1}
$\bar{x}$	distance to centroid of area	m
y	deflection	m
z	constant factor	-
α	included angle of blade section	degs
α	location of sink (chapter 4)	degs
α_1	rear wall leading edge location	degs
α_2	vortex wall leading edge location	degs
β	location of source	degs
β	blade angle	degs
γ	$= \rho g$, specific weight	Nm^{-3}
Γ	vortex strength	m^{2}s^{-1}
ε_1	rear wall leading edge clearance	m

5

symbol		units

ε_2 vortex wall leading edge clearance   m

ζ conformal mapping function

η conformal mapping function

η efficiency   -

θ angle   rads

Θ peripheral vortex location   rads

λ arc   rads

μ viscosity of air $kgm^{-1}s^{-1}$

ρ density kgm^{-3}

τ shear stress   Pa

ϕ velocity potential m^2s^{-1}

Φ dimensionless flow coefficient $\simeq \dfrac{Q}{L\,D_2\,U_2}$ -

ψ stream function m^2s^{-1}

Ψ dimensionless pressure coefficient $= \dfrac{P}{\frac{1}{2}\rho\,U_2^2}$ -

ω rotational speed $rads^{-1}$

Subscripts

1   fan inner periphery

2   fan outer periphery

AV   average

$\mathcal{L}$ centre-line

d   discharge

i   fan inner periphery (MOORE)

IN   input

n   normal

o   fan outer periphery (MOORE)

r   radial

s   static

s   suction (MOORE)

t   rear wall leading edge (MOORE)

Symbol

t	total
to	total on fan centre-line
v	vortex
θ	tangential
θ_i	tangential on free/forced vortex boundary

Superscripts

⎯	mean
$\sim$	free vortex
*	rotational flow

CHAPTER ONE

INTRODUCTION

1. INTRODUCTION

1.1 Problems with Cross Flow Fan Development

Although cross flow fans have been designed and built for nearly a century, there still remain ambiguities and a lack of precision in the description of the aerodynamic behaviour of these devices. Many of the difficulties arise from the presence of numerous geometric variables which are deemed to have an influence on performance and even now, optimisation criteria are not universally accepted. Nevertheless, the dominant feature of a cross flow fan (and to a large extent its vertical axis wind turbine counterpart) lies in the inherent unsteady, non-uniform aerodynamics of the rotor. The passage of blades through the vortex core, the reversal of flow direction relative to the blade during one revolution and the presence of highly turbulent flow zones, present problems of extreme difficulty for the analyst.

An account of the historical development of cross flow fans is given by CLAYTON (ref. 5) who additionally compiled a wide range of data in order to improve design guide lines. A more recent study by ALLEN (ref. 1), confirmed by previous research on the aerodynamic facility used for the present investigation, details a fan selection procedure which is included in Chapter 5.

1.2 Early History

The concept of using a paddle wheel to move a fluid probably occurred to MORTIER (ref. 17) who patented the first cross flow fan in the late 19th century. This example of a rudimentary idea giving rise to a new concept, is reflected in the development of the cross flow fan, which may be regarded as a distant relative of the paddle wheel. It is clear to see from Fig.1.1 that MORTIER's patent of 1893 has many features present in modern cross flow fans. However, their use in mine ventilation was short lived, probably because of the increasing use of axial fans which in the form of propellors, had received much attention in the development of powered flight.

A number of designs followed, each tailored to meet a particular industrial application. Notable amongst these was the design by DALIN (ref. 8), patented in 1927 for grain drying; ANDERSON's numerous patents (ref. 2) for industrial air heaters between 1931 and 1933; and the patent by BUCK (ref. 4) for injecting pulverised fuel into furnaces. Again there is no evidence that any of these designs were ever widely employed, probably because of the availability of the more efficient centrifugal blowers at that time.

It is apparent that the main advances in cross flow fan design were initiated by detailed investigations into their behaviour. Professor ACKERAT began such an investigation at the Aerodynamic Institute of the Technical University of Zurich in 1937. His research aroused some

10

Filler Body
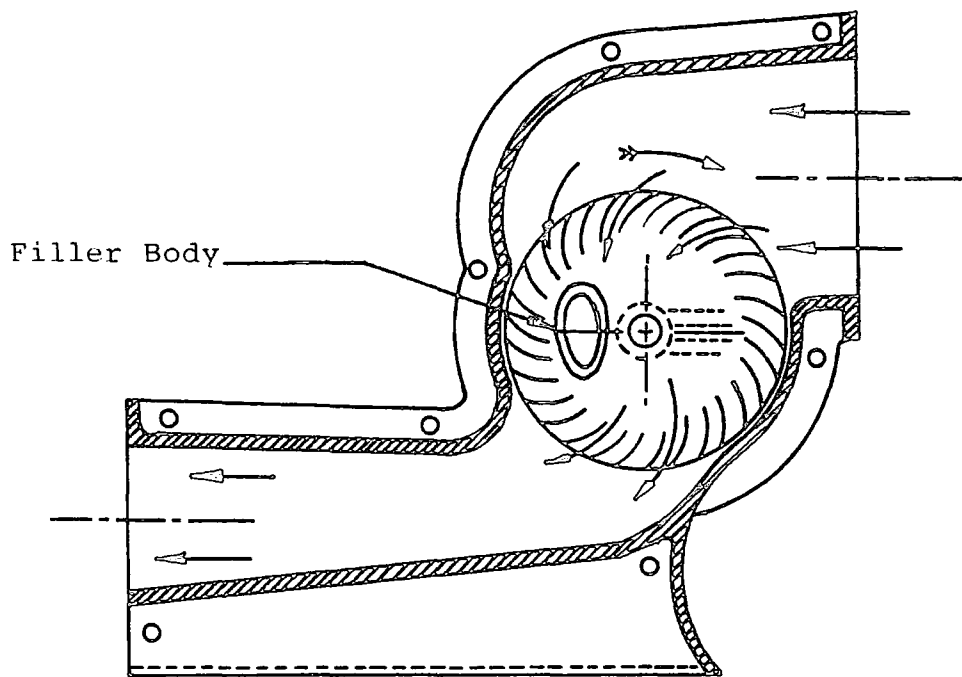
Figure 1.1 MORTIER FAN (U.S. PATENT 507, 445, 1893).
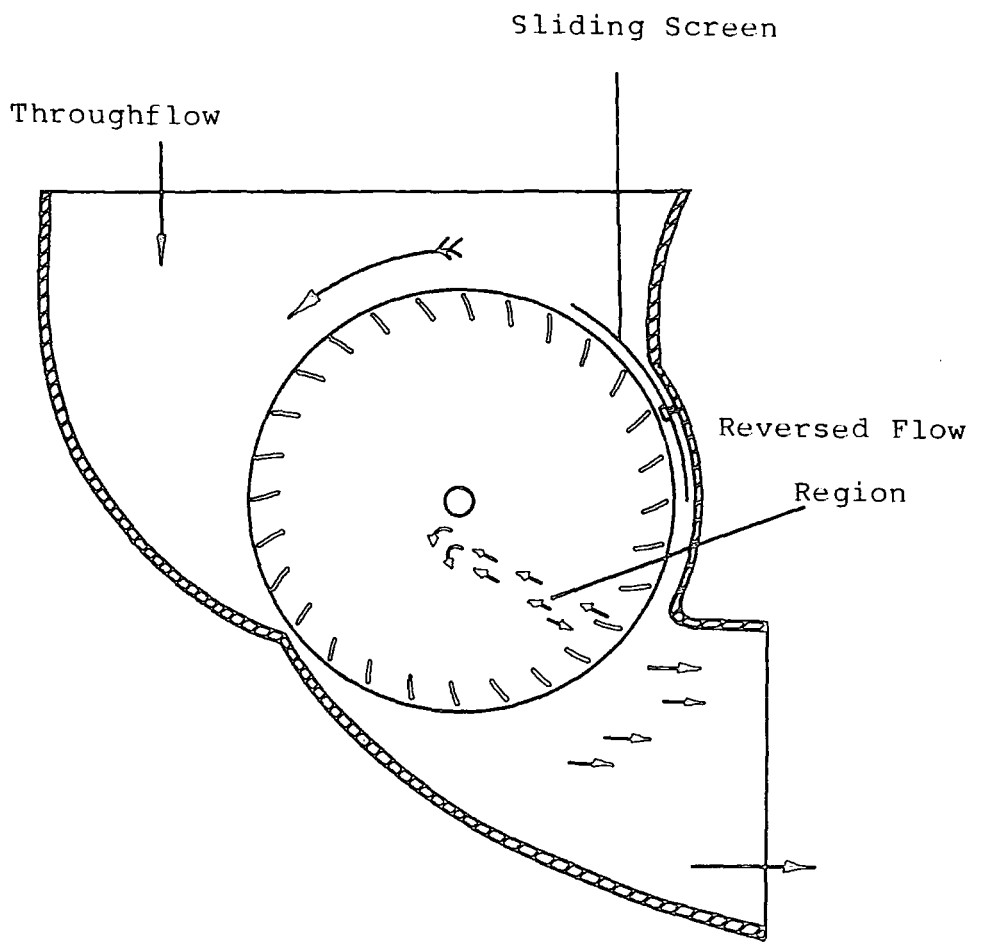
Figure 1.2   ANDERSON LINE FLOW FAN (U.S. PATENT 1, 920, 952)

interest in Swiss industry; notably at Sulzer Brothers of Winterthur who investigated the properties of these machines for applications in air conditioning.

A graduate of the same institute, Dr. DATWYLER , commenced research in 1950 which resulted in patents (ref. 9) which have since been licensed to several countries. In 1959, Dr. COESTER, also of the institute, published a paper (ref. 7) dealing with his research into and the analysis of improved cross flow fans with novel casing geometries.

Sadly, none of these endeavours culminated in the manufacture of a commercial machine and there can be little doubt that it was the research carried out by Dr. ECK in Germany which began the development of the modern cross flow fan.

ECK introduced the term cross flow, in a purely generic sense   , in his research which began in 1950. A design was soon completed comprising a fan having no external casing, relying on an internal body to stabilise the vortex, or indeed to provide a break of symmetry, thus initiating the throughflow. This design was subsequently sold to a West German company, giving these   fans their first practical application since their use in mine ventilation at the turn of the century. ECK's exhaustive text on fans (ref. 10) contains an article on this fan type.

Although a market was created for this novel duct-free fan as a desk top ventilator, the constructional difficulties and the increased manufacture cost prompted further research directed towards the development of a low

Throughflow

Recirculation Pocket

Recirculation

Pocket
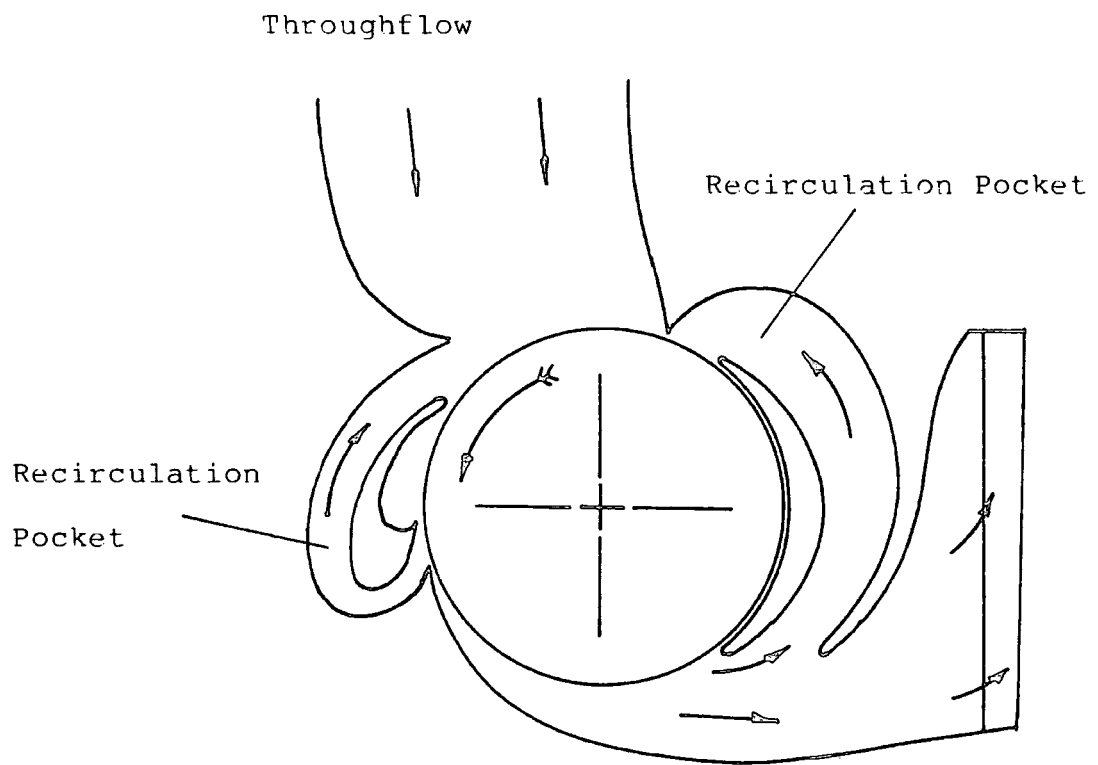
Figure 1.3   IMPROVED COESTER BLOWER

14
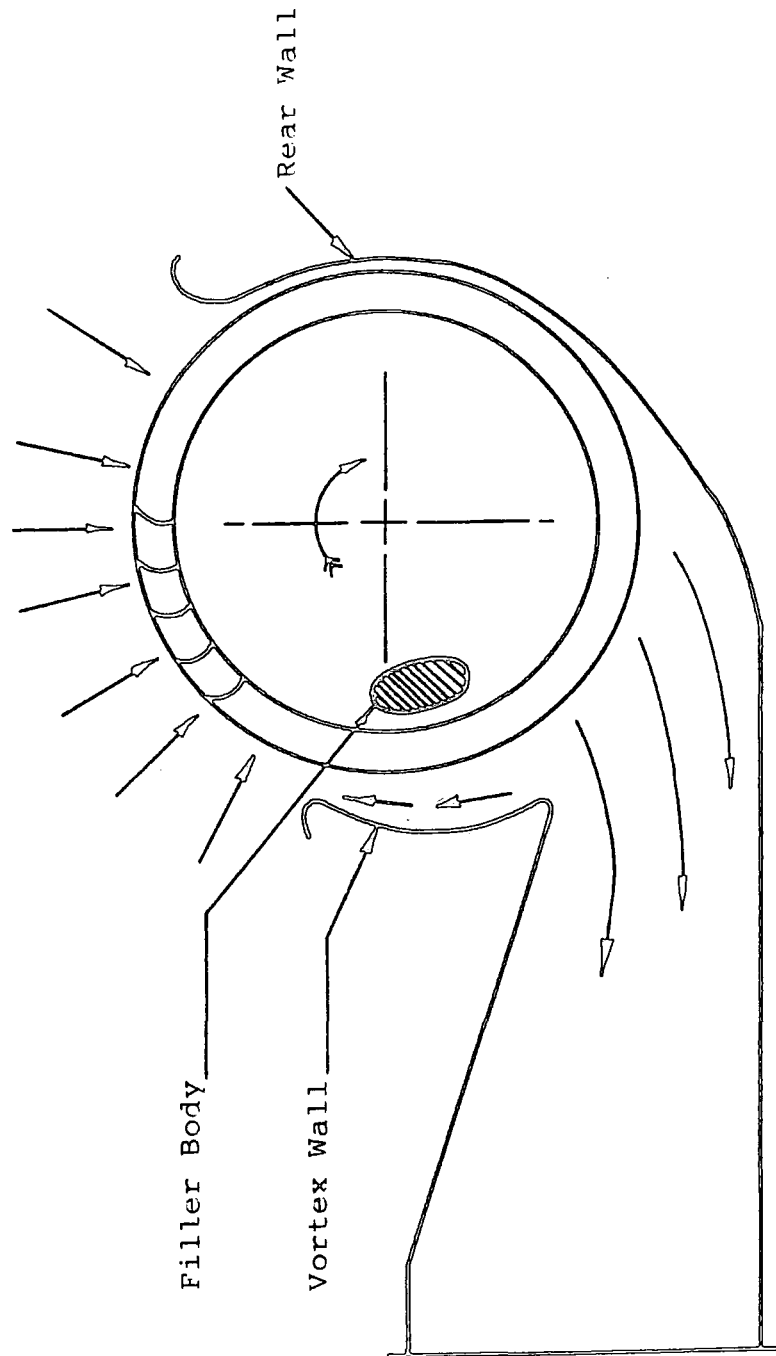
Figure 1.4   ECK CROSS FLOW BLOWER (U.K. PATENT 757, 543)

cost ventilation unit based on the same principle of vortex control. From performance evaluations together with flow visualization studies, ECK determined that the vortex could be controlled by correctly profiling the vortex wall. A running clearance was no longer necessary as he noted that the vortex acted as an aerodynamic seal, preventing a passage between the high pressure side and atmosphere. This had the added benefit of considerable noise reduction.

ECK's design of an efficient cross flow fan, ideal for use in low Reynolds number applications and cheap to manufacture through the absence of internal guide bodies and the larger running clearances, was patented in 1954. Today, this fan is still evident on the small fan market, where they find their predominant application in the air conditioning field.

1.3 Recent History

Since 1960, much of the research has been consolidated by the Japanese. YAMAFUJI (refs.28 and 29) conducted experiments with a small (160mm. o.d.) isolated rotor, in an effectively unbounded fluid contained by a water tank. He was able to show that a stable eccentric vortex could be formed, located close to the inner periphery of the rotor, provided that the Reynolds number (based on the outer blade tip speed and the blade chord) exceeded about 250. Under these circumstances a through flow across the rotor was established. Using the implications of this and further experimental work, an actuator disc theory was developed

(ref. 29). Good agreement with his experiments was found
including some examples in whch simple casing geometries
were specified.

MURATA and NISHIHARA (ref. 18) used a somewhat larger
rotor of 240mm. o.d. and examined the influence of a variety
of casing configurations on the performance. These
generally tended to confirm the optimised values used in
the present research. In ref. 19 , these researchers investi-
gated the shape of the fan performance curves in relation
to controlled adjustments of the casing. In this and the
previous work, the vortex centre formed near the inner
periphery of the rotor and was observed to move away from
the vortex wall and towards the rotor centre line, as the
flow rate was reduced from its maximum value. Further
systematic studies were conducted by MURATA et al (ref. 20)
along similar lines to ECK, where the effects of guide
vanes within the rotor which encircled the vortex region,
were examined.

1.4 The Present Research

At present, the field of applications of the cross flow
fan in diameters of up to 65mm. has been consolidated but
advances in industrial size has been slow. This is because
royalty income is largely dependent on total turnover and
as such, the mass market has received much more attention
by researchers and licensing companies than possible indus-
trial developments. Also, the tooling and manufacturing
costs of larger machines would be relatively high.

17

For these reasons, among others, previous workers
have tended to concentrate research on quite small rotors
(i.e. less than 300mm o.d.) but there has been some evi-
dence to suggest that large rotors may behave differently
(ref. 12). In order to clarify some of the areas of doubt
concerning the aerodynamics of large cross flow machines,
an experimental and theoretical research programme has been
undertaken. Quantitative data were obtained from a large
rotor previously installed in a purpose-built wind tunnel
(Chapter 2) and also from a smaller scale rotor placed in
a water tank (Chapter 3). This latter facility also all-
owed the adoption of reliable flow visualization techniques.
The theoretical study (Chapter 4) was aimed principally
at improving the approach adopted by **IKEGAMI** and **MURATA**
(ref. 13).

CHAPTER TWO

THE AERODYNAMIC FACILITY

"No one is competent to predict things about absolute space and absolute motion; they are pure things of thought, pure mental constructs that cannot be produced by experience".

<div align="right">Ernst Mach 1838-1916</div>

2. AERODYNAMIC FACILITY

2.1 Introduction

The need for a straight-through, open-circuit wind tunnel with a conventional test section led to the specification of a cross flow fan as the primary source of air supply. It was also possible to investigate the aerodynamic performance of the fan itself. A side section of the complete rig is shown in Fig.2.1. This rig was designed as part of a previous research project by HAINES and reported in ref.12.

The requirements for the wind tunnel test section indicated that the fan needed to supply air at a flow rate of $10m^3 s^{-1}$ and develop a static pressure rise of 1kPa. HAINES examined the previous data and showed that a value of the flow coefficient $\Phi = 0.6$* would correspond to optimum efficiency and approximately maximum static pressure coefficient $\Psi_s = 2.2$* and also result in a delivery flow reasonably free from pulsation i.e. a stable flow. These considerations led to the following rotor parameters;

    a) length L = 1.0m,

    b) outside diameter D_2 = 0.625m and

    c) rotational speed N = 6.67 rev.s^{-1}.

2.2 Rotor Geometry

The main geometric parameters of a cross flow fan rotor

* see notation

Rotor

Belt Drive

Outlet Duct

Diffuser

Screens

Contraction Section

Test Section

Drive Motor

2.0m

7.0m
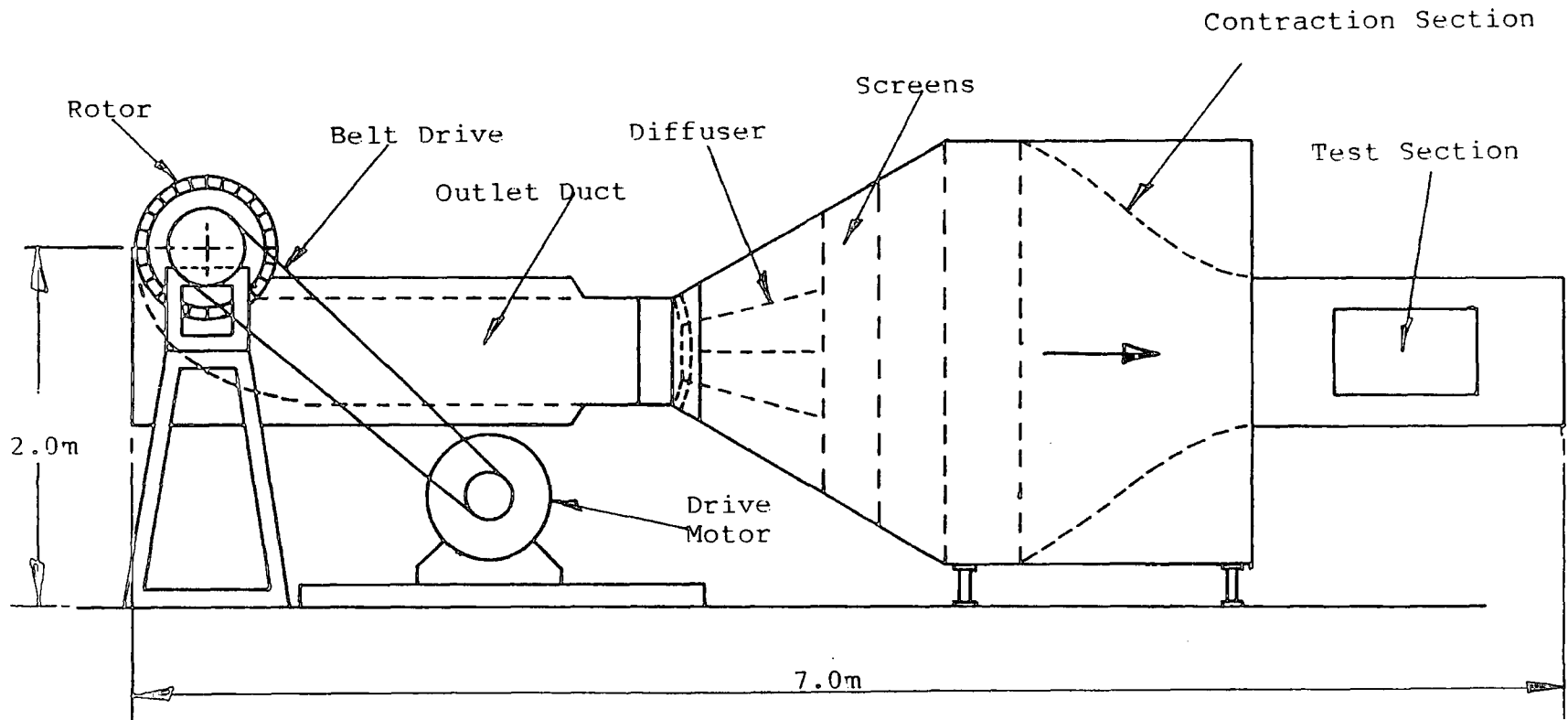
Figure 2.1   LAYOUT OF THE AERODYNAMIC TEST RIG

are illustrated in Fig. 2.2. Numerical values of these parameters for the rotor tested are summarized in Table 2.1. This design was a geometric scaling of a previous smaller fan that had given good results and was itself a combination of the best designs as indicated from the results of PORTER and MARKLAND (ref. 23) and PRESZLER and LAJOS (ref. 24). Generally, a change in the details of the impeller geometry was found to have a far smaller effect on performance than a change in the geometry of the surrounding casing.

2.2.1 The Number of Blades

The number of blades appears to be of secondary importance with the final choice resulting from a compromise between frictional losses and the cascade effect on flow deflection. Torsional and bending rigidity together with the mid-span blade deflection need careful consideration, the latter parameter being dealt with in Appendix 1. Past researchers have had a preference for rotors with between 18 and 36 blades. Therefore, the rotor tested has 24 identical, forward curved blades, equally spaced round the circumference of the swept-cylindrical area.

2.2.2 Blade angles β_1 and β_2

Using the continuity and momentum equations, it was shown by ECK (ref. 10) that β_1 should be 90° although little effect of changes in this angle over the range $60^\circ - 100^\circ$

Table 2.1

Rotor Geometry

Blade angles; $\beta_1 = 90^O$, $\beta_2 = 26^O$

Blade profile; circular arc

Number of blades; N = 24

Diameter ratio; $D_1/D_2 = 0.78$

Length to Diameter ratio; $L/D_2 = 1.6$

23
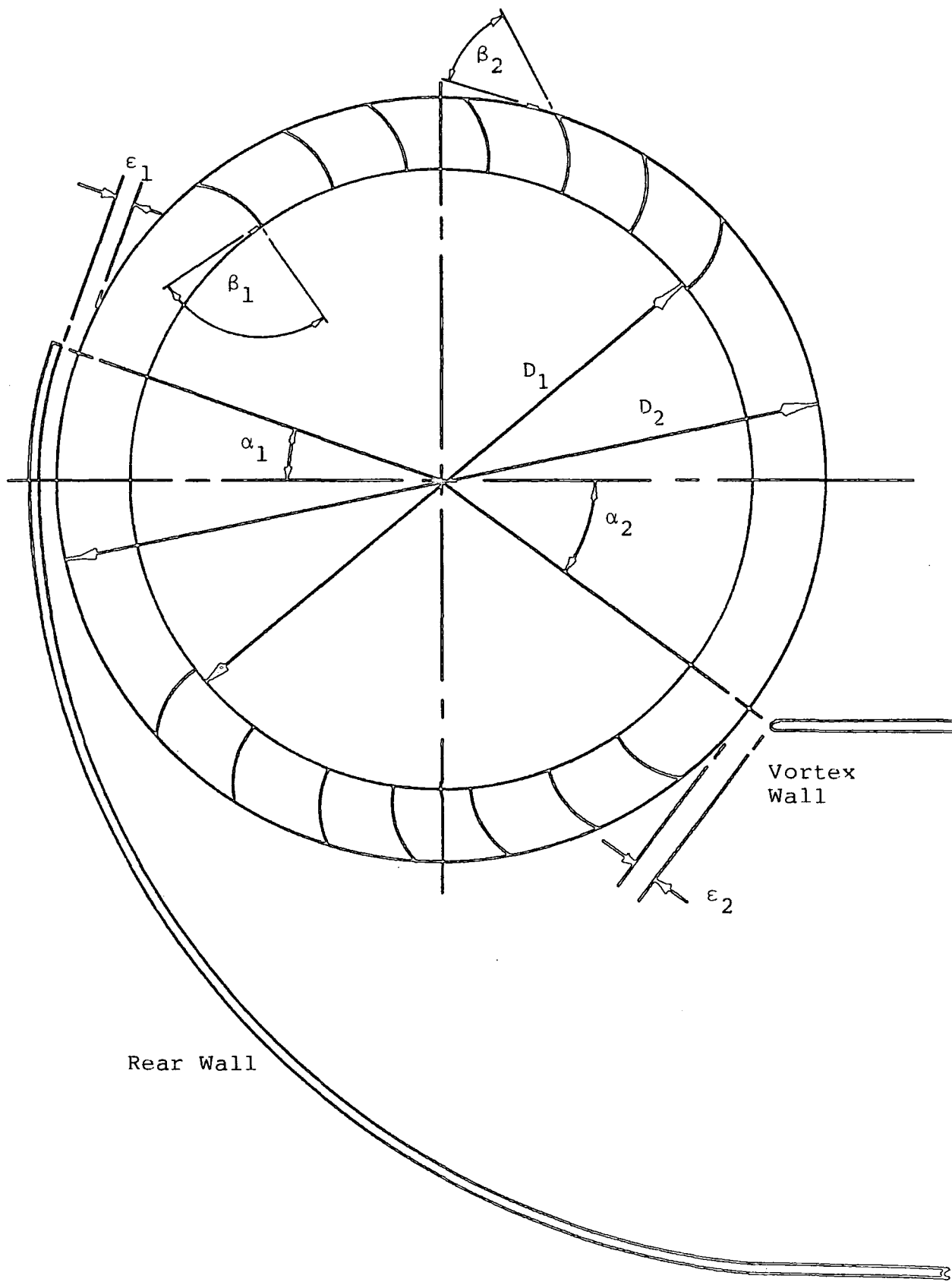
Figure 2.2   GEOMETRY OF THE CROSS FLOW FAN

is usually observed. By contrast, the value of the outer blade angle, β_2 has been optimised on the basis of measurements alone. IKEGAMI and MURATA (ref. 14) and PRESZLER and LAJOS (ref. 24) have exhaustively examined this parameter and it is generally considered that β_2 should be greater than 22° for stability with values around 26° representing an optimum.

The blade profile generally chosen is a circular arc camber, since each blade experiences flow reversal on passing from the suction to the discharge region. There may be a slight advantage in profiling the blades to suit the flow present at either the first or second pass (emerging from the work of MOORE (ref. 16)) but it was felt that any attempt to add a variable thickness profile to the blades was unlikely to improve performance or reveal any otherwise unseen flow behaviour. The constructional complexity would also be increased.

The rotor blades were therefore of constant cross-section and rounded at the leading and trailing edges with $\beta_1 = 90°$ and $\beta_2 = 26°$.

2.2.3 The Diameter Ratio, D_1/D_2

Experimental investigations have been performed to examine the effect of the diameter ratio on the performance of cross flow rotors (refs. 14 and 24) with general agreement between researchers. This parameter does not appear to be a critical parameter within the range of 0.70

to 0.85 and an average value of 0.80 was accepted for the tested rotor.

2.2.4   The Length to Diameter Ratio, L/D_2

The possibility of increasing the flow rate linearly with increase of rotor length (at a given rotational speed) is a main feature of the cross flow fan. There are limit- ations to this however, owing to structural considerations (torsional rigidity in long rotors) and the tendency for the line vortex to segment into shorter line vortices with a consequent deterioraton in overall performance. When this occurs, the fan behaves as a number of fans operating in parallel. Alternatively, if the rotor is too short, then significant secondary flows develop due to boundary layer accumulation on the end plates of the rotor and these can grossly distort the flow through the rotor and at the discharge periphery.

However, these effects have been shown to only slightly reduce the performance and for many applications are ignored, but as the internal flow was to be examined, an average value for this parameter of 1.6 was selected.

2.2.5   The Motor Drive and Drive Shaft

Each end of the rotor is blanked-off by plates which carry the bearings and housings for fixing to the main support frame (see Fig. 2.3). For structural reasons, a central through-shaft was employed on many of the early

Figure 2.3 DETAILS OF THE ROTOR

1000

Trunion Bearing

Support Gantry

Drive End
Pulley

Stationary Perspex
Double Window

334

548 p.c.d

658

Non Drive End Plate

Dimensions in mm

Drive End Plate
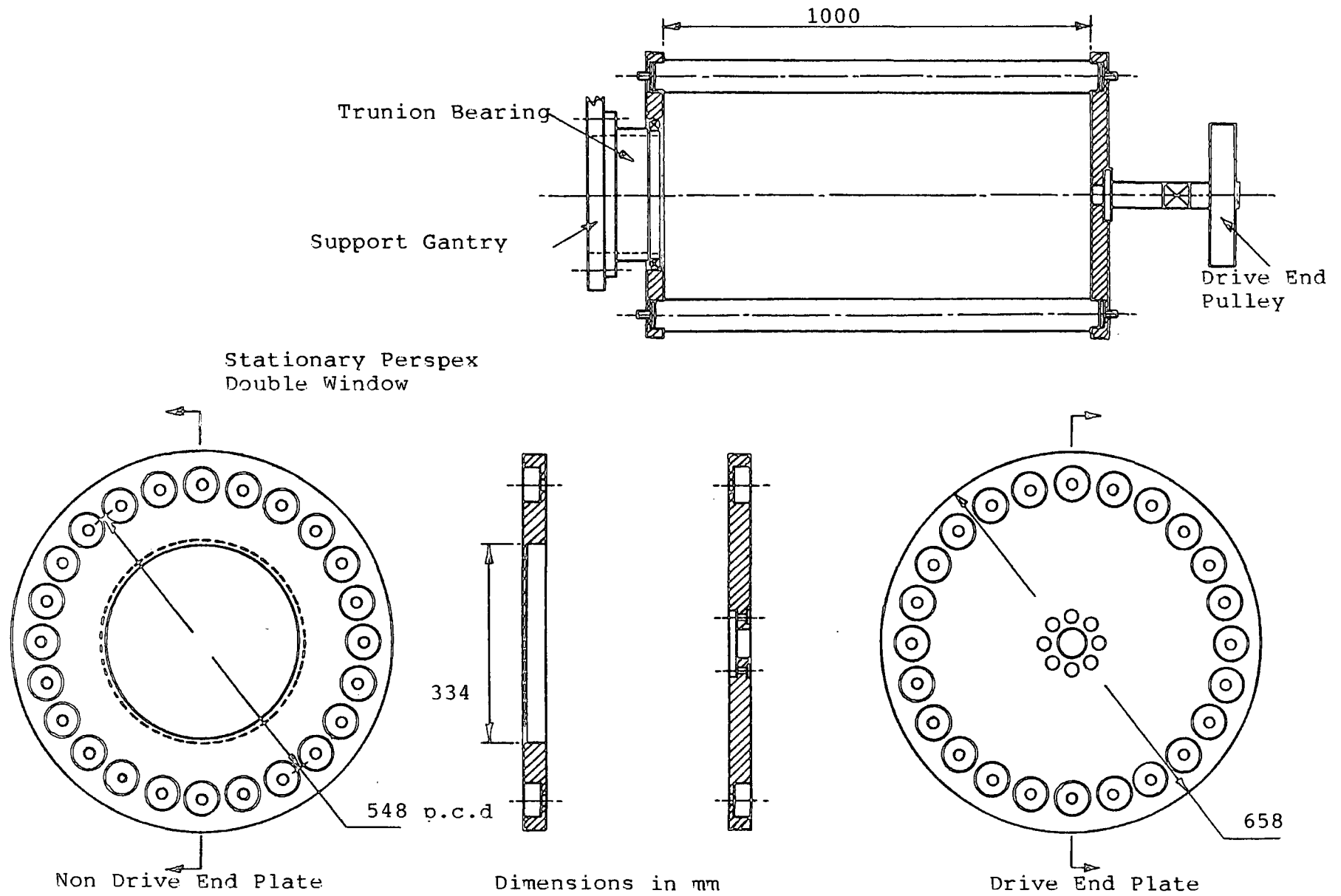
cross flow fans. Subsequent tests by YAMAFUJI (ref. 28)
showed that large reductions in pressure ratio and effi-
ciency would occur, mainly because of the wake generated
by the internal shaft. Modern units dispense with a
central shaft and rely on the blades and occasionally
diametral plates or struts at mid-span for torsional
rigidity.

The drive-end   end plate includes a hollow stub
shaft containing a strain gauge system for input power meas-
urements. The non-drive end end plate is annular and
supported on the framework by a trunnion bearing. This was
to enable measuring probes to be inserted into the fan
interior, for subsequent flow investigations. The drive to
the rotor is from a 50 h.p., 440 volt, 3 phase Schrager
motor using a belt and pulley system. The rotor speed is
variable between 5 and 16 rev. s^{-1} and could be controlled
to within one per cent of that selected.

2.2.6 Safety Cage

For safety reasons, a cage is positioned around the
rotor at a distance of 600mm. from the blades. During
commissioning, inlet velocity readings were taken to deter-
mine the mesh open area required to minimise the pressure
drop (this being proportional to the square of the inlet
velocity). A mesh open area of 80% was chosen which was
attached to an aluminium framework hinged on either side for
ease of removal.

2.3 The Fan Casing Geometry

2.3.1 The Vortex Wall

After the discovery of the line vortex by Dr. Bruno
ECK (ref. 10), much emphasis was placed on stabilising the
throughflow by control of the vortex. This was evident
in his designs where a return flow path was incorporated
in the vortex wall to stabilise and locate the vortex.
Also, under normal operating conditions, the vortex would
provide an aerodynamic seal preventing flow between the
high pressure and suction regions. Based on this, a small
running clearance was no longer necessary. By increasing
this clearance, the sound generated at the vortex wall
edge (mainly at multiples of the blade passing frequency)
could be considerably reduced.

COESTER (ref. 7) paid much attention to the vortex
wall geometry following his analytical study (see Chapter
4). Again, a recirculating path was employed generating
a jet of air with raised total pressure, which was intro-
duced to the rotor just prior to the blades passing from
the vortex wall to the intake region. This addition
tended to stabilise the vortex and a much improved
pressure at low flow rates was produced.

To obtain a more uniform velocity profile at the exit
of the rotor, COESTER used a solid body as an integral
part of the vortex wall, optimising the recirculating
flow. Satisfactory results were then achieved when
employing a diffuser for pressure recovery.

The problems with vortex walls having recirculating
pockets is twofold;

(i) the tendency to encourage a large proportion of the
throughflow to recirculate reducing, by this proportion,
the total efficiency, and

(ii) extending the vortex wall in a peripheral manner tends
to reduce the flow rate by acting as an arcuate damper.

ECK made comment on point (i) by suggesting that over
one-half of the total throughflow could be affected by
recirculation. TRAMPOSCH (ref. 26) compared an ECK type
vortex wall with a simple straight edged wall and found
the latter to give considerable improvement in performance.
Both PORTER and MARKLAND (ref. 23) and IKEGAMI and MURATA
(ref. 14) repeated the tests of TRAMPOSCH and clearly
showed optimum performance was achieved with a straight
edged vortex wall.

Experimental studies by IKEGAMI and MURATA were also
aimed at optimising the position of the vortex wall leading
edge (α_2). Their tests indicated that a value of $\alpha_2 = 36^\circ$ gave the best performance. PRESZLER and LAJOS (ref.
24) defined this position by referring to the inlet to
outlet arc ratio. By taking the rear wall leading edge as
level with the rotor axis ($\alpha_1 = 0^\circ$), their optimum of 1.5
for the ratio confirms the result of IKEGAMI and MURATA.
Tests were therefore carried out with the optimum geometry
of $\alpha_2 = 36^\circ$, as also confirmed by HOLGATE and HAINES (ref.
12).

Little emphasis has been placed on the effect on the
performance of the clearance between the vortex wall leading

edge and the blades, since ECK suggested the existence of the aerodynamic seal. IKEGAMI and MURATA followed this by showing performance and efficiency could be increased by reducing the clearance below $e_2/D_2 = 3\%$, with the associated increase in noise generation.

The original research pursued by HOLGATE and HAINES (ref.12), indicated a trade-off between the performance and efficiency for clearances below 5%. Following this earlier controversy surrounding the function and geometry of the vortex wall, there now seems little doubt that a simple straight wall with a rounded leading edge produces good fan performance and an acceptable level of noise.

For the aerodynamic rig tested the vortex wall followed the above recommendations with $\alpha_2 = 36^\circ$ and $e_2/D_2 = 4\%$.

2.3.1.1 Stiffening of the Vortex Wall Leading Edge

From original tests, the vortex wall was observed to vibrate violently, at low flow rates i.e. high throttling, because of the relatively long unsupported span. These unwanted vibrations were successfully removed by the addition of a 25° stiffening wedge. However, subsequent tests showed the wedge to have a small effect on the performance; acting primarily as an arcuate damper. More important, the internal flow field was significantly distorted by the wake produced by this obstruction, in what is known to be a high velocity region of the suction arc. For this reason, the stiffening wedge was removed and is not recommended for flow rates above $\Phi = 0.4$.

31

2.3.2 The Rear Wall

While much energy was being expended on the correct design of the vortex wall (refs.7 and 10), the rear wall was considered as simply the second side of the casing, employed to contain the throughflow. Only recently has the importance of the rear wall's vortex stabilising influence been fully appreciated. ECK and COESTER produced a design based on sound fluid dynamic principles. Assuming potential flow within the rotor, they showed that for constant peripheral velocity, the fluid radial velocity followed a tangent law.

The rear wall designed by DÄTWYLER (ref. 9⁻) was created to allow the vortex mobility so that it could find a stable location. He compared the improved performance with that of ECK and attributed the improvement to the new rear wall. However, the improvement was almost certainly due to his use of a straight edged vortex wall.

The position of the leading edge of the rear wall, α_1, has also been exhaustively examined. Experiments by IKEGAMI and MURATA, using a circular arc rear wall, found the optimum position to be diametrically opposite the leading edge of the vortex wall. They explain this as being some influence of symmetry. Hence, since the vortex wall was optimised at $\alpha_2 = 36^{\circ}$, then the position of the rear wall should be identical, $\alpha_1 = 36^{\circ}$. PORTER and MARKLAND showed clearly that a logarithmic rear wall shape gave acceptable levels of performance and efficiency and after repeating the tests of IKEGAMI and MURATA, the

positioning of the rear wall leading edge at $\alpha_1 = 30^O$, seemed to agree with their findings.

HOLGATE and HAINES found that diffusion became too great when a logarithmic spiral rear wall was used with its leading edge diametrically opposite the leading edge of the vortex wall, leading to flow separation and reversal. To combat this problem, a logarithmic spiral was developed from the leading edge at $\alpha_1 = 0^O$ but with a circumferential extension attached to the leading edge extending forwards to $\alpha_1 = 20^O$. They also showed the profound effect of the rear wall clearance on the performance and the stability of the flow in the outlet duct, and suggested a value between 3% and 5% of the rotor diameter should give optimum conditions.

For the aerodynamic rig tested, the rear wall followed the above recommendations with a logarithmic rear wall with a circumferential extension from $\alpha_1 = 0^0$ to 20° at a clearance of $e_1/D_2 = 0.05$.

In conclusion to these sections on vortex and rear wall design, it has been found that some researchers choose to include the parameter inflow to outflow arc. Most prefer a one-to-one ratio but a close examination of the history of this parameter seems confusing;

(i) ECK preferred a ratio greater than one,

(ii) DÄTWYLER preferred a ratio less than one,

(iii) PRESZLER and LAJOS selected a value of 1.5 and

(iv) PORTER and MARKLAND agreed with IKEGAMI and MURATA concluding that this parameter was of secondary importance in cross flow fan design.

In the sense of a fluid flowing into and out of the rotor, this parameter is quite meaningless. Flow visualization studies described in Chapter 3, show how the inflow and outflow arcs are largely dependent on the flow rate and should not be confused with the geometrical arcs, although some dependency is present.

2.3.3 Outlet Duct Diffuser

Like many early experimenters, ECK and PORTER and MARKLAND use a diffusing section attached to the fan outlet duct, and maintain that the efficiency of the fan stands or falls by the effectiveness of such a diffuser. The effectiveness of a diffuser is greatly reduced by the presence of a strongly non-uniform velocity and pressure distribution at its entrance. As the vortex lies partly in the outlet duct, the velocity profile at the fan discharge is far from uniform. COESTER recognised this fact incorporating recirculation pockets, producing a more uniform outlet velocity profile before entry to a short diffusing section. DÄTWYLER used no diffusing section as he accepted that the diffusion of the flow takes place mainly in the region enclosed by the rear wall which acts as a volute, plus the natural diffusion due to the vortex location.

Investigations by TRAMPOSCH indicated that only minor improvements could be achieved by using a diffuser and similar tests by PRESZLER and LAJOS showed that although the static pressure did increase, it did so at the expense

of the total pressure and the efficiency, especially in the normal working range of the fan (greater than $\Phi = 0.5$).

For these reasons, the surrounding ductwork of the fan tested (as shown in Fig. 2.4) contains no diffuser and has a simple parallel sided outlet duct.

2.3.4 Wind Tunnel Working Section Outlet Diffuser

The air from the test section was originally allowed to pass to atmosphere by means of a sudden expansion. The maximum flow rate through the fan was reduced because of the considerable pressure drop experienced. A pyramid diffuser with a cone angle of 14° and an area ratio of two positioned at the outlet of the working section had the effect of increasing the flow rate to in excess of $\Phi = 1.0$. A simple iris shutter system attached to the downstream end of the diffuser allowed the flow rate to be set with fine resolution to better than 1%, without unduly affecting the velocity profile in the working section.

2.3.5 Pressure Tappings.

Four symmetrically placed pressure tappings holes with brass inserts were located in the casing in a plane three rotor diameters downstream from the leading edge of the vortex wall. These were connected to a manifold and the mean response used to calculate the static pressure rise from the fan and hence the static pressure coefficient ψ_s.
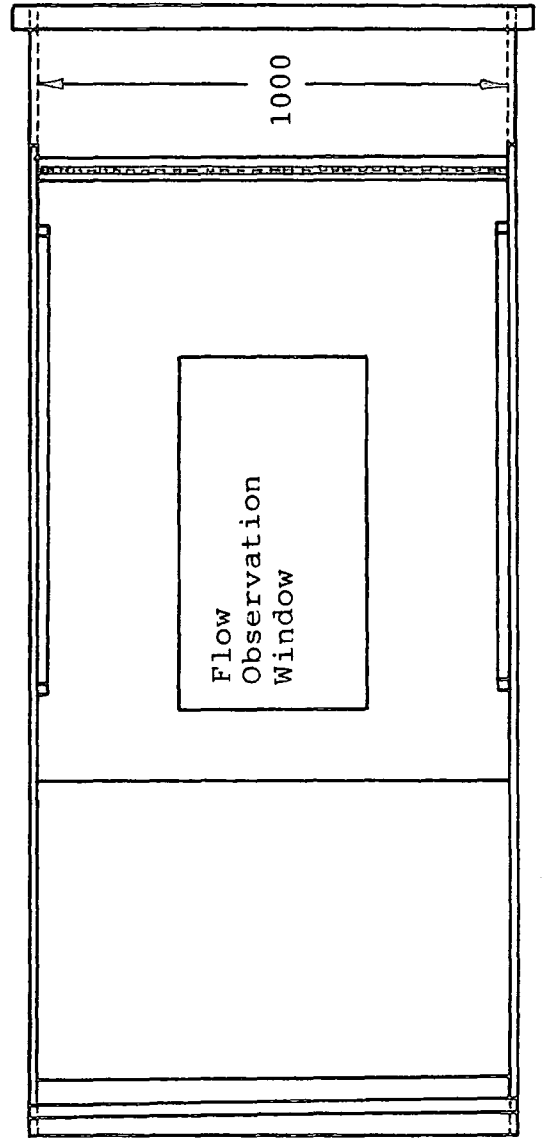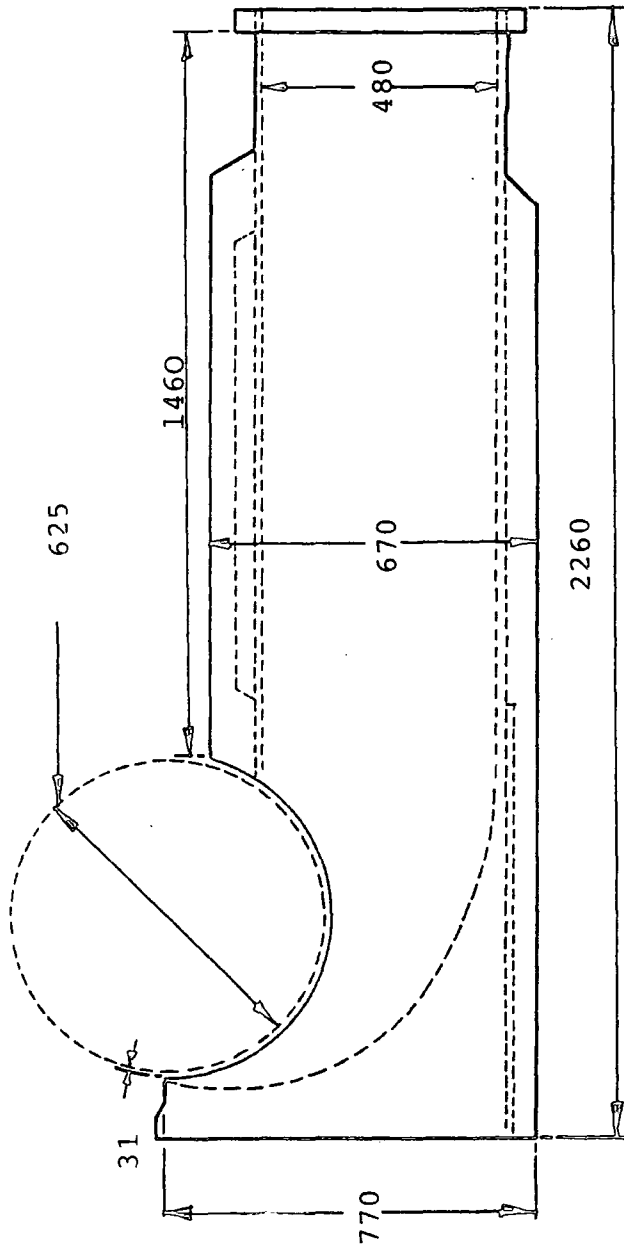
Figure 2.4   DETAILS OF THE FAN CASING

The test section of the wind tunnel had been previously calibrated in terms of the flow rate related to the centre line velocity, from which the flow coefficient Φ and the total pressure coefficient Ψ_t was easily determined.

The performance curves for the fan tested (at a rotational speed of 6.67 rev. s^{-1}) in terms of these parameters are shown in Fig. 2.5. It can be seen that the design requirement is met and subsequent data will be related to these curves.

2.4   The Aerodynamic Measurements

The experiments performed on the aerodynamic facility previously described detailed the internal flow regime of a large cross flow fan. Measurements of velocity, direction and total pressure were transformed into streamlines for the purpose of illustration together with corresponding variations of a total pressure coefficient $\tilde{t}$, throughout the flow field.

From these results, general conclusions were made which assisted with the development of an improved theoretical model (see Chapter 4).

2.4.1   Determination of Volume Flow Rate

The centre line velocity in the wind tunnel working section was calibrated by HOLGATE and HAINES (ref. 12) against the velocity obtained from a 26 point traverse across the fan exit ductwork at a section three rotor diameters downstream from the vortex wall leading edge (in
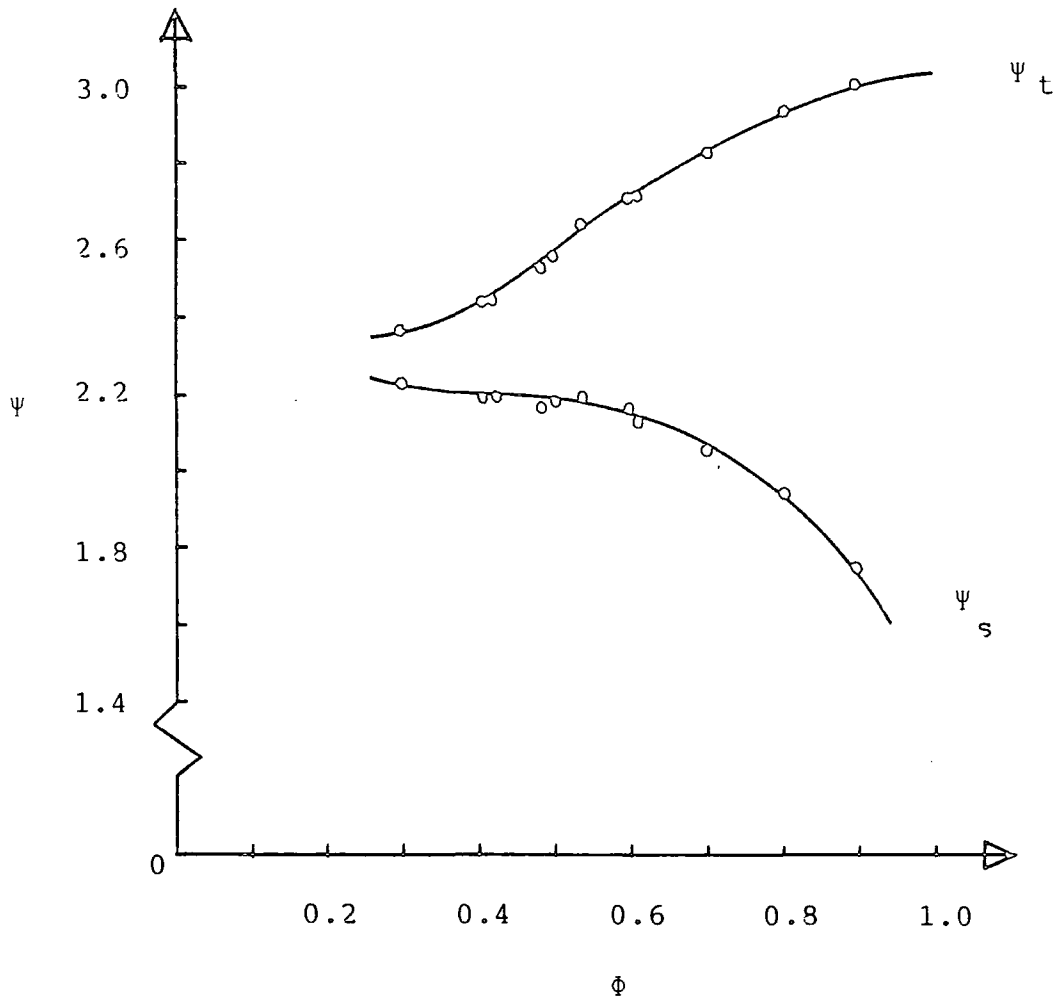
Figure 2.5 FAN PERFORMANCE CURVES

the same plane as the static pressure tapping ring). This
is a reduced form of the B.S. 1943, 48 point traverse.
This was checked using the pyramid diffuser previously
described to achieve different flowrates. The velocity
profile across the working section was maintained during
this calibration to ensure that no distortion occurred due
to the throttling hardware downstream.

The flowrate was determined from a single centre-line
reading in the working section and using the calibration
chart (see Fig.2.6) the flowrate was expressed in dimension-
less form.

$$\Phi = \frac{Q}{L \ D_2 \ U_2} \ ,$$

where Q = flow volume flowrate $m^3 s^{-1}$,

L = rotor length m,

D_2 = rotor outer diameter m and

U_2 = outer periphery blade tip speed ms^{-1};

A least squares fit of the data points from the cali-
bration chart yielded

$$V_{AV} = 0.644 \ V_{\textcircled{L}}$$

which is very close to the result obtained by taking
the ratio of the working section area to the fan outlet
duct area of 0.64.

2.4.2   Determination of Pressure Rise

The static pressure rise across the fan was determined
from a ring of four pressure tappings located one on each
side of the exit ductwork at a section three rotor
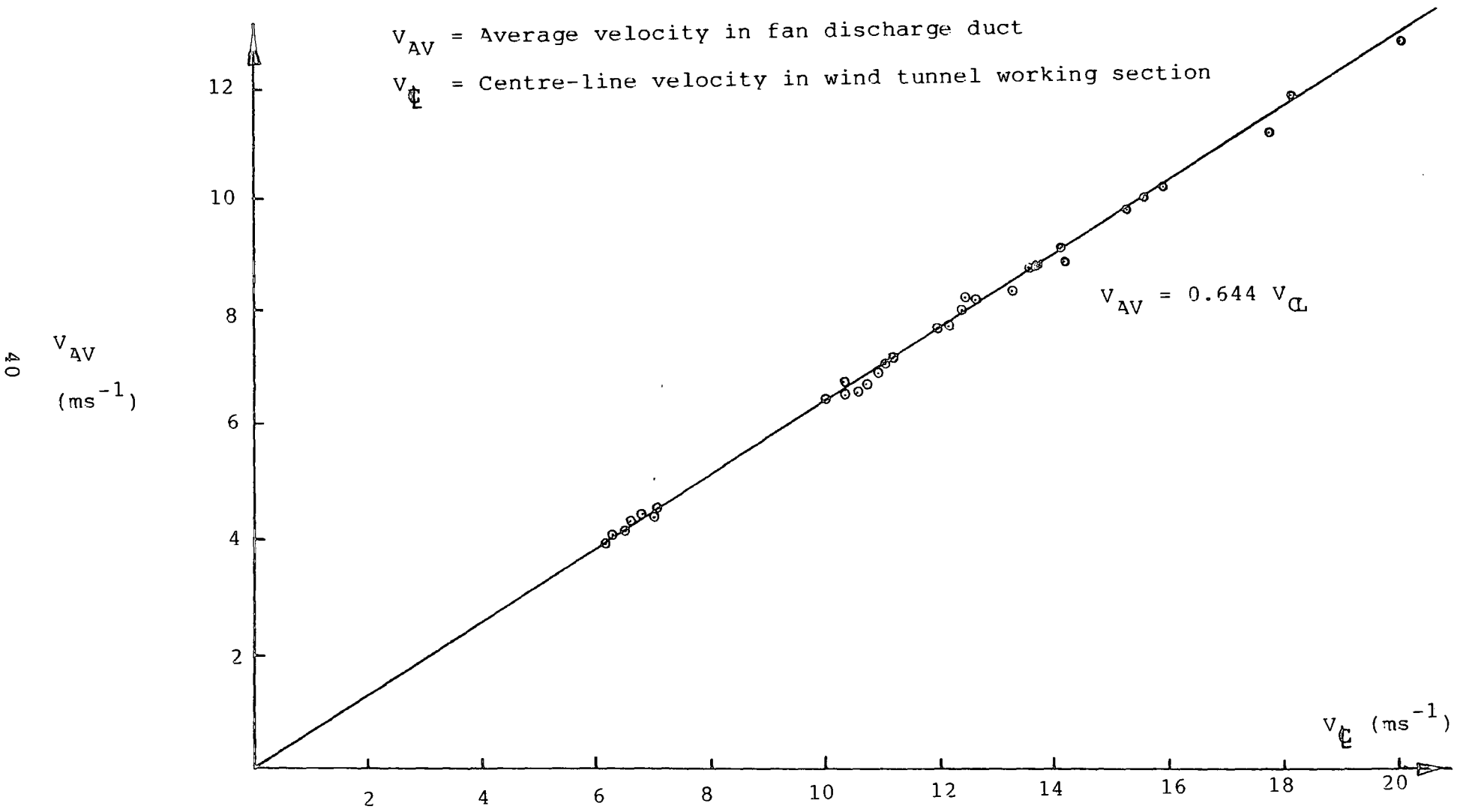
Figure 2.6   FLOW RATE CALIBRATION

diameters downstream from the vortex wall leading edge.
The tappings were connected to a manifold from which a
central connection provided the mean pressure response at
this section. The velocity profile at this section
showed to be substantially uniform indicating a uniform
pressure variation. The static pressure rise was expressed
in dimensionless form.

$$\Psi_s = \frac{p_s}{\frac{1}{2} \rho U_2^2}$$

where p_s = static pressure rise P_a,

ρ = density of air kgm^{-3},

U_2 = outer periphery blade tip speed ms^{-1}.

By measuring the velocity in the working section and
relating this to the velocity in the fan exit duct, the
velocity pressure $\frac{1}{2} \rho V_{AV}^2$ was calculated and added
dimensionlessly to the static pressure coefficient, yielding
the total pressure coefficient Ψ_t.

2.4.3 Determination of Power Input and Efficiency

Although efficiency was not a prime parameter in this
research, the facility for its assessment was available.
The power input to the fan was determined by measurement
of the torque on the drive-end shaft between the drive
pulley and the end plate. Two pairs of strain gauges
bonded diametrically opposite each other (eliminating
bending and axial strains) and connected via slip rings
to a full wheatstone bridge, produced microstrain signals.
The power input was easily determined from

$$P_{IN} = \text{torque x speed}$$

and the efficiency calculated from

$$\eta_t = \frac{Q \, P_t}{\text{Torque x speed}}$$

2.4.4   The Rotor Rotational Speed

A bakelite disc containing sixty symmetrically spaced soft iron segments was mounted on the drive-end shaft. A magnetic transducer fixed to the support frame and held in close proximity to the periphery of the disc, produced a direct reading in revolutions per minute on a standard timer-counter unit. The control circuity associated with the Schrager motor, ensured the rotor speed did not drift by more than one per cent from that selected.

2.4.5   Instrumentation

2.4.5.1   Cranked Three-hole Probe

A purpose built probe was designed to examine the internal flow regime of the cross flow fan, for two reasons. First, the access to the interior from the non-drive-end prevented measurements close to the blade row and second, the conventional hypodermic tubing considerably reduced the probe response. The designed probe had a variable geometry 'Z' drive with one arm concentric with the shaft of the fan, so that any radial location at mid-span could be adopted. Yawing was affected through a series of precision bevel gears attached to the hollow shafts which carried the

pressure tubes. Flexible tubing was used where direction changes occurred through the bevel gears.

The probe head was manufactured using a 'nest' of five hypodermic tubes arranged so that three of the internal tubes formed the conventional geometry for a yaw probe, i.e. the angle between the central and outer tubes being 40°. To combat the problems associated with drilling the 0.3mm diameter pressure taps, a section of the probe head was milled revealing the three tubes. This was filled with transparent resin creating a window and after allowing to set, the holes were drilled at the required angles without the drill slipping on the cylindrical surface. A short distance away from the head, the nest of tubes was connected to three large bore tubes for the remainder of the run through the probe unit. This considerably improved the pressure response rate. The probe is shown in Fig.2.7 with its calibration curves presented in Fig. 2.8.

2.4.5.2   The Traversing Mechanism

The traversing equipment was mounted adjacent to the opening provided by the non-drive end plate. This cons- isted of a bezel mounted on a slide which was in turn atta- ched to a second bezel aligned with the centre-line of the rotor, as illustrated in Fig. 2.9.

The probe was positioned within the rotor and a key on the probe body was allowed to travel in a slot milled in a pair of circular perspex windows which sealed the fan interior from atmosphere. A key on the probe shaft ensured
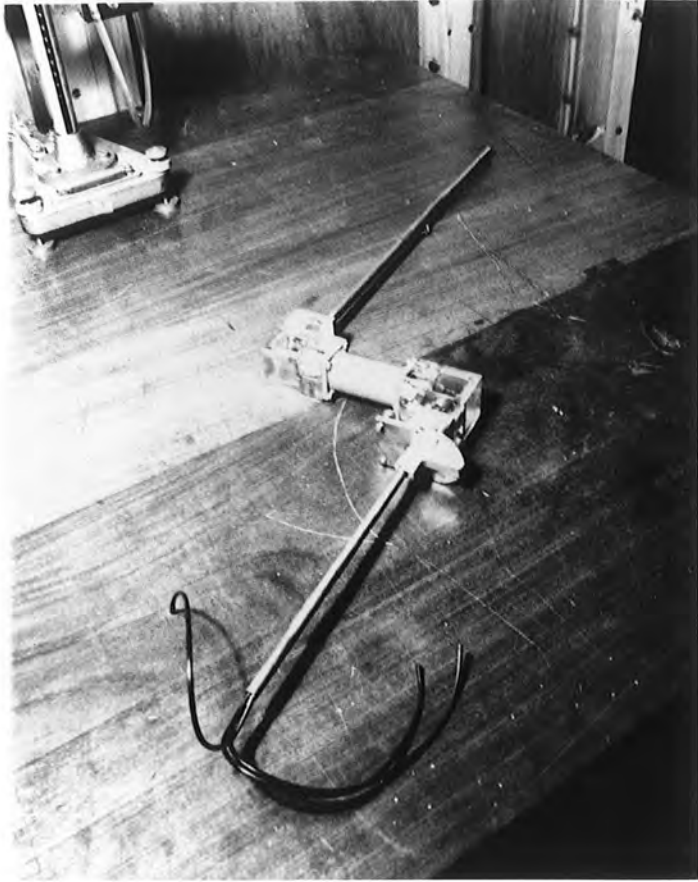
Figure 2.7(a)   THE CRANKED YAW PROBE

Figure 2.7(b)   THE CRANKED YAW PROBE

45

46
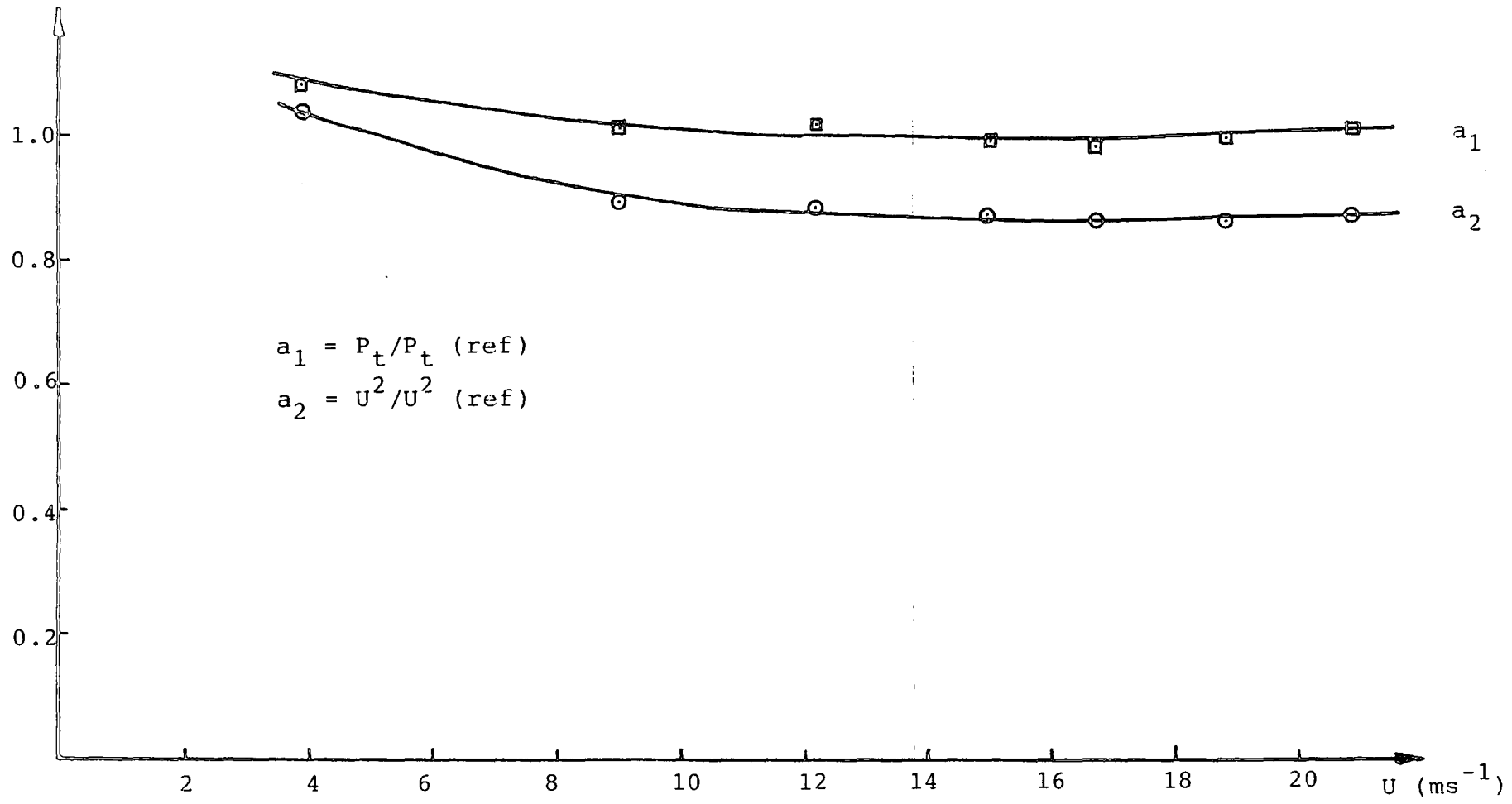
Figure 2.8   YAW PROBE CALIBRATION CURVES
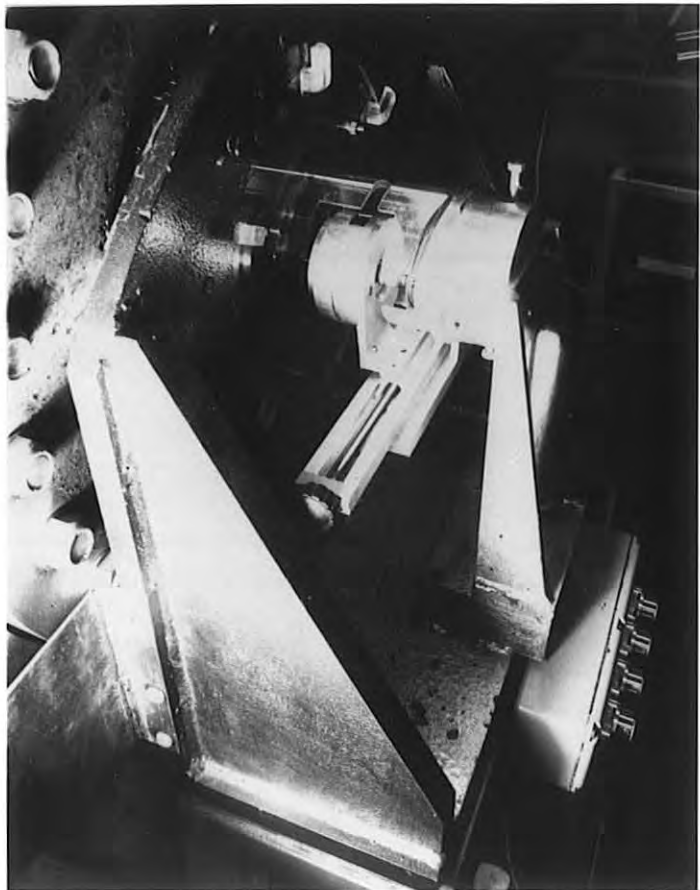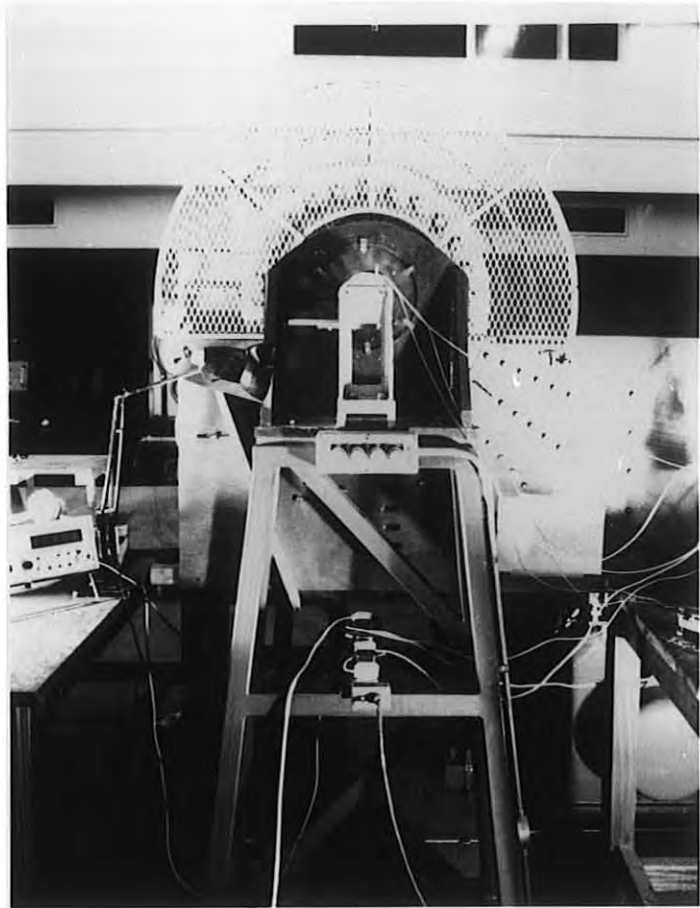
Figure 2.9   THE TRAVERSING MECHANISM

47

the centre hole of the probe head maintained the same angular orientation to the scale on the bezel at all times. The probe bezel is shown in Fig. 2.10.

Diametral wires attached to the fan blades allowed the probe head to be levelled with the centre-line of the rotor by means of three small jacking screws and provided the zero reading on the slide scale.

With this traversing geometry, the probe head could be positioned at any desired polar co-ordinate. The probe bezel was used to null the side tapping pressures and the flow velocity determined in the usual manner. This bezel was always rotated in the same sense during calibration in the working section and whilst traversing the fan interior to avoid any angular hysterisis that may have been present.

2.4.5.3 The Measurement of Pressure

All pressure measurements were made using micromanometers filled with silicon oil as manufactured for general department use. These instruments are accurate to $\pm$ 0.01mm H_2O.

2.4.6 The Experimental Procedure

Traverses of the internal flow regime of the rotor were related to a polar co-ordinate system located on the rotor centre-line, as shown in Fig. 2.11. The superimposed grid contained nine radii from the centre-line to within 20mm of the blades which were divided angularly into 15°
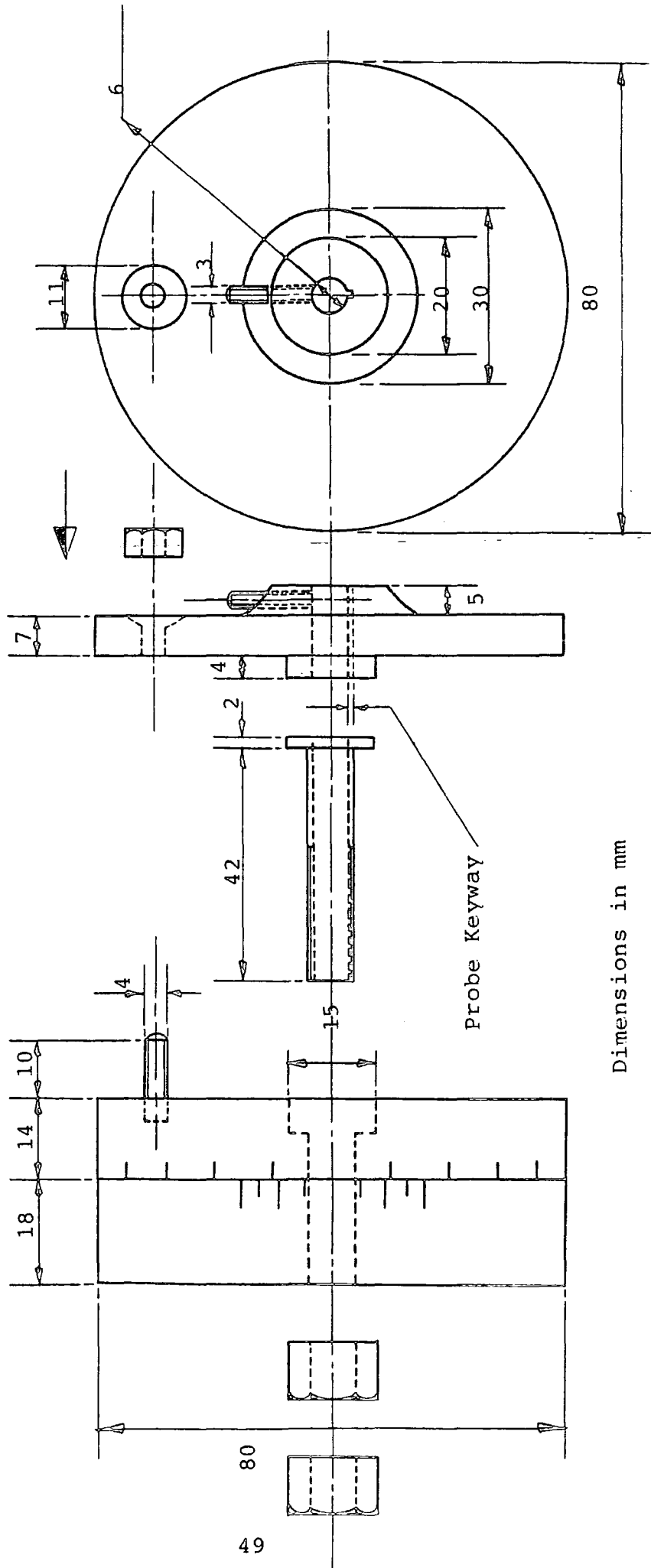
Figure 2.10 CONSTRUCTION OF THE PROBE SUPPORT BEZEL

Dimensions in mm

Probe Keyway

180°

90°   180°

θ minor

r   0°

270°

θ major

90°   270°

vertex wall

0°
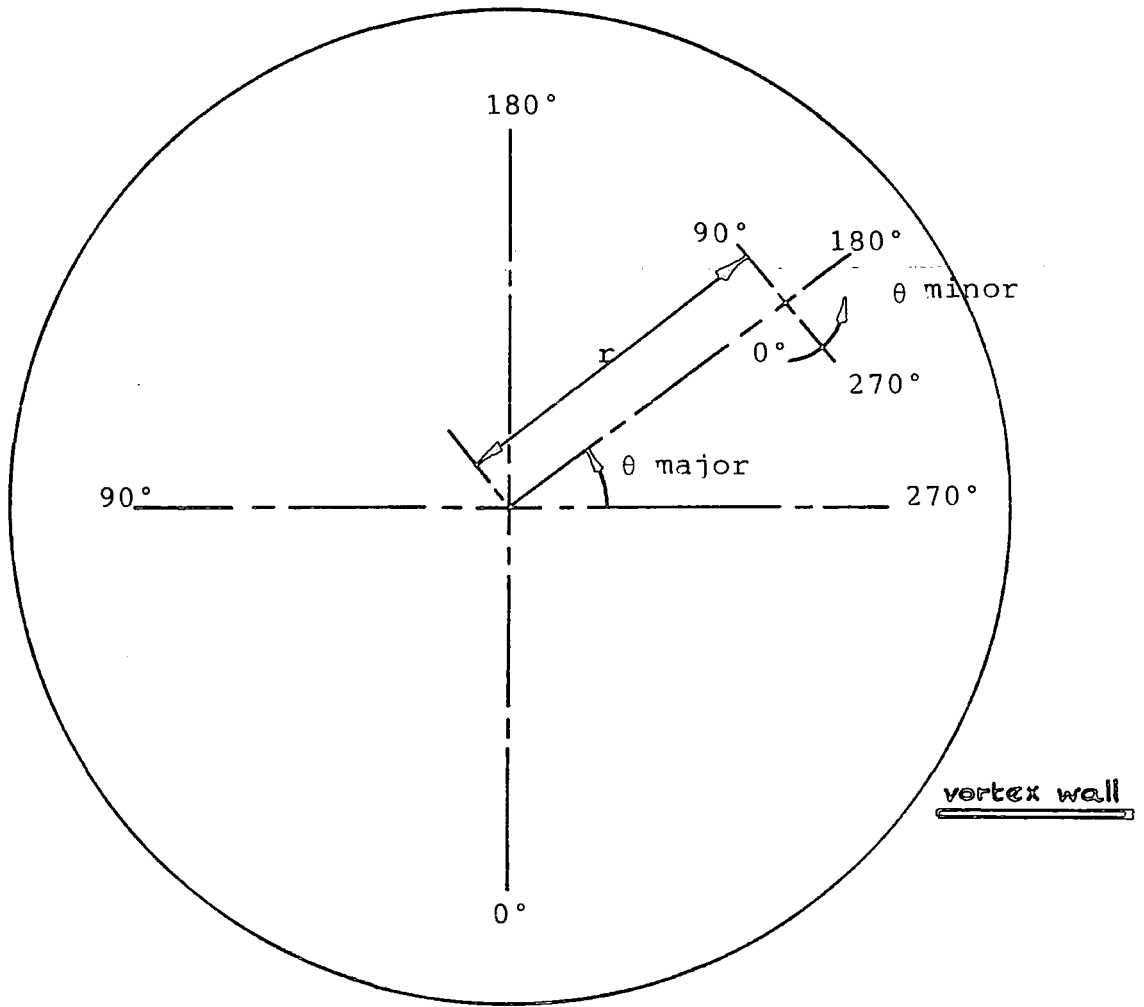
probe head at r, θ major

Figure 2.11 FAN INTERIOR COORDINATE SYSTEM

sectors. To yield a more comprehensive picture in the quadrant containing the vortex, the step size was reduced to 5°.

At each position in the polar grid, the probe head was yawed by means of the probe bezel, to null the pressures present at the two side tappings. Measures were then obtained of:

(i) the angle of the flow relative to a radial line between the fan centre-line and the probe head,

(ii) the velocity of the flow and,

(iii) the total pressure of the flow.

In some cases, especially in the quadrant containing the vortex, difficulty was found in assessing the predominant flow direction. To combat this problem, a series of tufts were connected freely to the shaft of the probe head, so that a visual indication of flow direction and quality was available.

The internal flow regime was examined at five flow coefficients between $\Phi = 0.4$ and 0.8 as this overlaps the general operating range of this type of fan. As complete traverses of the internal region took several days, it was important to maintain a fixed flow rate throughout. The iris shutter system attached to the pyramid diffuser allowed fine control over this parameter.

2.4.7   The Calculation of Results

2.4.7.1   The Calculation of Stream Function

For a comparison with previous studies the streamline
pattern in the rotor was required.   Fig.2.12 shows two adja-
cent streamlines associated with stream functions ψ_1 and ψ_2,
with local velocities of q_1 and q_2 and making angles of
θ_1 and θ_2 with respect to a radial line in the co-ordinate
system.   The streamlines are separated by the small radial
distance Δr, with the origin of the polar co-ordinate system
on the rotor centre-line. By definition

$$\psi_2 = \psi_1 + \bar{u} \, d_n$$

where, d_n is the normal distance between the streamlines
and

$$\bar{u} = \tfrac{1}{2}\{q_1 \sin(\theta + \theta_1) + q_2 \sin(\theta + \theta_2)\}$$

therefore,

$$\psi_2 = \psi_1 + \tfrac{1}{2}\{q_1 \sin(\theta + \theta_1) + q_2 \sin(\theta + \theta_2)\} \, \Delta r$$

The stream function for the streamline crossing the rotor
axis was arbitrarily chosen to be zero.   The radial and
tangential components of the velocities may be related to
the stream function by the expressions:

$$\frac{\delta \psi}{\delta \theta} = -rV_r \tag{1}$$

and

$$\frac{\delta \psi}{\delta r} = V_\theta \tag{2}$$

From the experimental results, all the velocity and
direction data were transformed into radial and tangential
components, so that the above expressions could be used
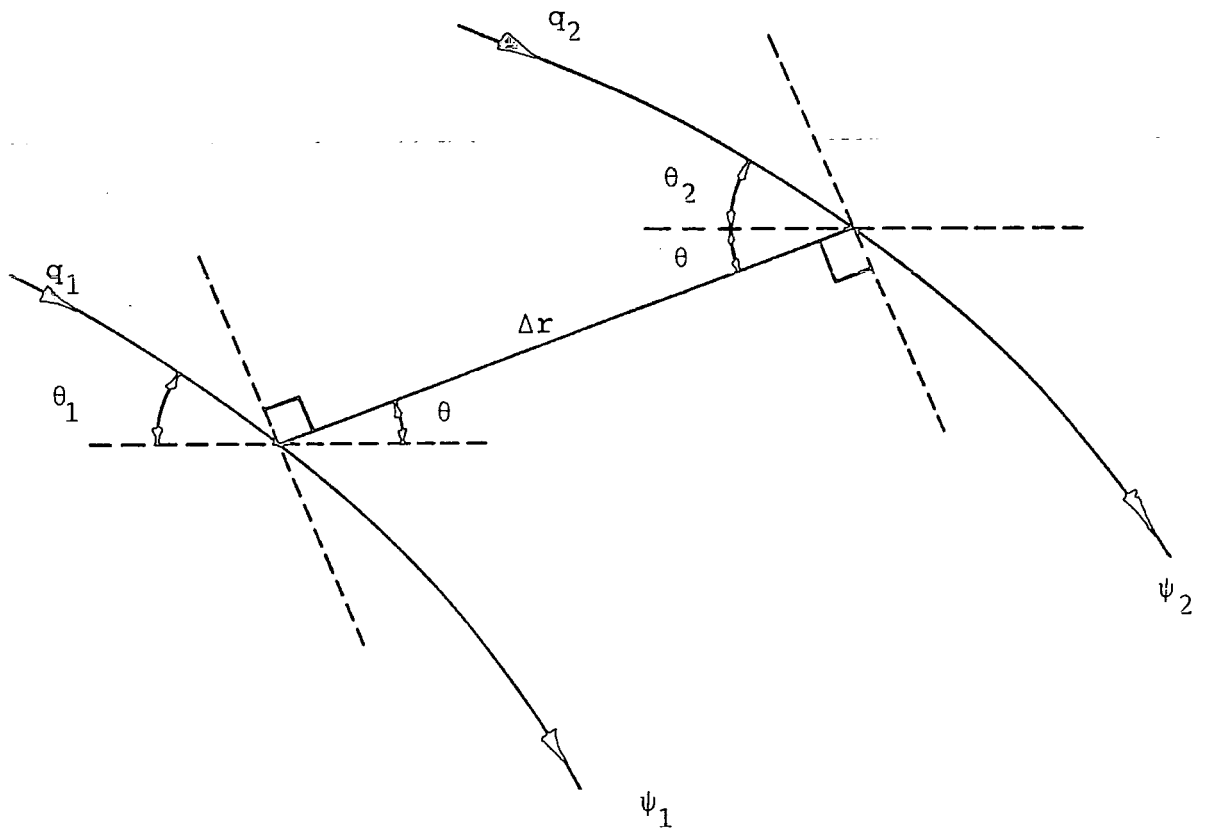
Figure 2.12 STREAMLINE GEOMETRY

53

in their incremental form:

$$\Delta \psi_\theta = -rV_r \Delta \theta \qquad (3)$$

and $\Delta \psi_r = V_\theta \Delta r \qquad (4)$

The calculation procedure was as follows:

(i) Plot V_r against θ, at all radii traversed (see Fig. 2.13 for $\Phi = 0.8$).

(ii) Plot V_θ against r, at all peripheral positions traversed (see Fig. 2.14 for $\Phi = 0.8$).

(iii) Begin the calculation procedure on the fan centre-line at $\psi = 0$, designated co-ordinate $r(0)$, $\theta(0)$.

(iv) Using eqn (4) find the change in stream function $\Delta \psi_1$ between the origin and $r(1)$, $\theta(270^O)$.

(v) Again using eqn (4) find the change in stream function $\Delta \psi_2$ between the origin nd $r(1)$, $\theta(275^O)$.

(vi) Using eqn (3) find the change in stream function $\Delta \psi_3$ between $r(1)$, $\theta(270^O)$ and $r(1)$, $\theta(275^O)$.

(vii) The two values of stream function present at co-ordinate $r(1)$, $\theta(275^O)$ are then averaged before the calculation proceeds, i.e. at co-ordinate $r(1)$, $\theta(275^O)$

$$\psi = \tfrac{1}{2}(\Delta \psi_1 + \Delta \psi_2 + \Delta \psi_3)$$

(viii) This method is repeated as the first radius $r(1)$ is scanned ending finally at $\theta(270^O)$ which is averaged with $\Delta \psi_1$ before proceeding. The second radius $r(2)$ is treated similarly except that the radial changes in stream function derived from eqn (4) are added to those present on the first radius $r(1)$ and so on as shown diagramatically in Fig. 2.15.

(ix) Curves are finally drawn of ψ against r, for constant θ and ψ against θ, for constant r as shown in Figs. 2.16 & 2.17 for
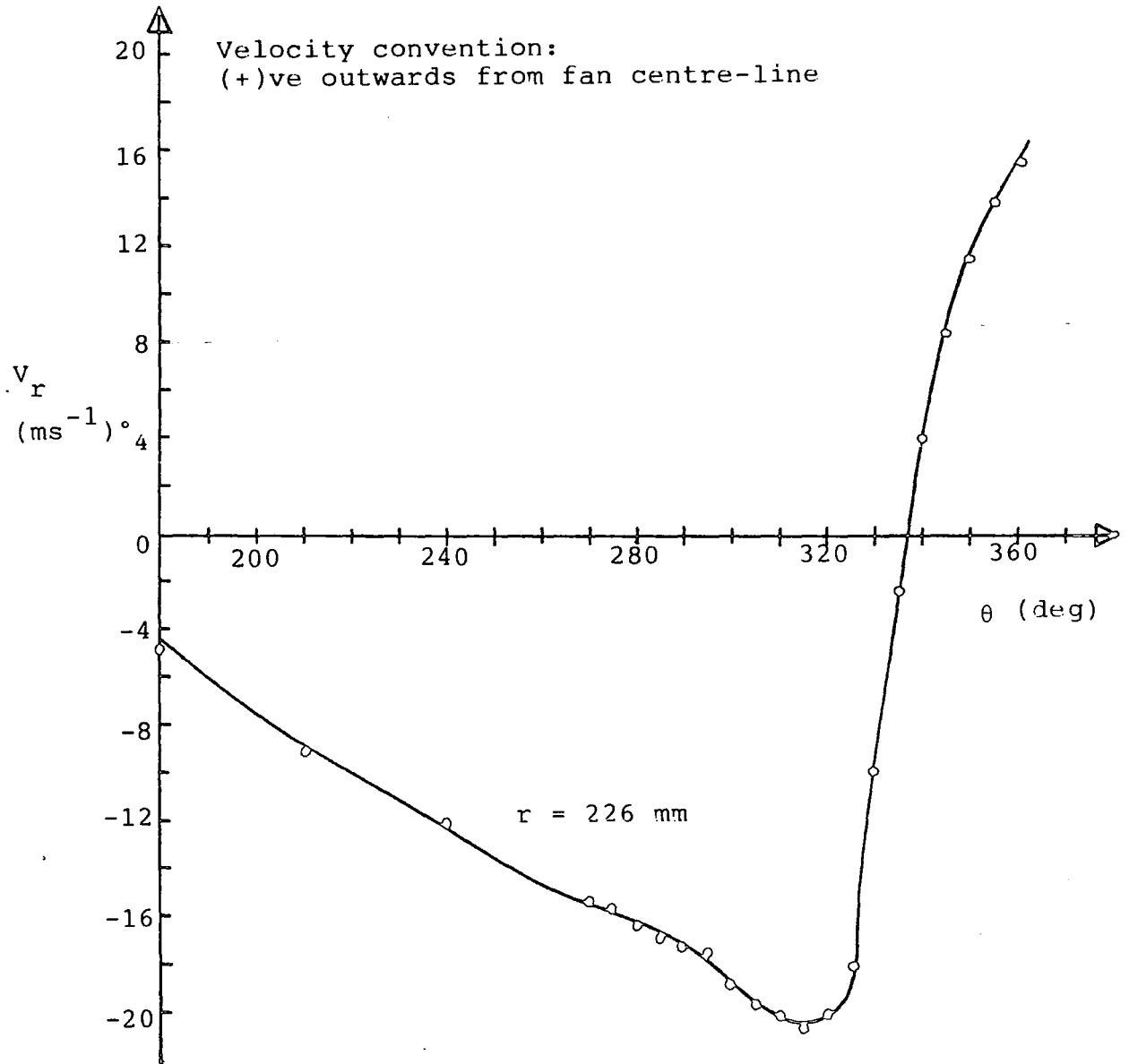
Figure 2.13   VARIATION OF RADIAL VELOCITY, $\Phi = 0.8$
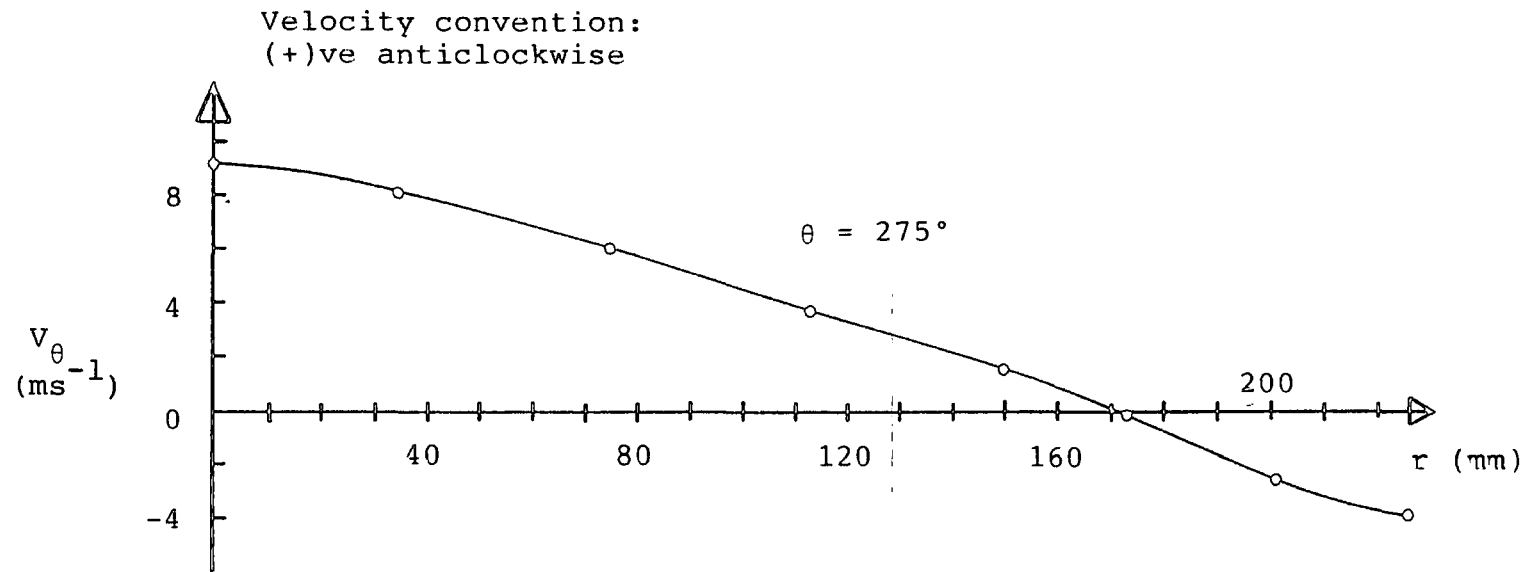
Figure 2.14   VARIATION OF TANGENTIAL VELOCITY, $\Phi = 0.8$
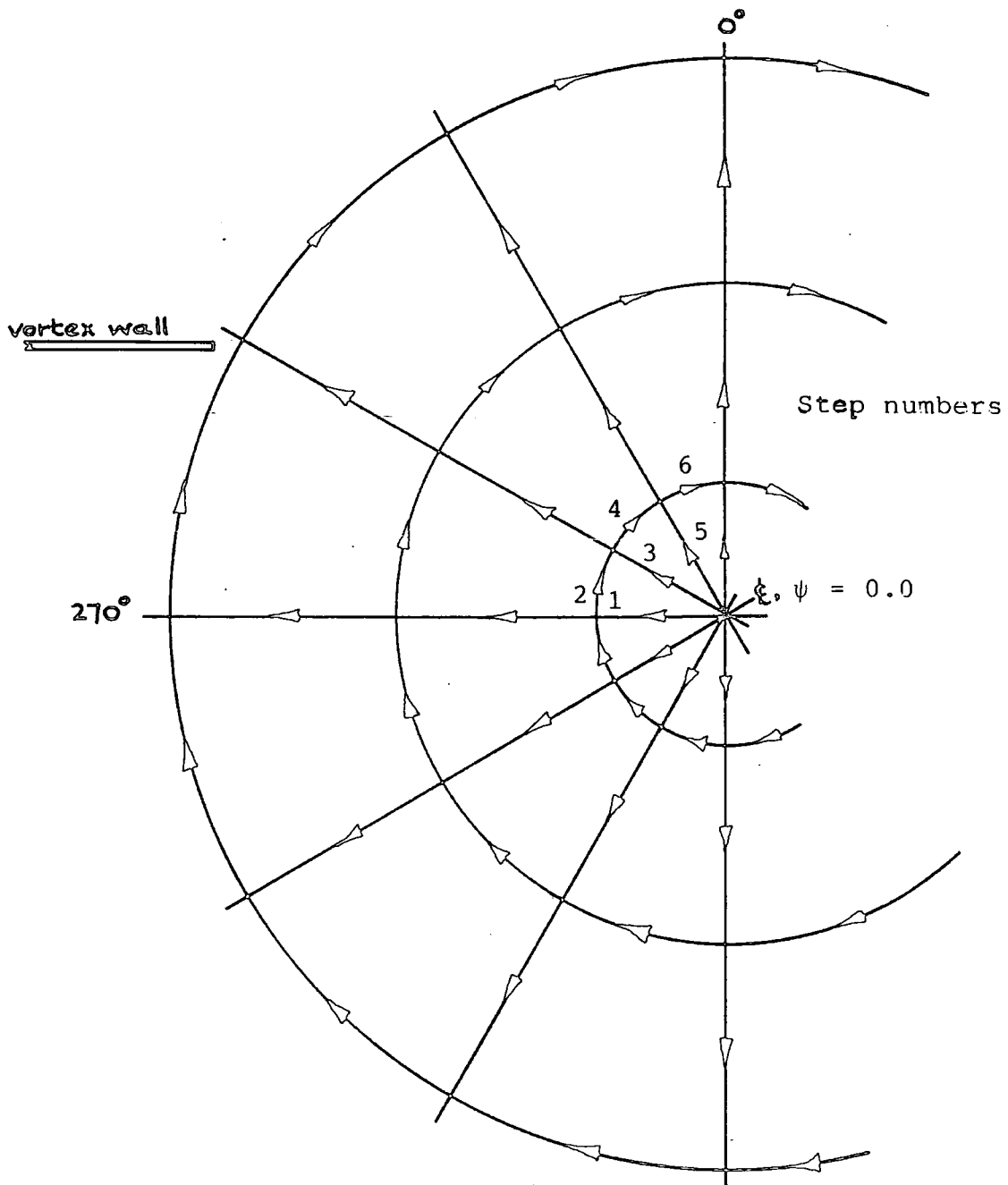
Figure 2.15   METHOD FOR CALCULATION OF STREAM FUNCTION

θ deg \ R mm	35	75	113	150	173	201	226
30	-0.3885 -0.3861 -0.3873	-0.8053 -0.8203 -0.8128	-1.1415 -1.2166 -1.1791	-1.4381 -1.5491 -1.4936	-1.6351 -1.6607 -1.6479	-1.7879 -1.7464 -1.7672	-1.8660 -1.8065 -1.8362
60	-0.0350 -0.0437 -0.0393	-0.0193 -0.0529 -0.0361	+0.0418 +0.0013 +0.0215	+0.1436 +0.0890 +0.1163	+0.2060 +0.2272 +0.2166	+0.3412 +0.3692 +0.3552	+0.4815 +0.5482 -0.5-49
90	+0.3028 +0.3006 +0.3017	+0.6897 +0.6649 +0.6773	+1.0592 +1.0362 +1.0477	+1.4473 +1.4672 +1.4572	+1.7160 +1.7882 +1.7521	+2.0657 +2.1075 +2.0866	+2.3791 +2.4851 +2.4321
120	+0.5478 +0.5518 +0.5498	+1.1738 +1.1642 +1.1690	+1.7447 +1.7222 +1.7334	+2.2459 +2.3054 +2.2757	+2.5747 +2.7168 +2.6458	+2.9972 +3.0864 +3.0418	+3.3256 +3.4557 +3.3906
150	+0.6545 +0.6579 +0.66562	+1.3562 +1.3693 +1.3627	+1.9764 +2.0174 +1.9969	+2.5853 +2.5938 +2.5645	+2.8693 +3.0127 +2.9410	+3.2742 +3.3786 +3.3264	+3.5827 +3.6273 +3.6050
180	+0.6038 +0.6113 +0.6076	+1.2556 +1.2626 +1.2591	+1.8177 +1.8786 +1.8481	+2.3328 +2.4271 +2.3799	+2.6605 +2.7553 +2.7079	+3.0173 +3.1370 +3.0771	+3.3084 +3.2737 +3.2910
210	+0.4025 +0.4198 +0.4111	+0.8691 +0.8919 +0.8805	+1.3023 +1.3511 +1.3267	+1.7226 +1.8144 +1.7685	+2.0031 +2.0376 +2.0204	+2.2836 +2.3825 +2.3330	+2.5430 +2.4331 +2.4880
240	+0.0998 +0.1087 +0.1043	+0.2703 +0.3032 +0.2868	+0.4825 +0.5240 +0.5037	+0.7313 +0.8339 +0.7826	+0.9344 +0.9742 +0.9543	+1.1377 +1.2279 +1.1828	+1.3466 +1.2396 +1.2931
270	START -0.2520 -0.2356 -0.2438	-0.4638 -0.4181 -0.4409	-0.5682 -0.5051 -0.5366	-0.5829 -0.4544 -0.5187	-0.5038 -0.4180 -0.4609	-0.4049 -0.3064 -0.3556	-0.2769 -0.3162 -0.2966
275	-0.3063 -0.3065 -0.3064	-0.5924 -0.5862 -0.5893	-0.7755 -0.7492 -0.7623	-0.8585 -0.8120 -0.8352	-0.8502 -0.7642 -0.8072	-0.7834 -0.6934 -0.7884	-0.6797 -0.5806 -0.6302
280	-0.3640 -0.3586 -0.3610	-0.7170 -0.7104 -0.7137	-0.9626 -0.9442 -0.9534	-1.1088 -1.0702 -1.0895	-1.1378 -1.0782 -1.1080	-1.115 -1.0392 -1.0771	-1.0359 -0.9448 -0.9903
285	-0.4113 -0.4103 -0.4108	-0.8328 -0.8322 -0.8325	-1.1536 -1.1348 -1.1442	-1.3644 -1.3336 -1.3490	-1.4341 -1.3820 -1.4081	-1.4529 -1.3884 -1.4207	-1.4032 -1.3197 -1.3614
290	-0.4603 -0.4574 -0.4588	-0.9428 -0.9461 -0.9444	-1.3282 -1.3217 -1.3249	-1.6117 -1.5944 -1.6031	-1.7296 -1.6821 -1.7059	-1.7969 -1.7391 -1.7680	-1.7818 -1.7095 -1.7456
295	-0.5058 -0.5026 -0.5042	-1.0522 -1.0521 -1.0521	-1.5005 -1.4965 -1.4985	-1.8445 -1.8374 -1.8410	-1.9986 -1.9731 -1.9859	-2.1077 -2.0767 -2.0922	-2.1347 -2.0899 -2.1122
300	-0.5425 -0.5441 -0.5433	-1.1463 -1.1529 -1.1491	-1.6621 -1.6632 -1.6626	-2.0585 -2.0609 -2.0597	-2.2357 -2.3403 -2.2380	-2.3724 -2.3878 -2.3801	-2.4339 -2.4455 -2.4397
305	-0.5810 -0.5786 -0.5798	-1.2358 -1.2401 -1.2379	-1.8098 -1.5174 -1.8136	-2.2632 -2.2704 -2.2668	-2.4761 -2.4962 -2.4861	-2.6709 -2.6997 -2.6803	-2.7828 -2.7908 -2.7868
310	-0.6125 -0.6105 -0.6115	-1.3215 -1.3194 -1.3204	-1.9493 -1.9546 -1.9520	-2.4626 -2.4736 -2.4681	-2.7315 -2.7533 -2.7424	-3.0014 -3.0048 -3.0031	-3.1544 -3.1566 -3.1555
315	-0.6458 -0.6372 -0.6415	-1.3935 -1.3908 -1.3921	-2.0609 -2.0772 -2.0691	-2.6537 -2.667 -2.6607	-2.9919 -3.0058 -2.9989	-3.3349 -3.3364 -3.3356	-3.5381 -3.5470 -3.5425
320	-0.6650 -0.6820 -0.6635	-1.4494 -1.4487 -1.4491	-2.1559 -2.1746 -2.1653	-2.8110 -2.8420 -2.8265	-3.2198 -2.2382 -3.2290	-3.6532 -3.6645 -3.6588	-3.9263 -3.9419 -3.9341
325	-0.6843 -0.6786 -0.6815	-1.5035 -1.4930 -1.4982	-2.2506 -2.2506 -2.2506	-2.9536 -2.9764 -2.9650	-3.4089 -3.4328 -3.4209	-3.9249 -3.9552 -3.9401	-4.2664 -4.2876 -4.2876
330	-0.6895 -0.6907 -0.6901	-1.5281 -1.5283 -1.5282	-2.330 -2.3177 -2.8238	-3.0920 -3.0776 -3.0848	-3.5678 -3.5892 -3.5785	-4.1399 -4.1795 -4.1597	-4.5347 -4.5943 -4.5645
335	-0.4035 -0.6933 -0.6984	-1.5544 -1.5426 -1.5485	-2.3579 -2.3672 -2.3625	-3.1562 -3.1574 -3.1568	-3.6778 -3.6925 -3.6851	-4.2927 -4.3088 -4.3007	-4.6782 -4.7151 -4.6968
340	-0.6983 -0.6957 -0.6970	-1.5450 -1.5469 -1.5459	-2.3629 -2.3768 -2.3693	-3.1857 -3.1797 -3.1827	-3.7094 -3.7251 -3.7173	-4.3128 -4.3406 -4.3262	-4.6900 -4.6791 -4.6845
345	-0.6913 -0.6881 -0.6897	-1.5317 -1.5286 -1.5301	-2.3357 -2.3555 -2.3456	-3.1504 -3.1631 -3.1567	-3.6777 -3.6811 -3.6794	-4.2492 -4.3631 -4.2561	-4.5811 -4.5603 -4.5707
350	-0.6808 -0.6750 -0.6779	-1.5079 -1.4977 -1.5028	-2.2970 -2.3042 -2.3006	-3.0721 -3.0945 -3.0833	-3.5686 -3.5790 -3.5788	-4.1058 -4.1123 -4.1090	4.4128 -4.3725 -4.3926
355	-0.6615 -0.6576 -0.6595	-1.4635 -1.4557 -1.4596	-2.2348 -2.2331 -2.2339	-2.9721 -2.9803 -2.9762	-3.4282 -3.4243 -3.4263	-3.9191 -3.9003 -3.9097	-4.2060 -4.-392 -4.1726
360	-0.6335 -0.6335 -0.6335	-1.3975 -1.3977 -1.3976	-2.-272 -2.1402 -1.1337	-2.8238 -2.8348 -2.8293	-3.2468 -3.2361 -3.2414	-3.6824 -3.6519 -3.6671	-3.9549 -3.8797 -8.9128

TABLE 2.2   CALCULATION OF ψ FOR Φ = 0.8
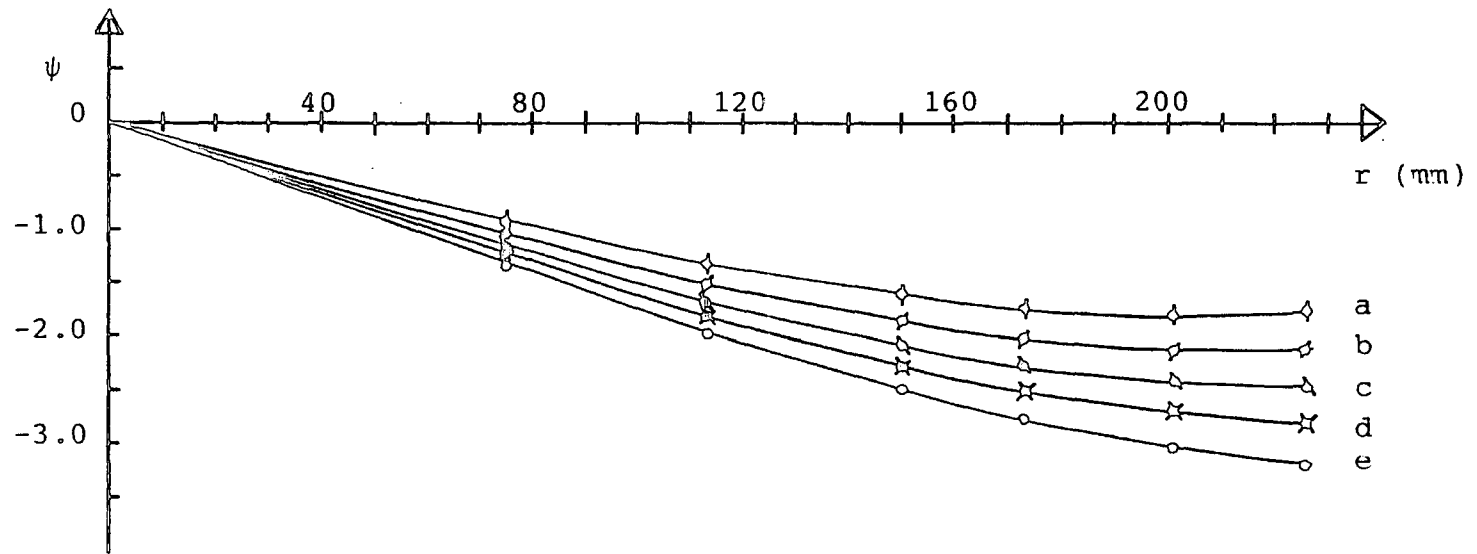
Figure 2.16(a)RADIAL VARIATION OF STREAM FUNCTION, $\phi = 0.8$

θ \ ψ	3.0	-2.5	-2.0	-1.5	-1.0	-0.5
a 290				134	81	38
b 295			173	113	72	35
c 300			144	100	65	32
d 305		173	128	91	60	30
e 310	201	152	116	85	57	30

Figure 2.16(b)
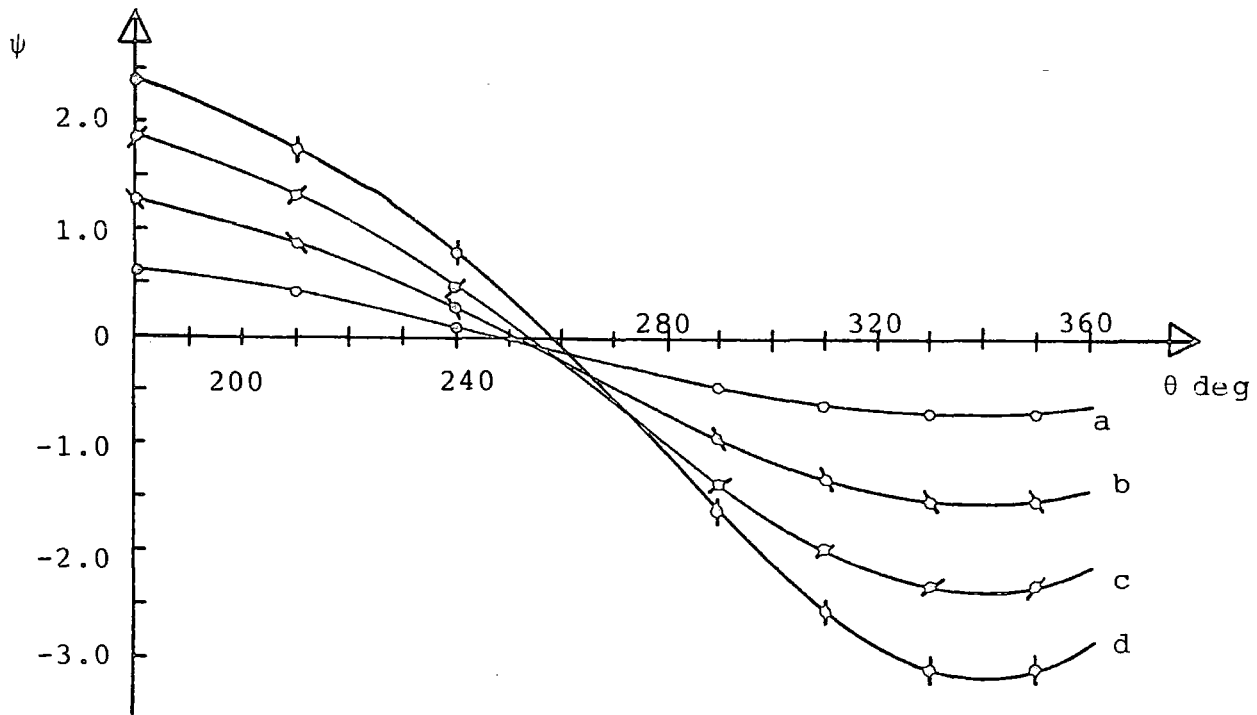
r	ψ	-3.0	-2.5	-2.0	-1.5	-1.0	-0.5	0.0	0.5	1.0	1.5	2.0
a	35						295	249	199			
b	75				325 350	293	272	252	230	202		
c	113			311	295	281	269	255	240	223	201	
d	150	326 354	310	298	288	278	269	258	247	234	219	200

Figure 2.17   PERIPHERAL VARIATION OF STREAM FUNCTION, Φ =0.8

61

$\Phi = 0.8$, from which co-ordinates are extracted for the final flow diagrams.

2.4.7.2 The Calculation of Total Pressure Coefficient

Measurements of the total pressure were taken using the polar co-ordinate system previously described to verify that the total pressure remained constant along a particular streamline and to give an indication of the type of vortex flow in existence. This latter point was established as follows. The pressure variation perpendicular to a streamline is given by

$$\frac{\delta p}{\delta r}s = \rho \frac{V_\theta^2}{r} \qquad (5)$$

For a free vortex (irrotational flow)

$$rV_\theta = \text{constant, } K \qquad (6)$$

so that eqn (5) becomes

$$\frac{\delta p}{\delta r}s = \rho \frac{K^2}{r^3} \qquad (7)$$

Integration with respect to r gives

$$P_s = -\rho \frac{K^2}{2r^2} + \text{constant} \qquad (8)$$

By definition

$$P_t = P_s + \frac{1}{2}\rho V_\theta^2$$

from which

$$P_t = -\frac{\rho K^2}{2r^2} + \frac{1}{2}\rho \left(\frac{K}{r}\right)^2 + \text{constant} \qquad (9)$$

and so, in a free vortex p_t is constant.

For a forced vortex

$$V_\theta = r\omega \qquad (10)$$

and by a similar means, it is easy to show

$$p_t = \rho V_\theta^2 + \text{constant} \tag{11}$$

Fig.2.18 shows typical velocity and pressure distributions for a free vortex with a forced vortex core (known as a RANKINE vortex) expected to exist in the rotor along with some measured data for velocity.

The measured total pressures were presented in dimensionless form as a total pressure coefficient

$$\tilde{t} = \frac{p_t - p_{t0}}{\frac{1}{2} \rho U_2^2}$$

where, p_{t0} = total pressure on the rotor axis, P_a.

p_{t0} was an arbitrary choice with no special significance, apart from ensuring $\tilde{t}$ was always zero on the fan centre-line regardless of the throughflow.

2.5 Results and Conclusions from Aerodynamic Study

The curves drawn of ψ against r for constant θ and ψ against θ for constant r as shown in Figs.2.16 , 2.17, for example, were used to extract co-ordinates for the final flow diagrams as shown in Figs.2.19,(a)(e) for Φ = 0.4 to 0.8. Distributions of the dimensionless total pressure coefficient $\tilde{t}$, are shown in Figs.2.20 (a)(e), for Φ = 0.4, 0.6 and 0.8.

For all flow rates, a flow approximating to a RANKINE type vortex was present within the rotor. The dimensionless total pressure exhibited a severe depression in the vicinity of the vortex core and became further depressed as the flow rate increased and the vortex strengthened. A
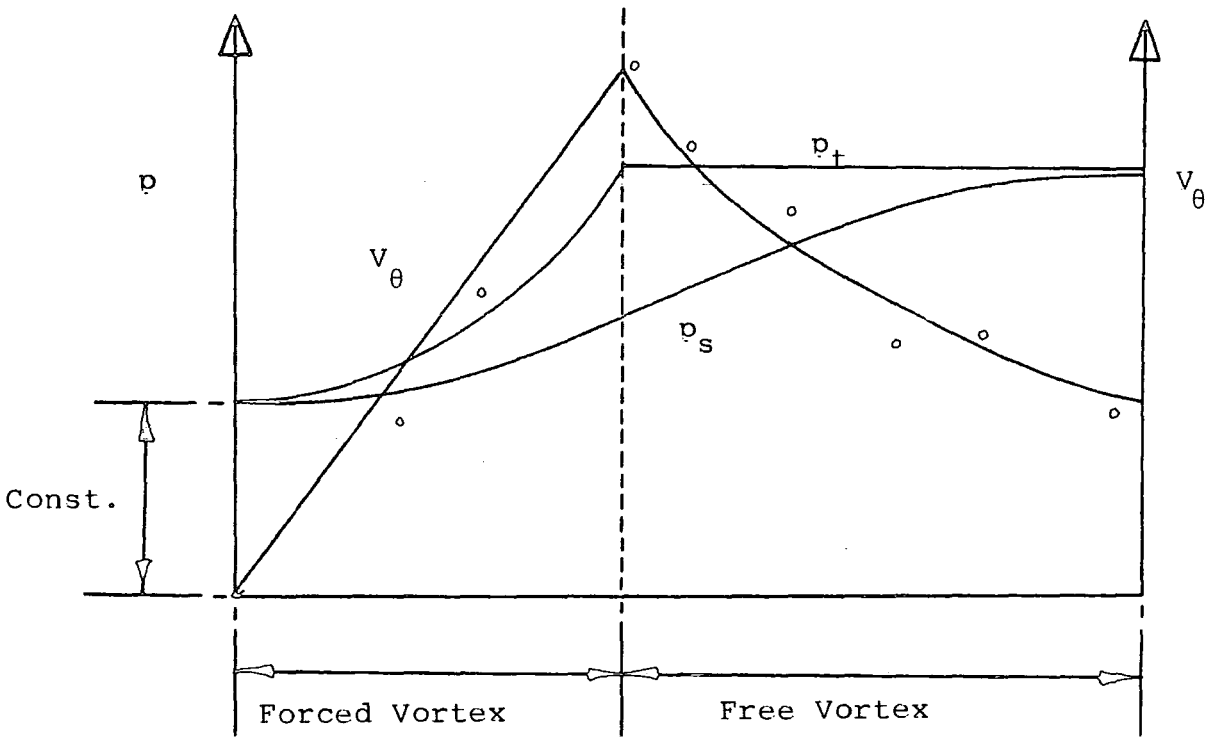
Figure 2.18   THEORETICAL VELOCITY AND PRESSURE DISTRIBUTIONS
IN A RANKINE VORTEX

Figure 2.19(e) , $\Phi = 0.4$ ———

Figure 2.19(d) , $\Phi = 0.5$ ———

Figure 2.19(c) , $\Phi = 0.6$ ———
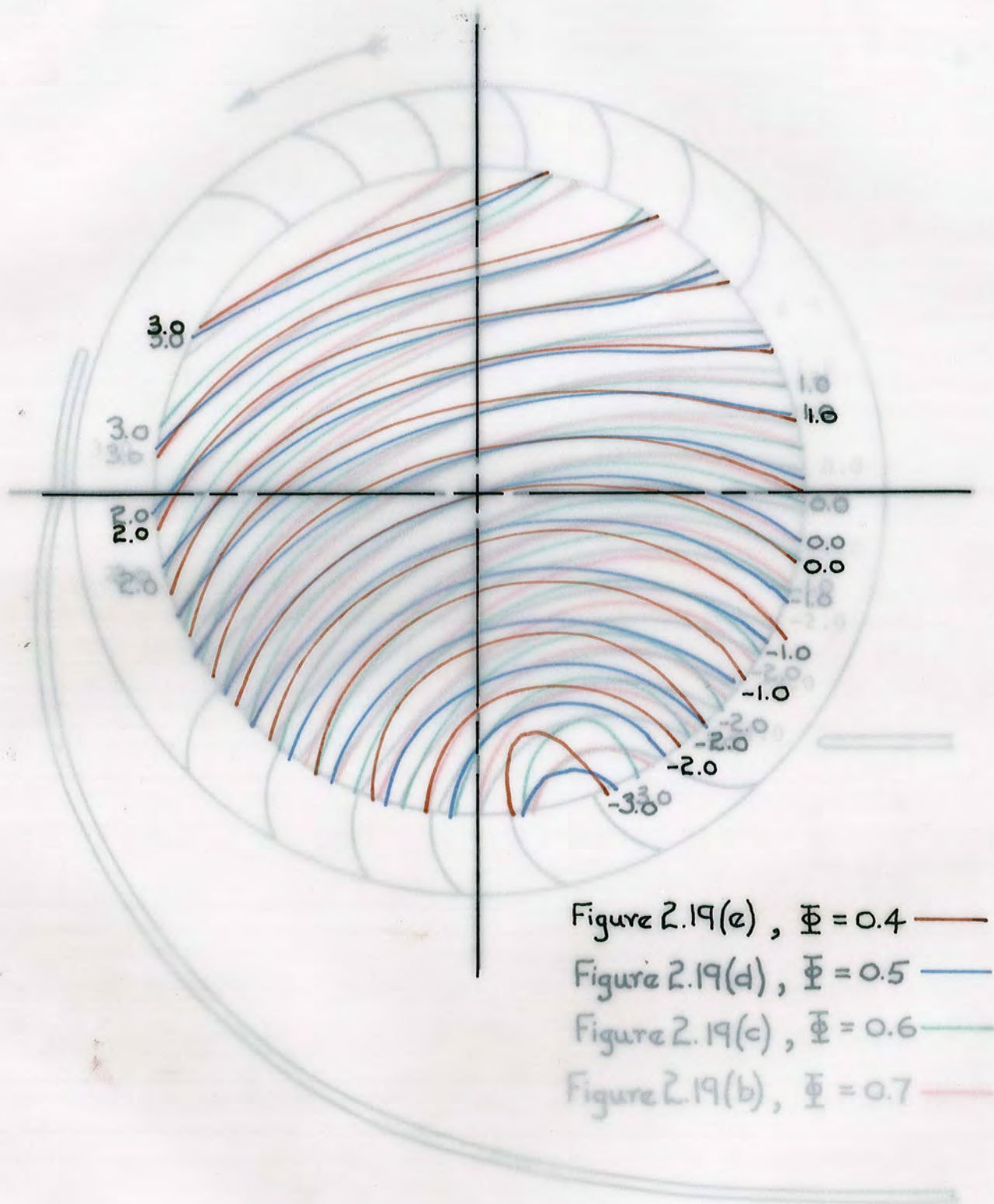
Figure 2.19(b) , $\Phi = 0.7$ ———

Figure 2.19(a)   STREAMLINE PATTERN, $\Phi = 0.8$

Region	$\tilde{t}$ Range
1	0
2	-2 to 0
3	-4 to -2
4	-6 to -4
5	-8 to -6
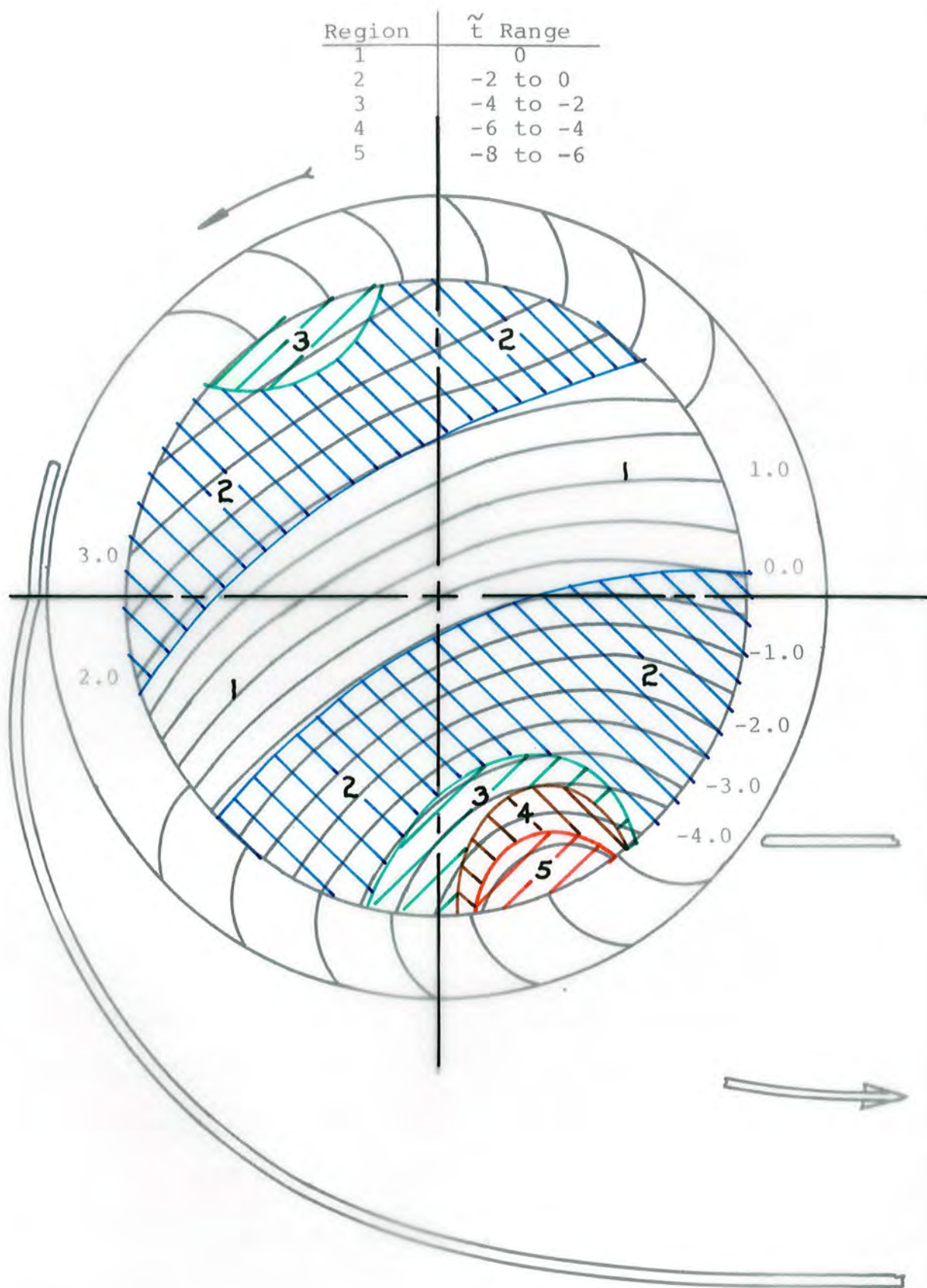
Figure 2.20(a)   TOTAL PRESSURE DISTRIBUTION, Φ =0.8

REGION	$\tilde{t}$ RANGE
1	0
2	-2 to 0
3	-4 to -2
4	-6 to -4
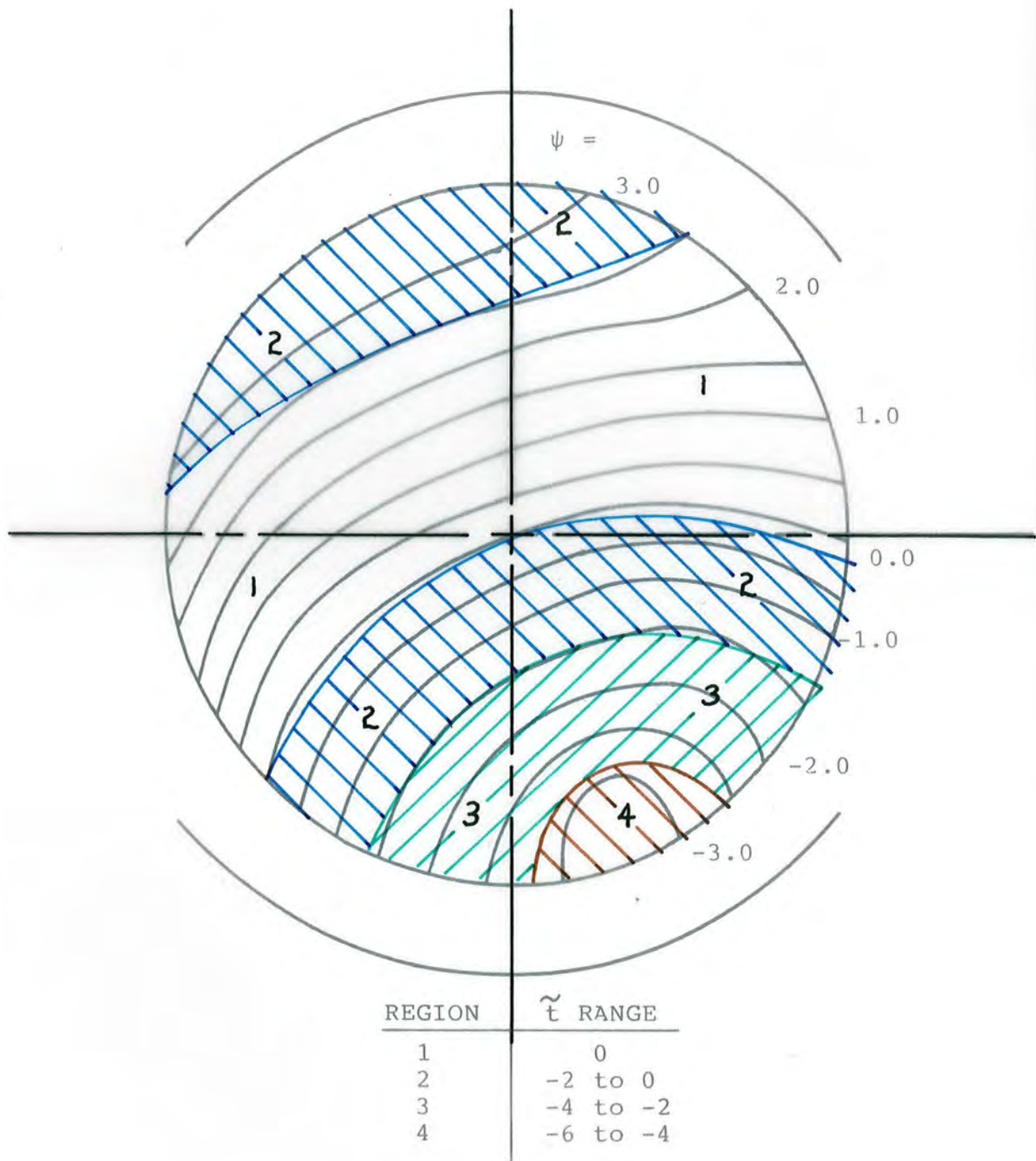
Figure 2.20(b)   TOTAL PRESSURE DISTRIBUTION, Φ = 0.6
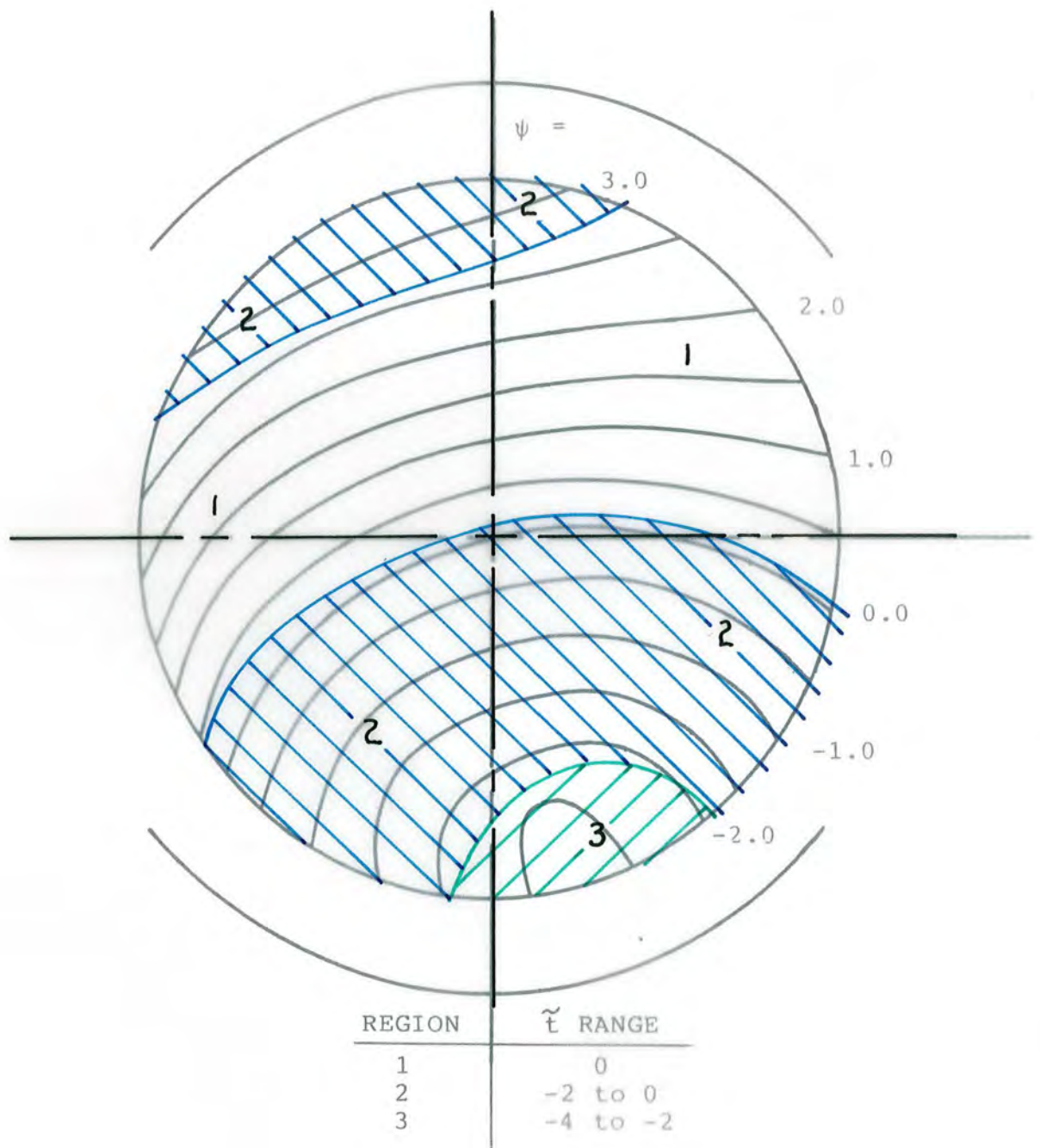
Figure 2.20(c) TOTAL PRESSURE DISTRIBUTION, $\Phi = 0.4$

REGION	$\tilde{t}$ RANGE
1	0
2	-2 to 0
3	-4 to -2

region of low total pressure (low energy) was present
almost diametrically opposite the vortex core, which
became more depressed and covered a larger area as the
flow rate increased (Chapter 3 on the hydrodynamic facility
confirms the existence of this region). The streamlines
do not remain concentric with the vortex core as the fan
is traversed radially. They are seen to flatten and indeed
exhibit reversed curvature towards the rear wall leading
edge (again see Chapter 3 for confirmation of this effect).

The streamlines yield a velocity profile across a
diameter, including the vortex core, which peaks at the
boundary between the free and forced vortex regions and
progressively reduces towards the rear wall leading edge.
The streamlines also indicate a general acceleration of
the flow across the fan interior. For $\Phi = 0.8$, the veloci-
ties in the quadrant containing the vortex core are seen
to be higher than those for $\Phi = 0.4$, whereas the velocities
in the opposite quadrant towards the rear wall, are similar
for both flow rates.

The location of the vortex core changed little in the
range $\Phi = 0.5$ to 0.8, but began to displace peripherally
and radially in the range $\Phi = 0.4$ to 0.5.

CHAPTER THREE

THE HYDRODYNAMIC FACILITY

3. THE HYDRODYNAMIC FACILITY

3.1 Introduction

Flow visualization techniques are often used to indi-
cate the general nature of the flow behaviour and with care,
some may be developed to yield not only qualitative but
quantitative data, particularly for water flows (see ref.
6). To provide a full understanding of the basic aero-
dynamic principles governing the flow through a cross flow
fan, visualization studies were carried out on a model
rotor built to a geometric scale of 1:6.25 and operated with
dynamic similarity to the aerodynamic facility (see Chapter
2).

3.2 Flow Visualization Techniques

Many techniques now exist for the visualization of
water flows, of which two were examined for their suitability.
The controlled introduction of hydrogen in water by
electrolysis has become a very popular method in recent
years. Hydrolysis of water generates hydrogen bubbles
from a cathode when d.c. is supplied between electrodes.
If the cathode takes the form of a thin wire, a very fine
cloud of bubbles is formed which appears as a line when
viewed edgewise. It is also possible to pulse the supply
to obtain time-streak markers, which can provide quantitative

data.

This technique has several advantages over other methods of flow visualization. The hydrogen bubbles are easily produced and their size and density controlled using standard power supplies. The flow is unaffected if the cathode wire is made sufficiently small and contamination of the fluid does not occur as with colloidal tellurium or dye streaks. It is also possible to maintain flow identity in wakes or minor turbulence, when sufficient power is supplied between electrodes. Due to the highly reflective nature of a liquid/gas interface, good contrast may be achieved on the photographic flow records.

ASANUMA and TAKEDA (ref. 3) used this technique to visualize the flow in a rotary cascade consisting of an inlet guide vane, a rotor, a stator and finally an outlet guide vane, with internal velocities up to $7ms^{-1}$. Although a d.c. voltage of 800 volts at 2.1 amps was used, it was only possible to determine the location of flow disturbances and stalling of blades.

The highly turbulent flow in and around a cross flow rotor was found too great to allow any reasonably sustained stream to be observed, especially on passing through blade passages where the bubbles were totally dispersed. General flow patterns could be discerned but the powers associated with the hydrolysis were dangerously high. However, a facility was included on the rig whereby two adjacent blades acted as electrodes, allowing the flow between blades to be examined at various positions around the suction and discharge arcs.

The second visualization technique examined for its suitability was the already proven method using neutral density polystyrene spheres. ROBERSON (ref. 25) used opaque polysterene spheres in water containing a little salt, so that the ratio of particle density to liquid density was in the range of 0.99 to 1.01. His theoretical analysis, as with that of FAURE (ref. 11), showed large deviations could be expected between the particle direction and the true streamlines, with density ratios outside this range. Also, deviations were minimised with small particle diameters. A compromise between the hydrodynamic performance and the optical requirements is called for.

Using this method, neutral density polysterene beads of 0.5mm. diameter were used as tracers after first soaking them in water to ensure a thoroughly wetted surface. Illumination was provided by three high-power, halogen strip lamps each collimated to produce a thin slice of light transversely across the tank at the mid-span position of the rotor. A camera was mounted above the tank and was positioned directly above the rotor axis. By choosing a suitable shutter speed it was possible to record photographic streaks which represented the displacements of the beads during the period of shutter opening. From these, local velocities both in terms of magnitude and direction could be estimated knowing the shutter speed.

Care was taken to ensure that the start and end of a streak was due solely to the chosen exposure time and that the corresponding sphere had not had a large axial velocity component which caused it to pass across and out

of the light beam. With this condition satisfied, the
motion could be regarded as substantially two dimensional.

3.3 The Water Table

A water table was constructed to enable flow visuali-
zation studies to be carried out on a model cross flow
fan, using techniques discussed in the last section.
Dynamically similar operating conditions were achieved
by driving the rotor at the speed necessary to give equality
of Reynolds number with the aerodynamic facility. Normally,
the characteristic length used in defining Reynolds number
is the blade chord with the velocity term given by the
blade tip speed. However, certain shortcomings of this
will be discussed later.

3.3.1 The Design and Manufacture of Tank

The tank was constructed totally from thick perspex
sheet. All butted faces were flat and well finished to
ensure water tight joints, using both screws and a bonding
agent. The rectangular tank was supported on a framework
of all welded construction using mainly square section
hollow tubing. The frame sat on six legs of which the
four outer legs were made of steel angle section. The
finished tank was located and supported on a square sec-
tion tube perimeter.

To limit the calculated high deflections throughout
the framework due to the large weight of water, a

74

longitudinal carriage truss was installed below the tank base which was positioned at mid-span and ran the full length of the support framework. Calculations showed mid-span deflections to be reduced by a factor of eight. Figure 3.1 shows a general arrangement of the water table.

3.3.2 The Design and Manufacture of Model Rotor

The rotor was a 1:6.25 geometrically similar model of the fan described in Chapter 2 and consisted of 24 pressed stainless steel blades, manufactured using a jig having a radius of curvature somewhat smaller than that required for the final blades, to allow for stress relief. The rotor end plates were constructed from heavy gauge perspex. The lower end plate was annularly rebated which allowed the blades to be located radially. The 24 identical blades were arranged symmetrically around the circumference using a wooden cylinder marked in 24 equal increments. A bonding agent was poured around each blade root filling completely the annular slot. After the solution hardened, the wooden cylinder was removed and the upper and plate (which took the form of a ring) was located and bonded. A side elevation of the rotor features is shown in Fig. 3.2 .

Excessive mid-span deflection of the rotor blades was avoided by using the principles discussed in Appendix ‖ .

3.3.3 The Design and Manufacture of the Rotor Casing

All casing components were manufactured totally from

Figure 3.1 LAYOUT OF HYDRODYNAMIC TEST RIG

76

Figure 3.2   ROTOR DRIVE AND INSTALLATION

Top Cover

Tank Base

17

3

9

75

162

111

1.5

38

6

1.5

16

3

16

35   24

48

Seal Unit Threaded 35⌀
Hexagonal Head

50

22

22

6

12

Dimensions in mm

77
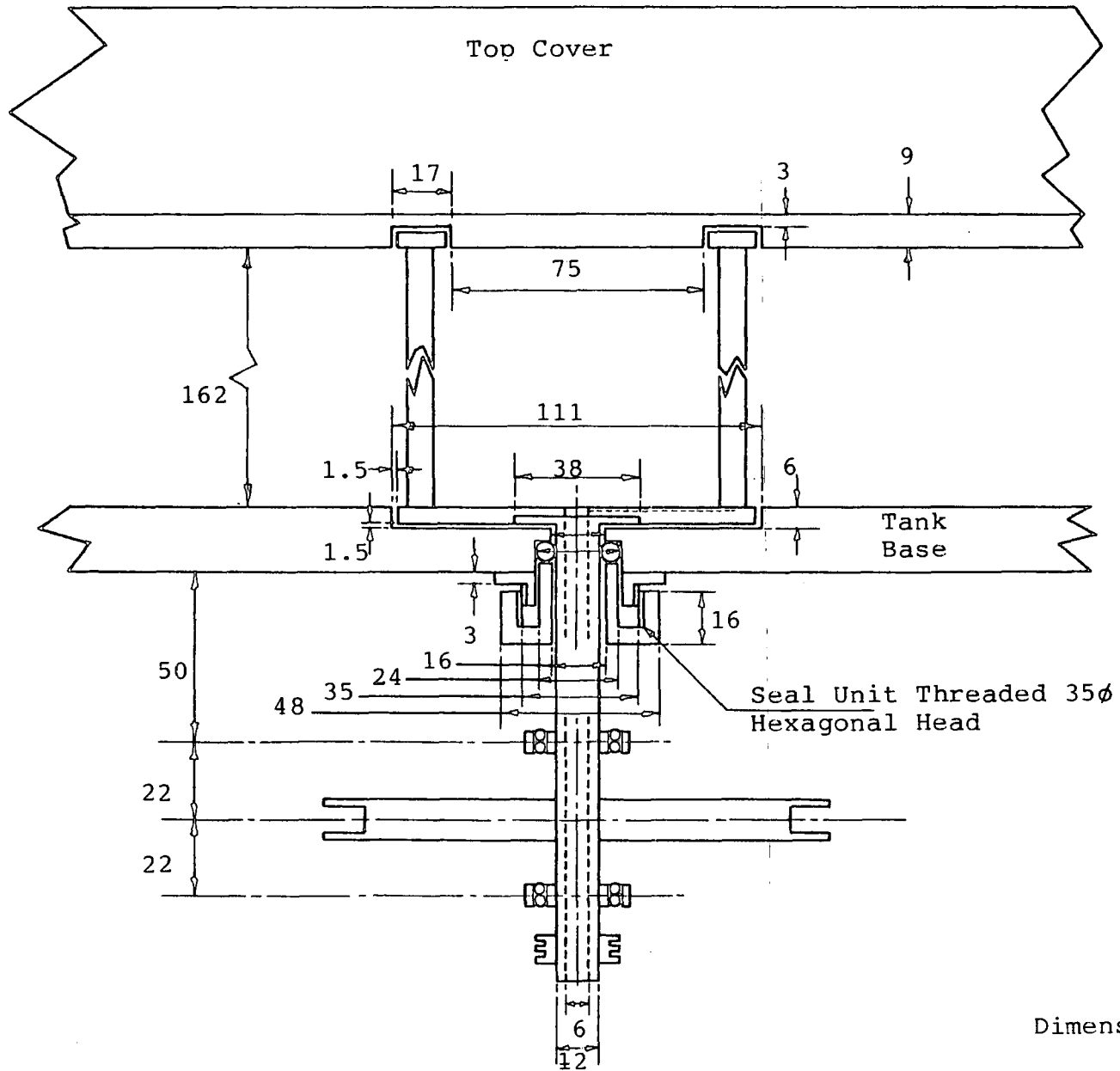
perspex allowing maximum transmission of light to the rotor interior. The logarithmic spiral rear wall was formed from a solid block made by bonding together sheets of heavy gauge perspex. The circular arc extension to the rear wall included five sections, each allowing an addition of 10° to the rear wall height (α_1). These extension pieces were located by two lugs on the underside and two holes in the top side. When fitted together in the correct order, a rear wall height of $\alpha_1 = 50^{\circ}$ could be achieved. A pair of square headed, threaded brass bars, firmly secured the whole rear wall unit to the duct base plate, which contained two slots allowing adjustment of the rear wall clearance. A slotted plate attached to the rear wall gave further support on two brass studs and a key protruding from the tank base.

The vortex wall was constructed from three layers of light gauge perspex. The two outer layers were bonded to the downstream wall section and the middle layer was allowed to slide freely varying the vortex wall clearance. A simple brass mechanism attached between the vortex wall and the duct base enabled the position of the leading edge (α_2) to be adjusted. Details of the rear and vortex walls are shown in Fig. 3.3 .

The second side of the fan casing was provided by a large perspex cover, shown in Figs. 3.1 and 3.2, which completely sealed the test section from atmosphere. The underside of the cover contained an annular rebate which located the top ring of the rotor. Thin walled plastic tubing sliced longitudinally and positioned along the

All values 4 mm

All 10°

Dimensions in mm
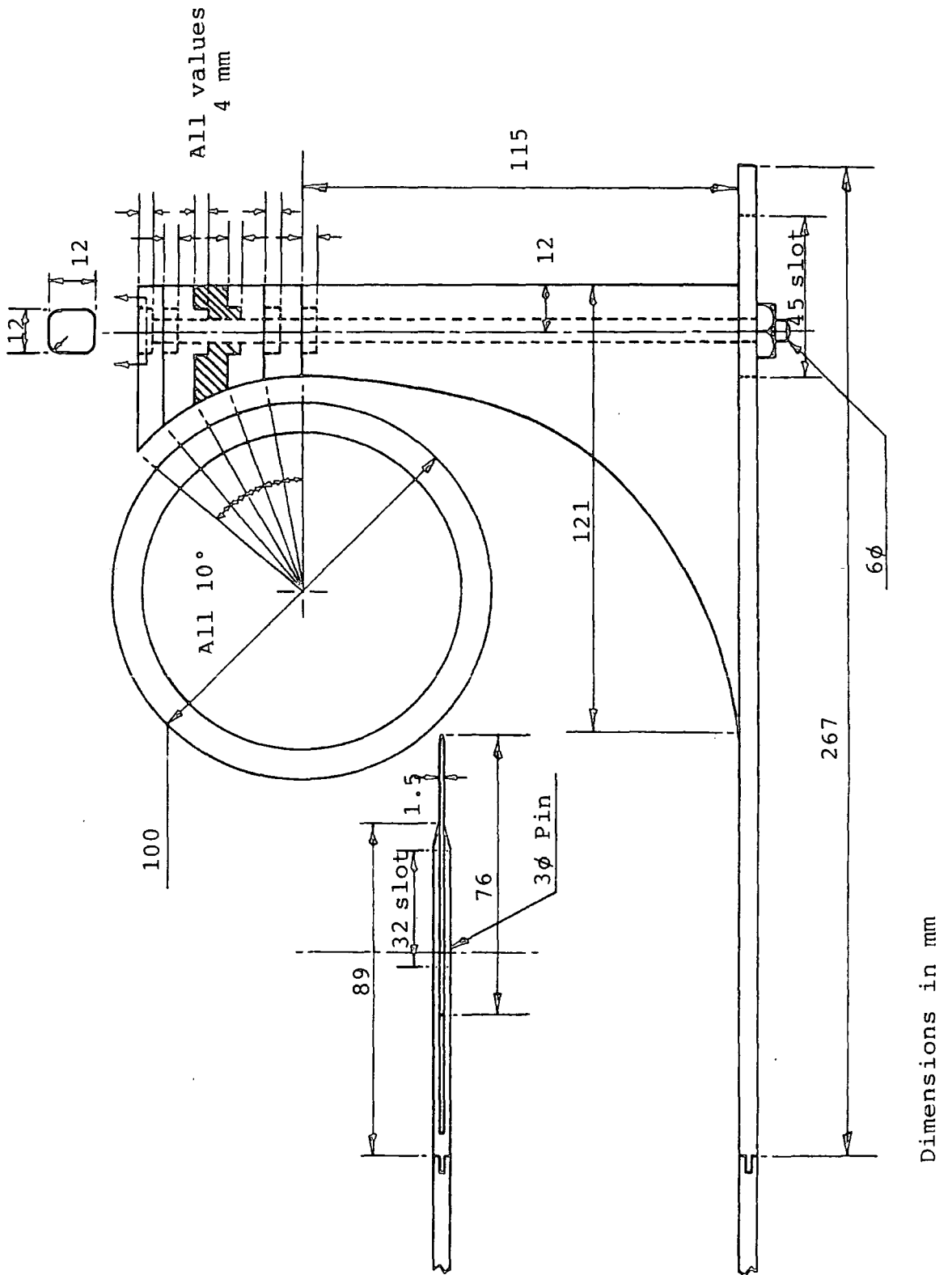
Figure 3.3(a)   VARIABLE GEOMETRY CASING
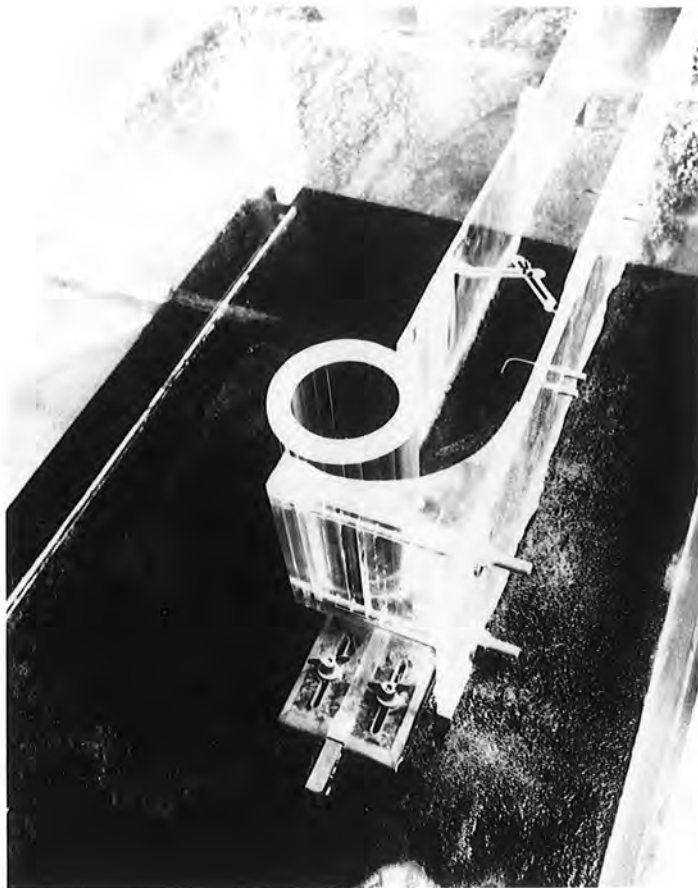
Figure 3.3(b)   THE VARIABLE GEOMETRY CASING AND ROTOR

edges of all duct walls, ensured firm location and pre-
vented leakage between the discharge and suction regions.

3.3.4 The Drive to the Rotor

The drive shaft attached to the lower end of the
rotor passed through a seal in the base of the tank,
shown in Fig. 3.2 . The power was transmitted from a 0.5
h.p., a.c. motor to the rotor shaft by a system of timing
belts and pulleys. Self-aligning plummer block bearings
were used througout.

3.3.5 Tank Flow Guide Walls

To avoid excessive swirling of water within the tank
an internal channel was installed, which directed the
flow from the fan discharge smoothly towards the test
section. Downstream of the test section, the vortex wall
could be adjusted which allowed the tank to be 'trimmed',
regulating the flow rate in the channel.

Honeycombs, water-proofed by coating in laquer, were
positioned at the outlet of the channel and at the top
end of the test section which eliminated any remaining
eddies in the water flow prior to entry into the fan
suction region.

3.4 Photographic Materials and Techniques

A Canon AE1 fitted with a Canon FD 50mm. F1.4 S.S.C. lens

was used throughout the visualization study. Automatic light metering was utilized in nearly all cases whereby the shutter speed was given priority over the f number.

Kodak Tri-X 35mm. roll film was chosen as an appropriate recording emulsion. The film was developed using Tetenal Neofin Red because its greater developing power 'pushes' the film speed resulting in a much improved contrast. This developer also reduces the normal graininess associated with high speed film by chemically affecting the total negative at an equal rate, independant of local densities. This prevents the usual clumping of the silver halide crystals.

After neutralising the developer in an acid stop bath, the film was fixed for twice the clearing time. The contrast was further enhanced by printing on grade 4 paper.

3.5 Experimental Procedure

The base of the tank below the test section was painted with matt black paint to eliminate unwanted reflections and provide a suitable photographic background. Illumination was provided by three high-power halogen strip lamps forming a 6mm. thick slice of light transversely across the tank at the mid-span position of the rotor. The two lamps positioned adjacent to the test section   contained 1kW lamps, while the lamp opposite the test section, a 1.5 kW lamp. This arrangement provided an even light level in and around the rotor.

The camera was mounted on a tripod directly above the axis of the rotor by aligning the microprism focussing ring concentrically with the rotor. A ruler clamped in a retort stand and positioned directly in the slit beams allowed accurate focussing and provided a scale for future streak measurements. Whenever the film was changed or the camera repositioned, an updated photograph of the scale was required.

3.5.1 The Rotor in Unbounded Fluid

Initially, no casing components were used to study both the transient flow at start-up and the steady state flow. To examine the transient flow process, the rotor was accelerated to full speed within one second and the shutter released remotely at some arbitrary time after start-up. Repeated shots were taken of this process and straightforwardly placed in temporal order as judged by the development and position of the vortex and the general magnitude of the velocity vectors.

The steady state flow was examined by taking several photographs in quick succession once a particular type of flow was stabilised. Various types of flow were achieved by 'trimming' the tank, as discussed earlier.

3.5.2 The Rotor with Casing

The vortex wall and rear wall leading edge clearances were both set to $0.05D_2$ as it was unclear how these

parameters would affect the conditions for dynamic similarity with the aerodynamic rig. Table 3.1 shows the possible range of all the variable parameters. Main consideration was given to tests where dynamic similarity with the aerodynamic rig was maintained.

Shutter speeds between 1/4 and 1/30 s. were used. The former gave an overall flow picture and the latter detailed flow in the suction region.

3.6 Results and Conclusions

The recorded photographic streaks represented the displacements of the neutral density polystyrene beads and the corresponding directions of motion. The local velocities were calculated from the known shutter speed and the scale appearing in the first frame of each film. The co-ordinate of each velocity vector was that at the mid-point of the corresponding streak.

3.6.1 Rotor in Unbounded Fluid

Two distinct types of steady state flow were found to occur, depending on the 'trim' of the channel walls. The first resulted in minimal throughflow and produced a totally forced vortex flow in and around the rotor with the streamlines concentric with the vortex core (see Fig. 3.4). The vortex centre was continually hunting in the direction of rotation of the rotor and occasionally moved radially away from the axis.

Table 3.1

Adjustable Parameters on Hydrodynamic Facility

Parameter	Symbol	Range
Rear Wall height	α_1	$0°$ to $50°$, steps of $10°$
Rear Wall Clearance	e_1/D_2	2% to ∞
Vortex Wall Height	α_2	$90°$ to $-90°$
Vortex Wall Clearance	e_2/D_2	2% to ∞
Vortex Wall Diffusion Angle	α_2'	$0°$ to $30°$
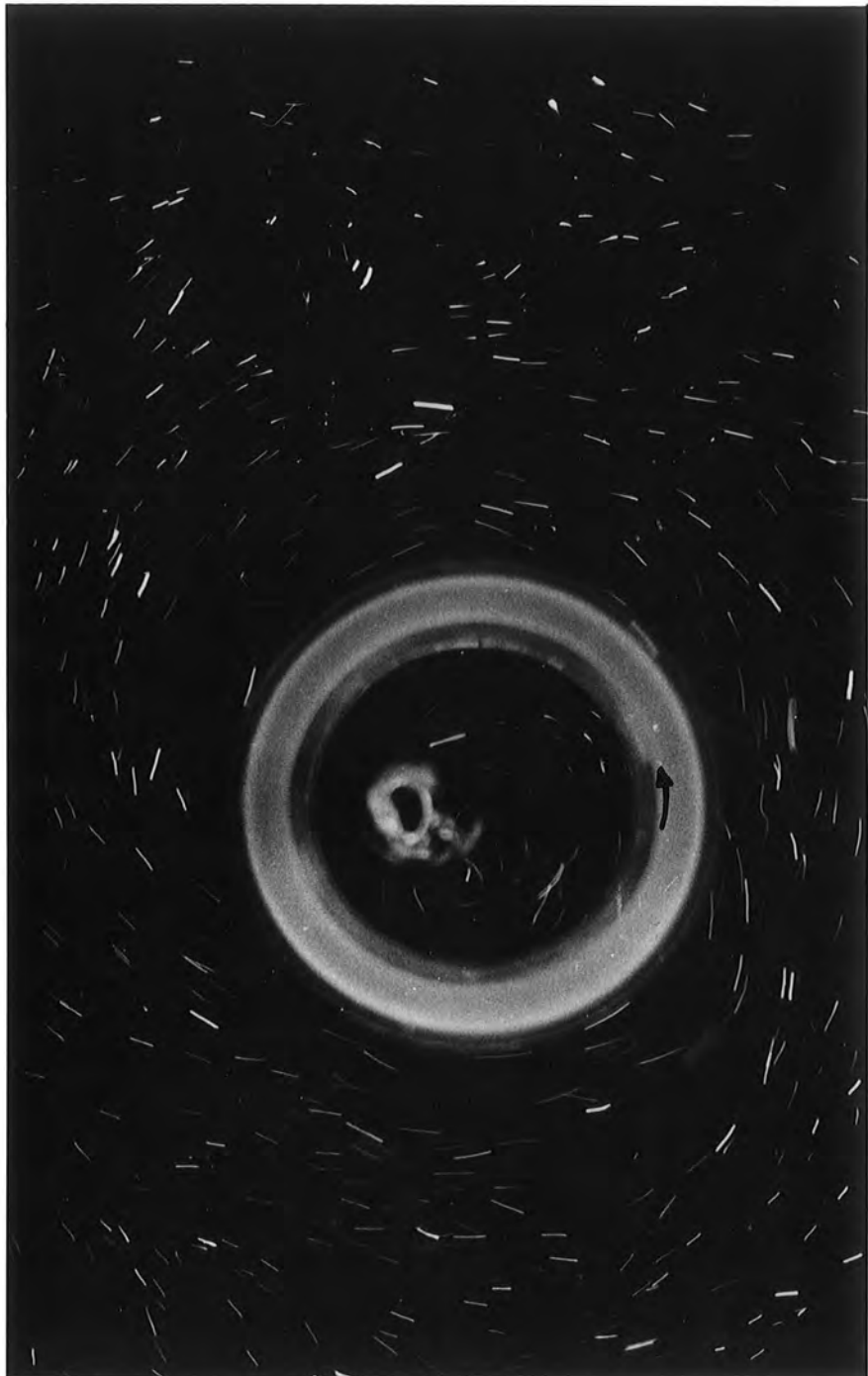
Figure 3.4   ROTOR WITHOUT CASING: STEADY STATE FLOW I

U_2 ⊢

The second type of flow produced a more familiar pattern with the vortex on the inner periphery of the rotor and substantial throughflow. At times, the vortex would find a stable location which was maintained for several seconds before hunting in the direction of rotation of the rotor. During stable periods, it was possible to identify a dividing streamline between the suction and discharge regions which might indicate the ideal location for the vortex wall (a dividing streamline in itself). Figure 3.5 illustrates this flow during a stable period, showing vortices shed from the vortex core and passing downstream, caused by small perturbations in the vortex position. These seem to be a major cause of pulsations and instability of the discharge flow.

Photographs of the transient flow during start-up, were of great interest. The geometry of the tank recirculation channel was arranged for steady state flow of the second type, as discussed above. Initially, a number of vortices formed on the inner perphery of the rotor, each rotating in the same sense as the rotor. The action of these individual vortices caused localised throughflow and viscous forces caused the region surrounding the rotor axis to rotate in an opposite direction. As this central region began to gain in strength the outer vortices diminished. A sudden transition occured as the rotation of this region change sense and as the throughflow began, the vortex moved towards a stable position on the inner perphery.

Photographs of this process always show an odd number of vortices present on the inner periphery, although symmetry

Figure 3.5 ROTOR WITHOUT CASING: STEADY STATE FLOW II

U2 $\longmapsto$

88

seems to be the only requirement. Groups of three, five and seven were observed with the occasional vortex generated on the outer periphery (see Fig.3.6, for example). The latter stages of the transient process were deduced from observation as from the large number of photographs taken, none managed to capture the final rapid vortex formation without excessive blurring of the detail.

A HYCAM 16mm, high speed cine camera was used to record this process. Due to the relatively low light levels, it was not possible to obtain individual photographs with the clarity of the 35mm photography. However, the general transient characteristics described above, were still present. A diagram representing the possible stages of vortex formation within a spinning cylinder is illustrated in Fig.3.7.

YAMAFUJI (Ref.28) investigated the formation of the eccentric vortex using solid particles sprinkled on a free surface and the moire method of topography. He showed that each blade trailing edge (inner periphery) produced a small vortex which coalesced with its neighbour, finally producing a large vortex within the impeller which moved to the inner periphery. Problems arise with this experiment because of the surface waves produced by the blades which pierce the free surface. These can be seen to cause interference making the flow pattern apparently more complex.

The moire method has been used successfully for contouring waves produced by ship models for drag estimations but is really not suitable for this application.

The transient process seems to be a specific case of a more generalised flow. The rotational acceleration of

Figure 3.6(a)   ROTOR WITHOUT CASING: TRANSIENT FLOWS
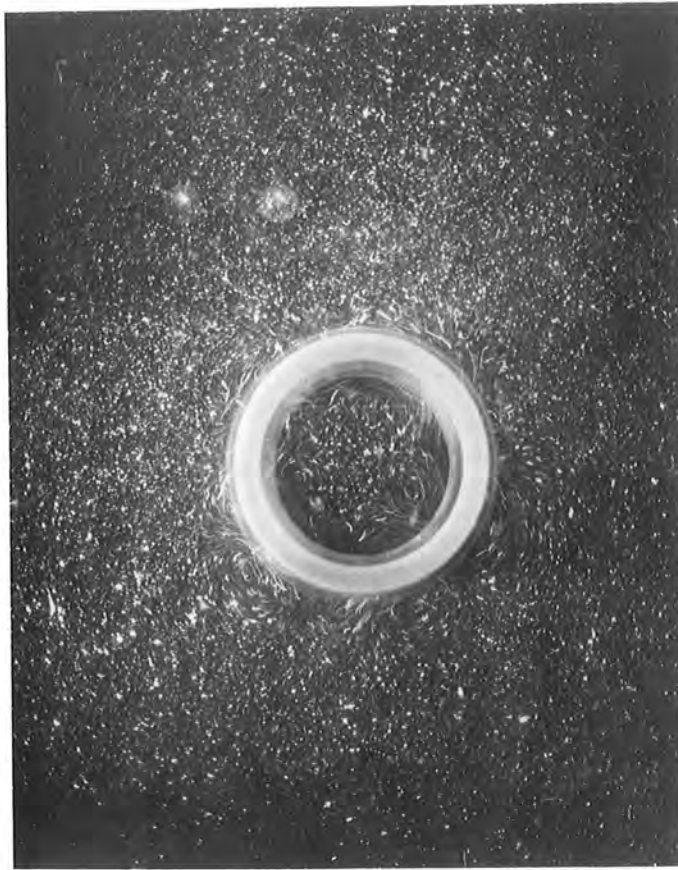
Figure 3.6(b)   ROTOR WITHOUT CASING:· TRANSIENT FLOWS

91

A. Forced vortex originates from primary vortex
B. Forced vortex originates from secondary vortex
C. Forced vortex originates from tertiary vortex

Primary vortices

A

B

C

Final forced vortex flow

Secondary and tertiary vortices
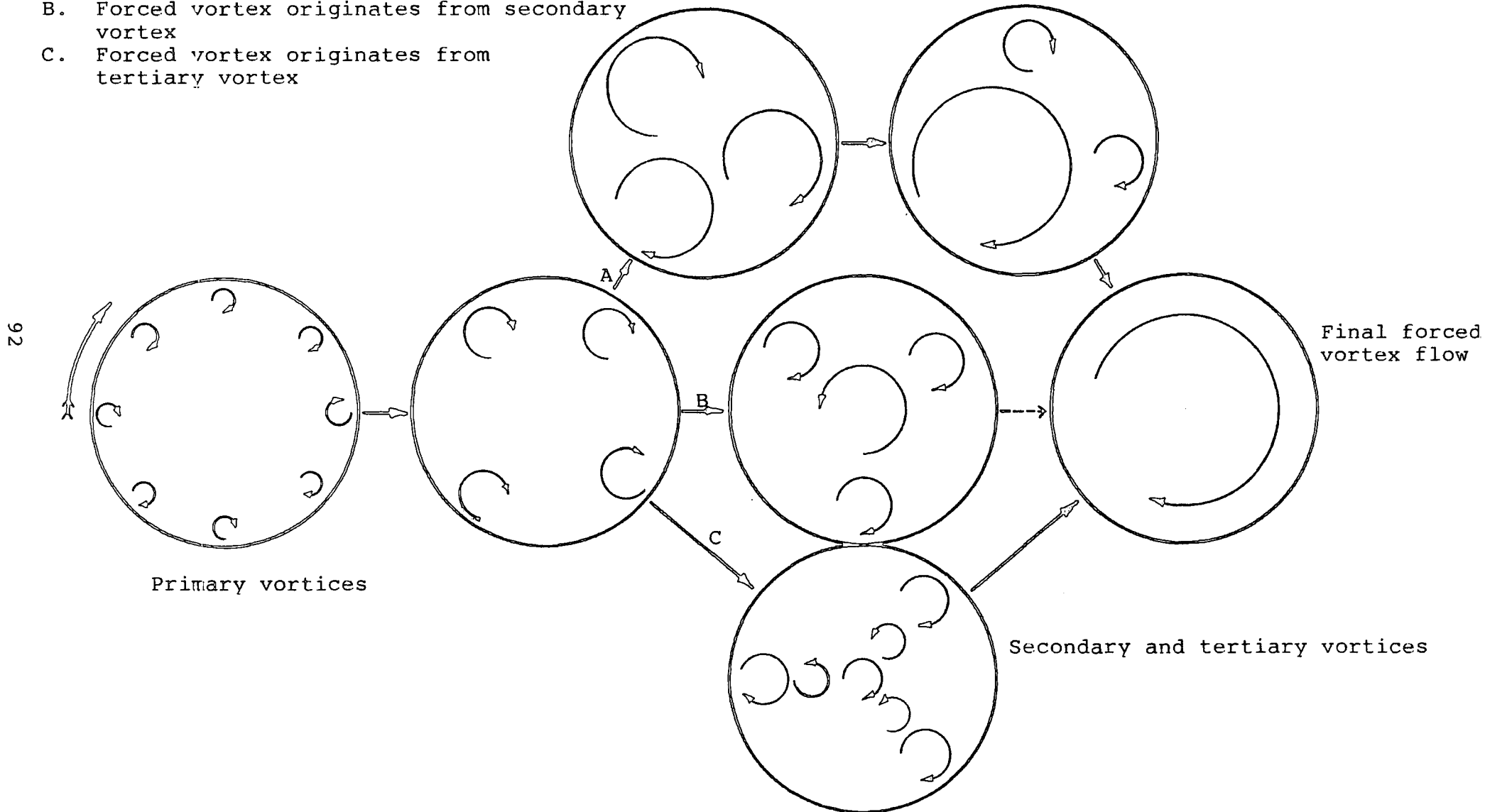
Figure 3.7 VORTEX FORMATION IN AN ACCELERATING CIRCULAR CYLINDER

a hollow cylinder submerged in fluid, where the viscous action between the solid and liquid produces high shear stresses at the interface causes the formation of small vortices around the inner periphery and finally results in a forced vortex centred on the cylinder axis. Once this is formed, the true cross flow action begins.

3.6.2   The Rotor with Casing

For each photograph, velocities in the various regions were determined from a knowledge of the camera shutter speed and the scale appearing in the first frame of each film. The information extracted from each of the photographs took the form of:

(i) the effective inflow arc (this is different from the geometrical inflow arc),

(ii) the general behaviour of the flow in the suction region,

(iii) the flow velocities in the suction region,

(iv) the size and velocity of the discharge jet over the rear wall,

(v) the general behaviour of the flow in the interior region,

(vi) the flow velocities in the interior region,

(vii) the position of the vortex core,

(viii) the effective outflow arc (different from the geometrical outflow arc),

(ix) the general behaviour of the flow in the discharge region, and

(x) the flow velocities in the discharge region.

From the resulting data it was possible to identify

discrete zones of flow within the suction, interior and discharge regions, as shown in Fig.3.8.

3.6.2.1 Flow in the Suction Region

The zones identified within the suction region were:
a) an inflow zone covering an arc beginning at the vortex wall leading edge,
b) a discharge jet from the rotor interior covering an arc beginning at the leading edge of the rear wall, and
c) a zone of entrained flow resulting from the jet over the rear wall.

For the fan operating under medium throttle conditions, the flow in the suction region exhibited all three regions. Figure 3.9 shows the high velocity region close to the vortex wall where the majority of the flow enters the fan (region a) with velocities in this region estimated at 0.5 U_2. The geometric suction arc consists of 80% inflow, with the remainder comprising the jet (region b) and its associated entrainment (region c). The velocity of the jet region is the order of the blade speed, showing clearly that the origin of the flow lies within the fan interior. (see Fig 3.10 .

The suction region velocities for a throttled fan are little different from those of the full flow condition. However the inflow arc then diminishes to 50% of the geometric arc, with the rear wall jet becoming increasingly dominant containing flow velocities up to 3.0 U_2. This jet region appears to be a major source of losses and hence

94

Arc_in

a

c

h_jet

i

h

V_jet

b

θ_d

V_in

V_int

g

Vortex Wall

f

e

d

l

Arc_out

j

Rear Wall

k

V_out
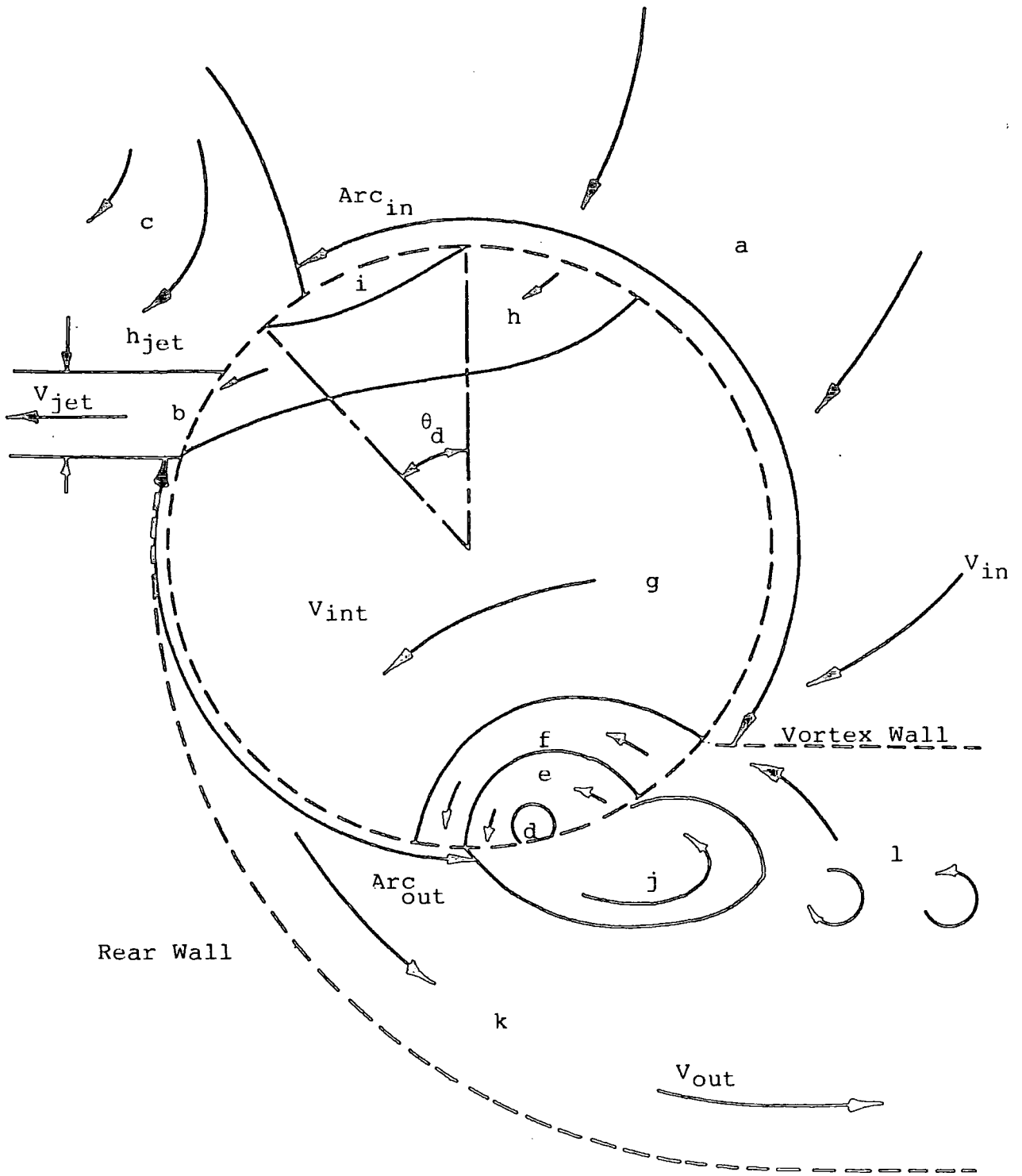
Figure 3.8   REGIONS OF FLOW
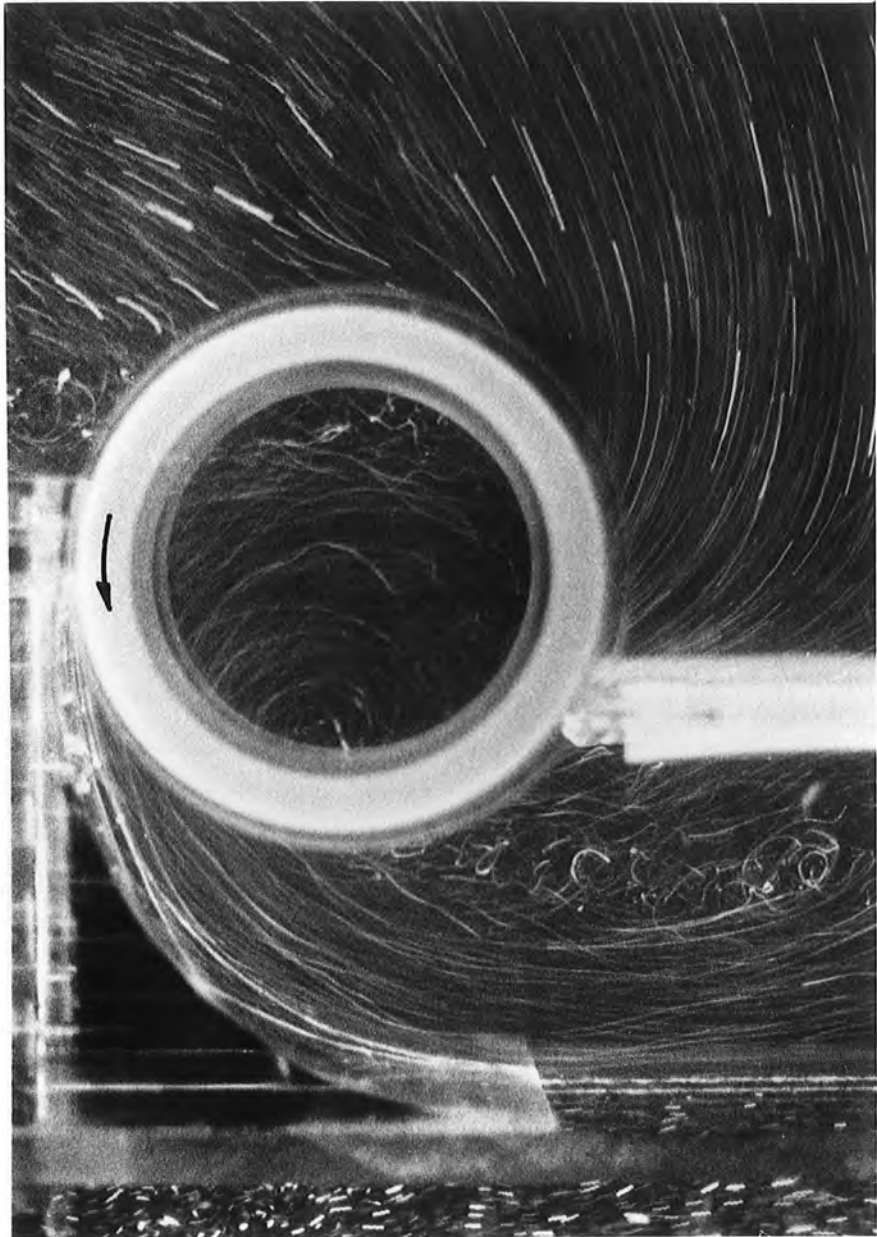
Figure 3.9   MEDIUM THROTTLE, $\alpha_1 = 20^\circ$

U_2 |————————————————|
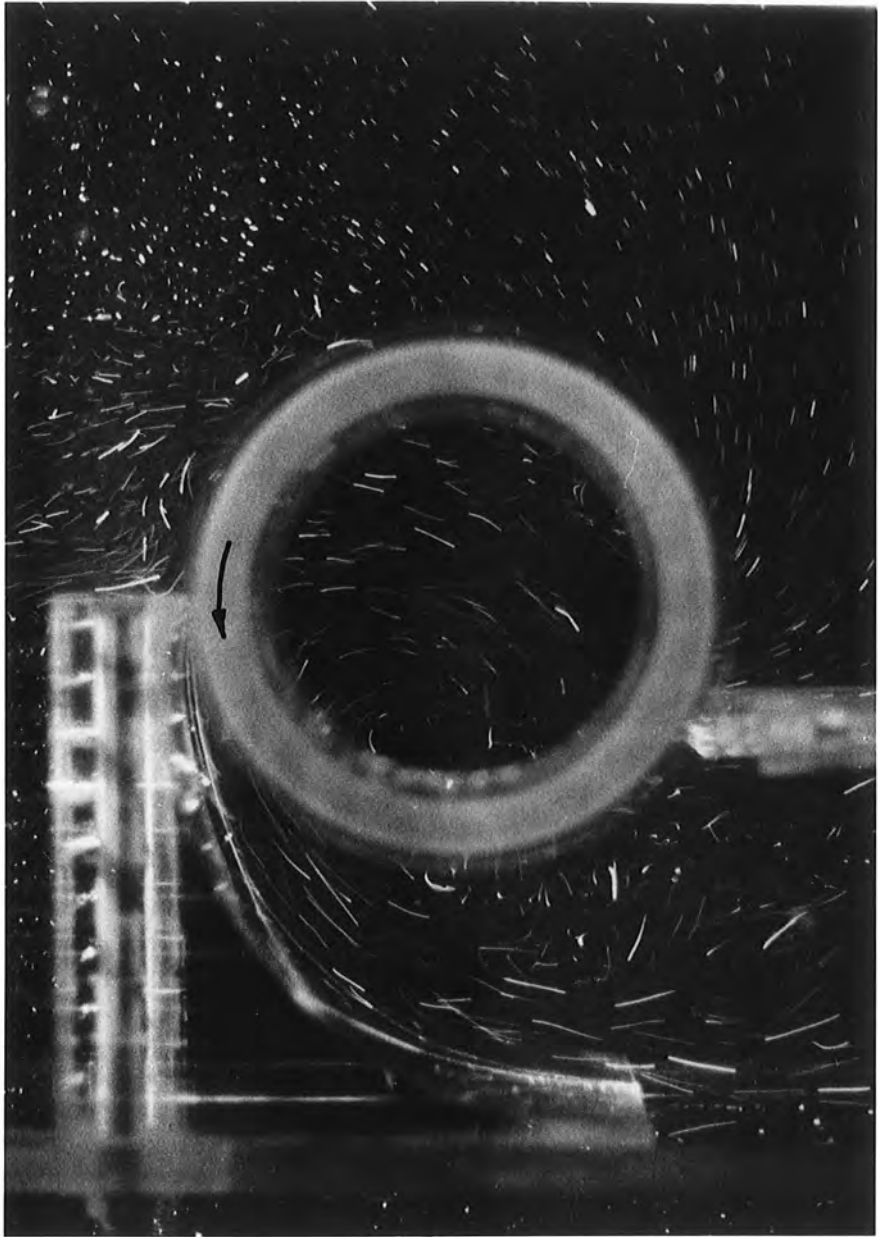
Figure 3.10   HIGH THROTTLE, α_1 = 0°

U_2 ⊢⊣

97

poor efficiency of cross flow fans. A study by PELHAM
(Ref.21) showed a similar result from tests on the aero-
dynamic facility (Chapter 2).

On removing the 20° extension to the rear wall, the
jet region became more extensive and contained flow velo-
cities lower than those previously recorded. Furthermore,
the total inflow arc was also reduced. When the rear wall
extension was raised to 50°, the jet became smaller and
the flow velocities higher. The total inflow arc was also
smaller than the 20° extension case. Figures 3.10 and 3.11,
show these two cases at zero flow, where they were found
to be most dominant. Finally, under no conditions of
casing geometry and flowrate did the inflow arc equal the
geometrical arc.

3.6.2.2   Flow in the Interior Region

The zones identified in the interior region were:

d) a forced vortex core,

e) a recirculating flow return path from the discharge
region,

f) a return flow path from the discharge region below the
vortex wall,

g) a through flow path,

h) a throughflow path from the suction region to the dis-
charge jet over the rear wall, and

i) a low energy random zone.

The interior flow clearly shows the vortex core (region
d) and the turbulent low energy region diametrically

opposite (region i). As the fan outflow was throttled, the vortex moved by about 15° peripherally towards the rear wall but did not move significantly in a radial direction. Figure 3.12 is a high contrast, slow shutter speed photograph, which shows the vortex core and a surrounding fainter region which corresponds to the flow returning from the discharge region below the vortex wall (region e).

The flow visualization reveals that the interior flow field is rather different from those proposed in mathematical models and this divergence will be discussed in Chapter 4. The disturbed region within the impeller (region i) was always most predominant under low throughflow conditions and the pressure distributions found throughout the impeller of the aerodynamic rig, showed similar trends (see Chapter 2).

3.6.2.3 Flow in the Discharge Region

The zones identified in the discharge region were:
j) a turbulent recirculation zone from the fan interior,
k) a diffusing throughflow zone, and
l) a flow path under the vortex wall, returning essentially laminar flow to the fan.

Figure 3.9 illustrates the outflow arc covering 65% of the geometric arc before meeting the recirculation region (region j) where vortices are seen to be shed from the main vortex core. The flow under the vortex wall is returning towards the fan (region l). The velocities in the discharge region are approximately 3.0 U_2 (region k).

Figure 3.12 HIGH THROTTLE, α_1 = 20°

U_2 ⊢———⌁———⊣

Figure 3.13 illustrates the zero flow criterion and shows the large recirculating region in the fan discharge (region j). It is important to appreciate that zero flow relative to the fan cannot exist by throttling the outlet duct as flow is always maintained through the fan owing to recirculation within the duct. A true zero flow condition can only be imposed using a damper installed adjacent to the fan outlet and extending over the geometric arc. The vortex then moves to the centre of the rotor and the interior flow field becomes that of a forced vortex.

3.6.2.4 The General Flow Field

The size and associated velocities of the zones discussed in Section 3.6.2.3 were found to be entirely dependent on the flow rate passing through the fan. Table 3.2 summarizes the photographic records taken for the 0°, 20° and 50° extensions to the rear wall, with the specific parameters labelled on Fig.3.8. Figure 3.14 illustrates a more general view of the total flow fields mentioned previously and clearly indicates that the cause of pulsations found during the use of many of these units stems from the shed vortices and recirculation in the outlet duct.

Figure 3.13 ZERO FLOW CRITERION, α_1 = 20°

U_2 |—⌵—|

103
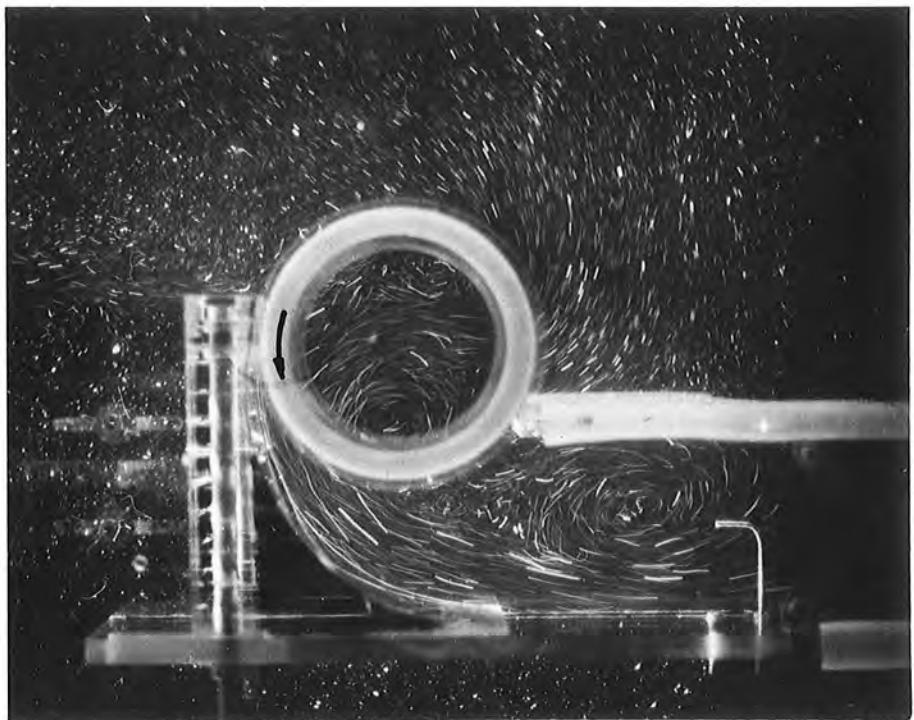
Figure 3.14   GENERAL FLOW FIELD, α_1 = 20°

104

α_1 (deg)	Throttle (increases with more *)	Inflow Arc (deg)	V_{in}	V_{jet}	h_{jet}	Vortex Position (deg)	Vortex Size	Extent of Disturbed Region, θ_d	Interior Velocity V_{int}	Outflow Arc (deg)	V_{out}	Outflow Quality (the more * the better)
0	*	154	$0.75u_2$	$1.0u_2$	$0.2r_2$	275	$0.17r_2$	81	–	96	$3.0u_2$	****
0	**	131	$0.50u_2$	$1.5u_2$	$0.4r_2$	295	$0.30r_2$	62	$1.7u_2$	84	$2.0u_2$	*****
0	***	116	$0.63u_2$	$1.0u_2$	$0.51r_2$	289	$0.50r_2$	61	$3.0u_2$	71	$1.7u_2$	**
20	*	158	$0.48u_2$	$1.0u_2$	$0.19r_2$	279	$0.37r_2$	95	$3.0u_2$	91	$3.0u_2$	***
20	**	128	$0.58u_2$	–	$0.25r_2$	290	$0.50r_2$	65	$1.5u_2$	80	$2.5u_2$	**
20	***	101	$0.57u_2$	$2.0u_2$	$0.31r_2$	292	–	75	$1.0u_2$	72	$3.0u_2$	***
50	*	153	$0.70u_2$	$0.35u_2$	v.small	281	–	75	–	91	$3.6u_2$	**
50	**	121	$0.63u_2$	$0.60u_2$	$0.21r_2$	290	–	57	–	84	$3.0u_2$	***
50	***	99	$0.70u_2$	$2.5u_2$	$0.38r_2$	292	–	29	–	71	$3.0u_2$	*

Table 3.2   Summary of Photographic Records

CHAPTER FOUR

THEORY OF THE CROSS FLOW FAN

"One cannot escape the feeling that these mathematical formulas have an independent existence and intelligence of their own, that they are wiser than we are, wiser even than their discoverers, that we get more out of them than was originally put into them.

Hertz

4. THEORY OF THE CROSS FLOW FAN

4.1 Introduction

As yet, no theory exists which satisfactorily explains the basic operation of the cross flow fan. Since its introduction by Paul MORTIER of France in 1891, numerous workers have puzzled over this problem with limited success. Only methodical experimentation has made a significant contribution to the development of the cross flow fan. However, this too, has proved to yield results which are at times confusing and inconsistent. There is little doubt that a predictive performance theory would benefit the design engineer but analytical attempts have provided only partial answers to this enigma.

Without a proper understanding of the processes of energy transfer and the consequent losses, it is not possible to make even crude predictions. This forces severe limitations upon the future development of this blower. Even so, the theoretical models postulated during the last 25 years have given some clues, which a few research workers have put to good use, often providing a guide to experiment.

A brief summary of cross flow fan theory is given by the author in ref. 27. In this chapter, the author intends to review some of the more important papers and finally to extend the work of IKEGAMI and MURATA (ref. 13).

4.2   The Theory of COESTER

Robert COESTER (ref. 7.) worked in Switzerland on cross flow fan theory and experimentation during the period of great research activity between 1955 and 1957. His was the first detailed theoretical exploration of the fan's principle of operation and the flow fields likely to be encountered within the impeller. An experimental study of the flow on either side of the blade row gave rise to the conclusion that the flow within the impeller consisted of two zones, which he describes as;

(i) a region of approximately constant total pressure and

(ii) a region of random, low energy flow, i.e. low total pressure.

(It is by no means obvious why COESTER described the flow in the forced vortex region as random or low energy, as in fact it is highly organised.)

These correspond to the free and forced vortex zones, respectively. COESTER's experiments indicated that the boundary between these two zones was well enough defined that a streamline of constant static pressure (i.e. constant velocity) enabled the so called 'dead water zone' to be removed from the flow altogether. This left a two-dimensional potential field for analytical treatment using Laplace's equation in polar co-ordinates.

$$\nabla^2 \phi \ (r,\theta) = r \frac{d}{dr}\left\{ r \ \frac{d\phi}{dr}\right\} + \frac{d^2\phi}{d\theta^2} = 0 \qquad (1)$$

A general solution obtained by the method of separation of variables was found to be

$$\phi = \sum_n r^n (a_n \sin n\theta + b_n \cos n\theta) \qquad (2)$$

which may be superimposed upon other solutions as it is

a harmonic and analytic solution of Laplace's equation.

The boundary condition on the inner periphery of the rotor,

ensured the velocity potential function became unique

$$\phi(1,\theta) = F(\theta)$$

for $r = 1$ and the most logical form for the periodic $F(\theta)$

being a Fourier series

$$F(\theta) = \sum_n (a_n \sin n\theta + b_n \cos n\theta) \qquad (3)$$

Defining $F(\theta)$ as a polynomial allowed a variety of boundary

conditions to be considered

$$F(\theta) = \sum_m A_m \theta^m \quad -\Pi < \theta < \Pi \qquad (4)$$

and the fourier coefficients were then written;

$$a_{nm} = \frac{A_m}{\Pi} \int_{-\pi}^{\pi} \theta^m \sin n\theta \; d\theta \qquad (5)$$

$$\text{and } b_{nm} = \frac{A_m}{\Pi} \int_{-\pi}^{\pi} \theta^m \cos n\theta \; d\theta \qquad (6)$$

A solution of Laplace's equation was then expressed

$$\phi = \sum_m \sum_n r^n (a_{nm} \sin n\theta + b_{nm} \cos n\theta) \qquad (7)$$

the resulting value depending on the boundary conditions

applied. The Cauchy-Riemann relations yielded the ortho-

gonal expression for stream function

$$\psi = \sum_m \sum_n r^n (a_{nm} \cos n\theta + b_{nm} \sin n\theta) \qquad (8)$$

Initially, COESTER chose the simple case $m = 1$ and

found that substitution in eqns. (5) to (8) gave;

$$\phi_1 = 2A_1 \; \text{Arctan} \left(\frac{r \sin\theta}{1 + r \cos\theta} \right) \qquad (9)$$

and $\psi_1 = A_1 \ln \left\{ (1 + r \cos\theta)^2 + r^2 \sin^2\theta \right\}$ (10)

which produced a potential vortex with a core located at coordinate $(1, \pi)$ as shown in Fig.4.1 . Determination of the flow velocities was carried out using;

$$q_r = \frac{d\phi}{dr} \qquad\qquad (11)$$

and $q_\theta = \frac{1}{r} \frac{d\phi}{d\theta}$ (12)

and substituting from eqn. (9) gave;

$$q_r = - A \text{ Tan} \left(\frac{\theta}{2}\right) \qquad\qquad (13)$$

and $q_\theta = - A$, a constant   (14)

COESTER commented on these results, 'If a boundary condition q_θ = constant is assumed, the flow regime is that of a vortex with its centre on the rotor inner periphery and for such a vortex, q_r follows a tangent law; where $\theta = 0$ is at a point 180° away from the vortex core. Casings which attempt to guide the flow, other than in accordance with this law, will either be unsatisfactory or generate other vortices which will accommodate the situation.'

COESTER found that these conditions could only be satisfied with the blade angle on the inner periphery of the rotor, $\beta_1 = 90^{\circ}$ (which by definition implied q_θ constant, for perfect guidance through the blade row, i.e. an infinite number of blades). The calculation involving eqns. (7) and (8) was extended to include terms for m = 2 and 3. The solution obtained displayed an accelerated throughflow, with no streamlines of constant static pressure, as shown in Fig.4.2, and as such, the low energy
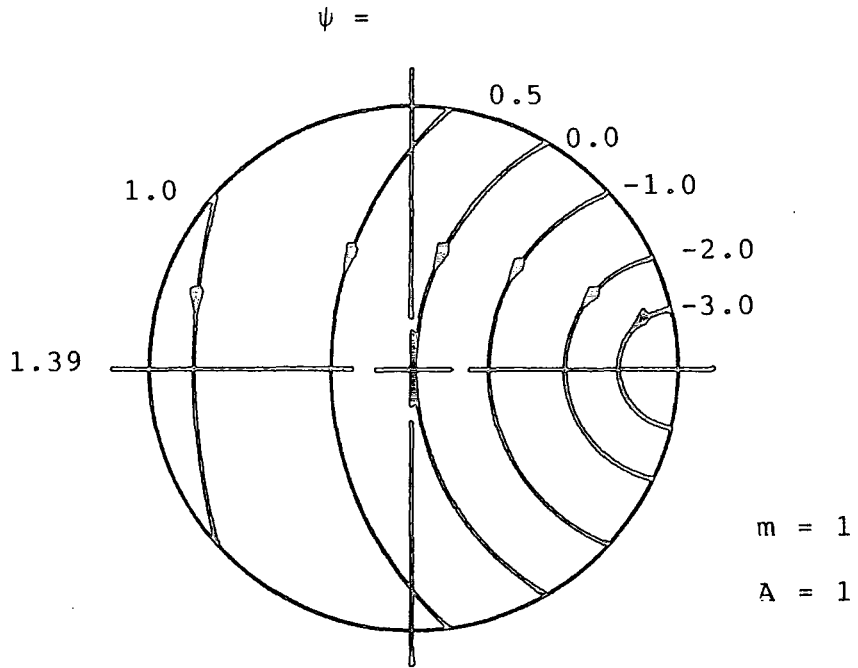
Figure 4.1   POTENTIAL VORTEX SOLUTION (COESTER)
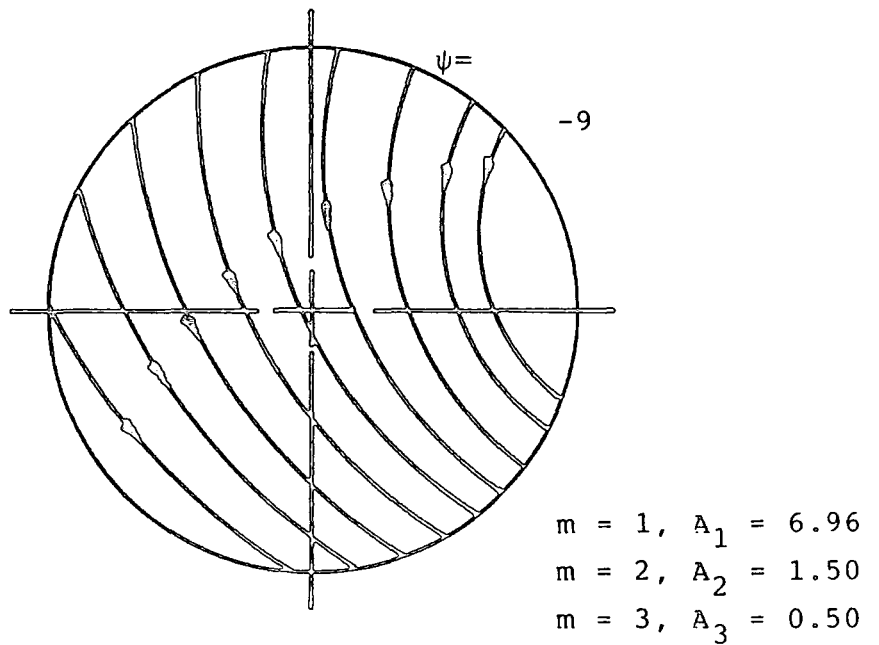
Figure 4.2   ACCELERATED FLOW (COESTER)

111

region could not be removed from the solution. To over-
come this, two unit vortices were introduced to achieve
the desired condition and this is shown in Fig.4.3. COESTER
then found it possible to choose q_θ and q_r independently
by selecting suitable constants to give the tangential com-
ponent of velocity and by adjusting the strength of the
unit vortices to change q_r. Establishing a line of
constant static pressure tended to limit the choice of q_r.

The resulting casing designs showed a marked similarity
to those of MORTIER, especially in respect of their close
fitting arrangement. In an attempt to improve the radial
velocity profile at exit from the rotor, COESTER included
a vortex opposite the main vortex, which increased the
energy of the flow farthest from the main vortex. This
was thought to remove the poor effect of a free vortex on
the distribution of energy at outlet and thus to improve
the pressure recovery in the diffuser. By moving this
vortex away from the symmetrical position, it was found
possible to either accelerate or decelerate the flow through
the rotor. Again, vortex distributions were needed to
reduce one streamline to a constant static pressure. COESTER
said about this situation that 'The creation of the vortex
opposite the main vortex, automatically causes the vortex
distributions to be formed, whether or not the housing
construction favours this.' (see Fig.4.4).

COESTER's later casing designs show direct evidence of
the use of this theoretical study, with a fairly complicated
housing geometry containing two large recirculating pockets
to presumably induce the vortex distributions described.(fig. 1.3)
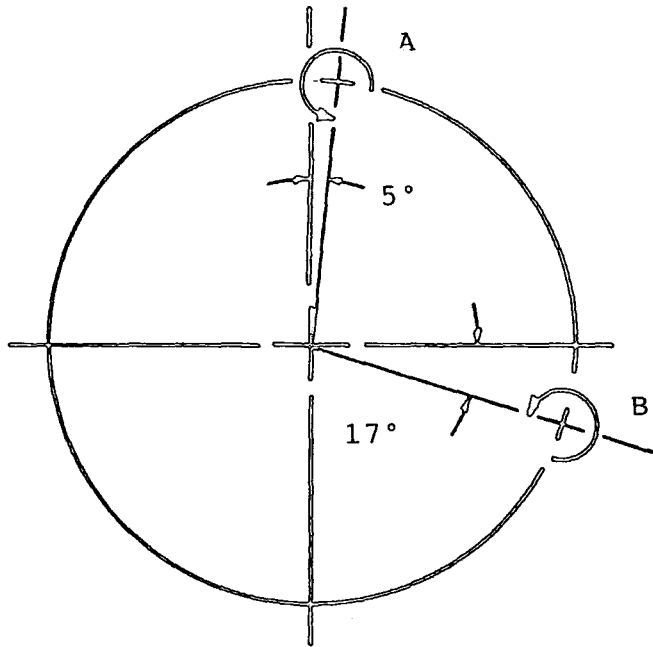
Figure 4.3 MODIFIED SOLUTION USING UNIT VORTICES (COESTER)
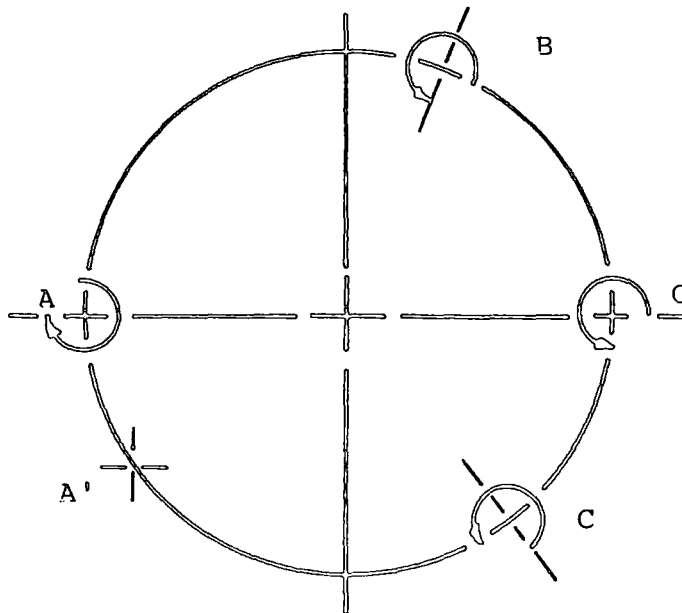
Figure 4.4 VORTEX DISTRIBUTION FOR IMPROVED OUTFLOW (COESTER)

113

However, this study applied essentially to a 'one-flow'
situation and as such, could not be used to determine
the performance characteristics. Although it was sensible
to position a recirculation pocket opposite the main vor-
tex, providing a more satisfactory energy distribution,
the recirculation pocket on the vortex wall was unnecessary
and a quirk of the mathematics. COESTER was saying 'what
sort of flow do we require and hence what model provides
that flow', whereas the purpose of the vortex distribution,
as described, was to isolate the throughflow from the
non-potential region so that Laplace's equation could be
applied with the right hand side zero. Nevertheless, this
was certainly the first attempt to describe the operation
of the cross flow fan using theoretical principles and his
experimental results did show minor improvements compared
with original casing geometries.

4.3 The Theory of ILBERG and SADEH

An experimental study of velocity and pressure through-
out the interior of a cross flow fan, was the basis for
the theoretical analysis of ILBERG and SADEH (ref. 15).
Like COESTER, they recognised the existence of a two-zone
flow field, with the exception that the core of the vortex
was treated as a forced vortex. The majority of the flow
within the impeller was said to obey the periodic potential
function.

$$\phi_I \left(\frac{r}{r_1}, \theta\right) = \sum_n \left(\frac{r}{r_1}\right)^n (A_n \cos n\theta + B_n \sin n\theta) \quad (1)$$

which when combined by superposition with a potential vortex given by

$$\phi_{II} \left(\frac{r}{r_1}, \theta\right) = \frac{\Gamma}{2\pi} \theta r \quad (2)$$

yielded a full description of the flow field outside the forced region. By treating the vortex core as a solid body, continuity of velocity was arranged at the interface between the forced vortex and the inner periphery of the rotor. Equating velocities between the free and forced vortex zones gave a value for the vortex strength, Γ, which when applied to eqn. (2) gave the final boundary potential function

$$\phi(1,\theta) = \phi_I (1,\theta) + \phi_{II} (1,\theta) \quad (3)$$

ILBERG and SADEH found that eqn. (1) converged rapidly with the coefficients A_n and B_n being determined by Fourier analysis and the previous knowledge of the boundary potential $\phi(1,\theta)$, from their experimental study. The velocities were calculated throughout the impeller interior, yielding a typical flow diagram as shown in Fig.4.5 and gave good agreement with the experimental results. As the flow field was not sufficiently general, no attempt was made to evaluate the fan performance.

ILBERG and SADEH did not confirm COESTER's model in two respects. First, their measurements revealed that the radial flow component did not equate to the tangent law, and second, their tests indicated that the tangential component varied considerably from a constant around the inner periphery. The apparatus used in these experiments
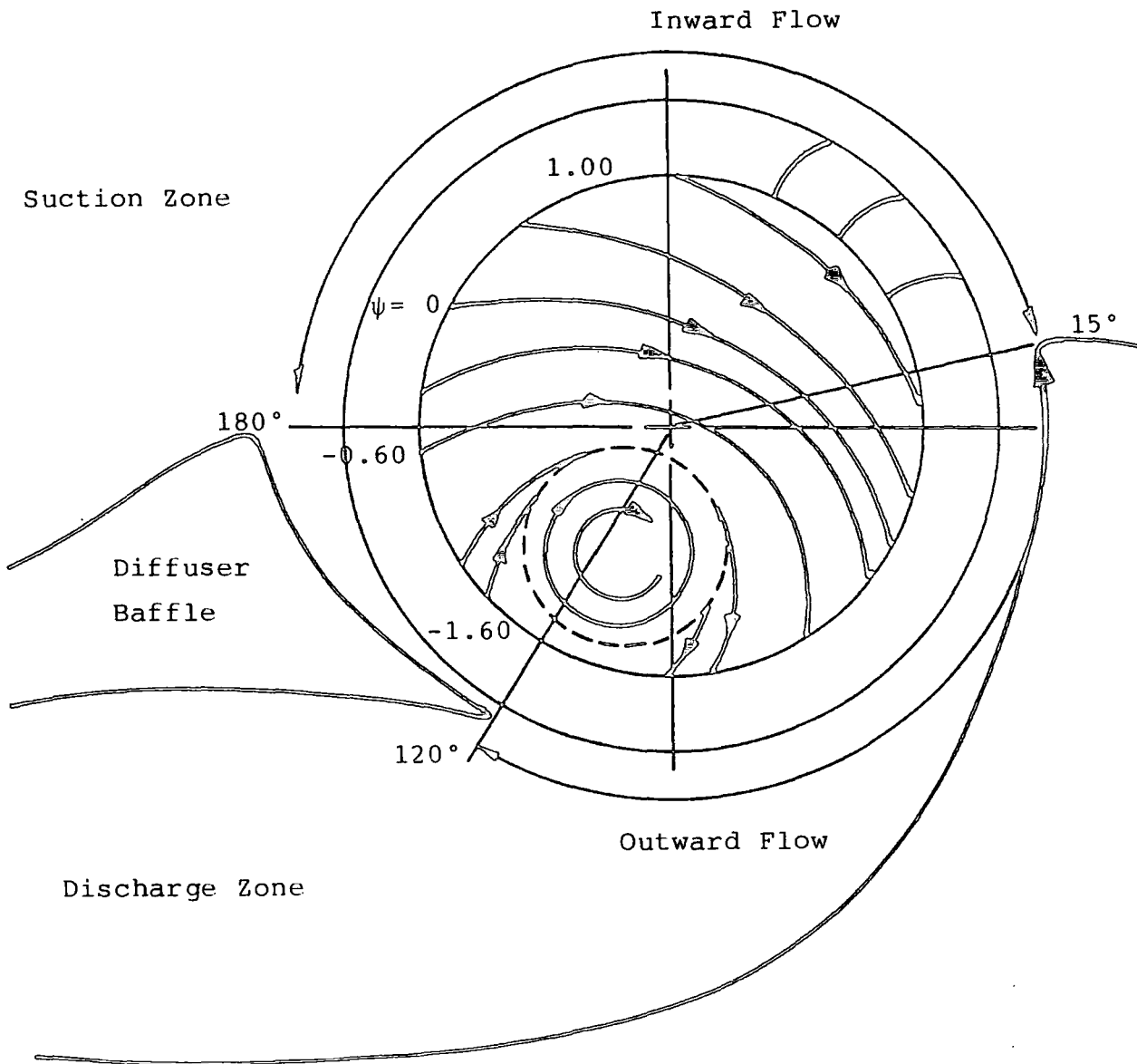
Figure 4.5   CALCULATED FLOW PATTERN (ILBERG AND SADEH)

may explain these discrepancies. The impeller had a very low aspect ratio of 0.25 and the non-drive end plate of the rotor was fixed. A secondary flow perpendicular to the main flow was described, which they attributed to the superposition of the flow caused by the rotor disc and the main flow but more likely, the pressure gradient across the rotor was caused by a boundary layer set up on the fixed end plate. Hence, the short rotor may have accounted for many of the flow properties encountered. The forced vortex region was treated as solid body rotation but the assumption of equivalent velocities on the boundary with the inner periphery, although intuitively correct, resulted in further problems which will be commented on in a later chapter. Finally, like the COESTER solution, this model was selected for a particular flow rate and consisted of fitting the developed theory to the experimental results. This analysis cannot be extended to predict the fan performance.

4.4 The Theory of MOORE

The paper of MOORE (ref. 16) stemming from work at the National Engineering Laboratory during 1972, derived the change in angular momentum between suction and discharge by the use of a mean line joining all the stations considered across the rotor, as shown in Fig. 4.6. The Euler head, Ψ, of a generalised impeller was written as a function of the flow coefficient, Φ. By examining this equation, MOORE was able to determine the contribution of
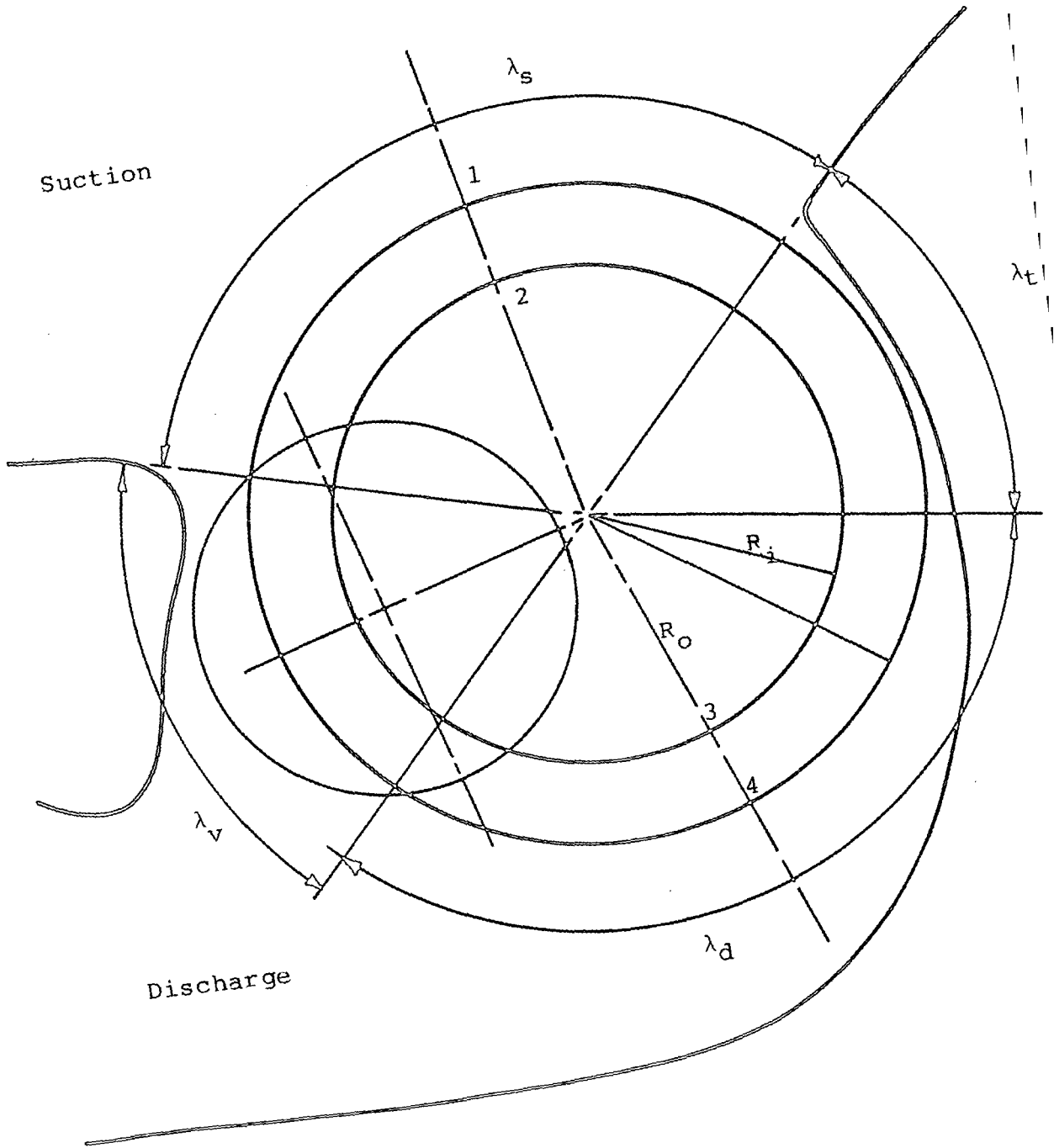
Figure 4.6   THEORETICAL FLOW MODEL (MOORE)

the inlet and discharge blade rows, to the total pressure rise. From this emerged the new concept of controlling the two-stage pressure generation, so that a characteristic could be obtained which would rise continuously from full to zero flow, with no possibility of the fan stalling. MOORE suggested that stability would be achieved by operating the first stage blades as a turbine over a portion of the flow range. The overall design procedure was iterative, relying on the correct choice of vortex strength to obtain the desired values for a particular casing geometry. MOORE added that the net value of total pressure rise, governed the inlet and hence exterior blade angles (β_2) with freedom of choice for the interior blade angles (β_1) being limited and essentially fixed by the ratio of the suction to the discharge arc.

There was good agreement with his experimentally evaluated results in some cases but in others, the correlation was poor and MOORE suggested that the general departure from the theory was due totally to the losses within the vortex. This, he explained from the equality

Total Power Input, $\gamma = \Psi \Phi +$ Power lost in the momentum

change in the vortex, γ_v

from which was obtained an expression for the power absorbed by the vortex

$$\gamma_v = \Phi \Delta\Psi$$

where $\Delta\Psi$ is the departure from theory.

MOORE's quest for a 'stable tangential fan' led him to a preliminary design which indeed produced a desirable performance characteristic. The departure from the

119

estimated Euler line suggested the power consumed by the vortex was high. He stated that all subsequent research should be directed towards reducing this loss, probably by means of an internal guide vane positioned to reduce the work done by the second stage blading in the recirculating region.

It appears that the line chosen to bisect the inlet arc, is an attempt perhaps to find a mean condition (see Fig.4.6). Experiments (ref. 21) have however shown that the bulk of the inflow occurs close to the vortex wall and his mean line is far from representing the mean flow.

It is doubtful whether a simple analysis of this sort can ever be expected to produce satisfactory results, given the extreme variation over both the inflow and outflow arcs.

MOORE attributed the majority of losses to those occurring within the vortex region. He states that up to one half of the input power could be dissipated with some designs. There will, of course, be losses occurring in the vortex region but others are present, such as the so called 'shock' losses, due to the relative flow angle departing from the inlet blade angle and this will be discussed later.

Although interesting to note that $\Delta\Psi$ was found to be virtually constant over the design range, MOORE's calculations also showed it could become negative, which implied that energy was being transferred from the vortex to the throughflow. Clearly this is unacceptable as energy cannot continuously be exchanged from the vortex but

may occur over an unstable transient period.

4.5   The Theory of IKEGAMI and MURATA

The work of IKEGAMI and MURATA (Ref.13) at Osaka
University during the period up to 1966 was novel in many
respects. It displays the possibility of a completely
analytic solution based on rotor geometry, with an internal
flow field allowing the vortex complete mobility within
the rotor. A simple casing was also included, providing
separation between the suction and discharge sides in the
form of a dividing streamline. This analysis is considered
so radical that the author intends to review this study,
in some detail, with consideration given to the progression
of thought and the generation of ideas as the theory unfolds.
From the abstract to their paper 'The authors tried to
calculate characteristics of a cross flow fan which consis-
ted of a simple linear casing and an impeller with an infi-
nite number of blades, on the assumption that the fluid was
non-viscous and incompressible'. They considered that
failing to realise the effect of casing configuration on
the performance, was the major defect in previous theories.
They later showed that the flow within the impeller could
not be judged as purely potential and their equations
included this possibility.

IKEGAMI and MURATA began the analysis with the suction
region which could be regarded as purely potential flow,
obeying LAPLACE'S equation in the form

$$\frac{d^2\psi}{dr^2} + \frac{1}{r}\frac{d\psi}{dr} + \frac{1}{r^2}\frac{d^2\psi}{d\phi^2} = 0 \qquad (1)$$

121

By considering the total head distribution around the inner periphery of the rotor

$$H(\theta) = \frac{p}{\gamma} + \frac{1}{2g} \ (C_r^2 + C_\theta^2) \tag{2}$$

and the equation of continuity between the suction side and some arbitrary position within the rotor

$$r_1 \ d\theta_1 \ C_{1r} = r \ d\theta \ C_r \tag{3}$$

it was found that the internal region could be described by

$$\frac{d^2\psi}{dr^2} + \frac{1}{r}\frac{d\psi}{dr} + \frac{1}{r^2}\frac{d^2\psi}{d\theta^2} = \frac{g}{r_1 C_{1r}} \ \left(\frac{dH}{d\theta}\right)_{r=r_1} \tag{4}$$

The use of Euler'S equation in conjunction with velocity triangle relationships across the blade row, showed clearly that the right hand side of eqn (4) was unlikely to be identically zero. This implied that every streamline within the impeller would have a different Bernoulli constant and in turn this suggested that the flow was not potential. As a first approximation, the difference in Bernoulli constant between streamlines was considered small and so the fundamental equation for this region reduced to eqn (1). The angular momenta at suction and discharge were examined assuming no external force acted on the fluid in the internal region (for the inviscid flow considered) and it was concluded that angular momentum was conserved across the rotor. Including this with the desirability for 'shockless' flow (achieved by setting $\beta_1 = 90°$), yielded the boundary condition for the internal flow field

$$C_{1\theta} = U_1 = \text{constant} \tag{5}$$

where U_1 is the blade tip speed on the inner periphery.

Before IKEGAMI and MURATA began this study, the flow inside the impeller had been widely analysed by using a single free vortex located on the inner periphery of the rotor, which satisfied the boundary condition of eqn (5). However, this model prevented movement of the vortex and also gave infinite capacity when the inlet and exit flows were separated by a dividing streamline, i.e. the casing. Figure 4.7 shows how these problems were overcome by the introduction of a second vortex of equal strength and the same direction, positioned on the same radial line but outside of the internal flow region. The radial co-ordinates for the vortices are ar_1 and r_1/a respectively giving increased flow rate as 'a' varies from zero to unity.

The stream function for this combination was evaluated by the superposition of the individual compenents and was given by

$$\psi = -\frac{\Gamma}{4\pi} \ln\left\{(r^2 + a^2 r_1^2 + 2arr_1 \cos\theta)(r^2 + \frac{r_1^2}{a^2} + \frac{2rr_1}{a}\cos\theta)\right\}$$
$$+ \text{ constant} \tag{6}$$

By differentiating eqn (6) to yield $C_{1\theta}$ and by including the boundary condition of eqn (5), the strength of the vortices was found to be

$$\Gamma = 2\pi r_1 U_1 \tag{6A}$$

and hence the full description of the internal flow field was written

$$\psi = -\frac{r_1 U_1}{2} \ln\left\{(r^2 + a^2 r_1^2 + 2arr_1 \cos\theta)(r^2 + \frac{r_1^2}{a^2} + \frac{2rr_1}{a}\cos\theta)\right\}$$
$$+ \text{ constant} \tag{7}$$

and Fig 4.8 shows a typical flow field based on eqns (1)
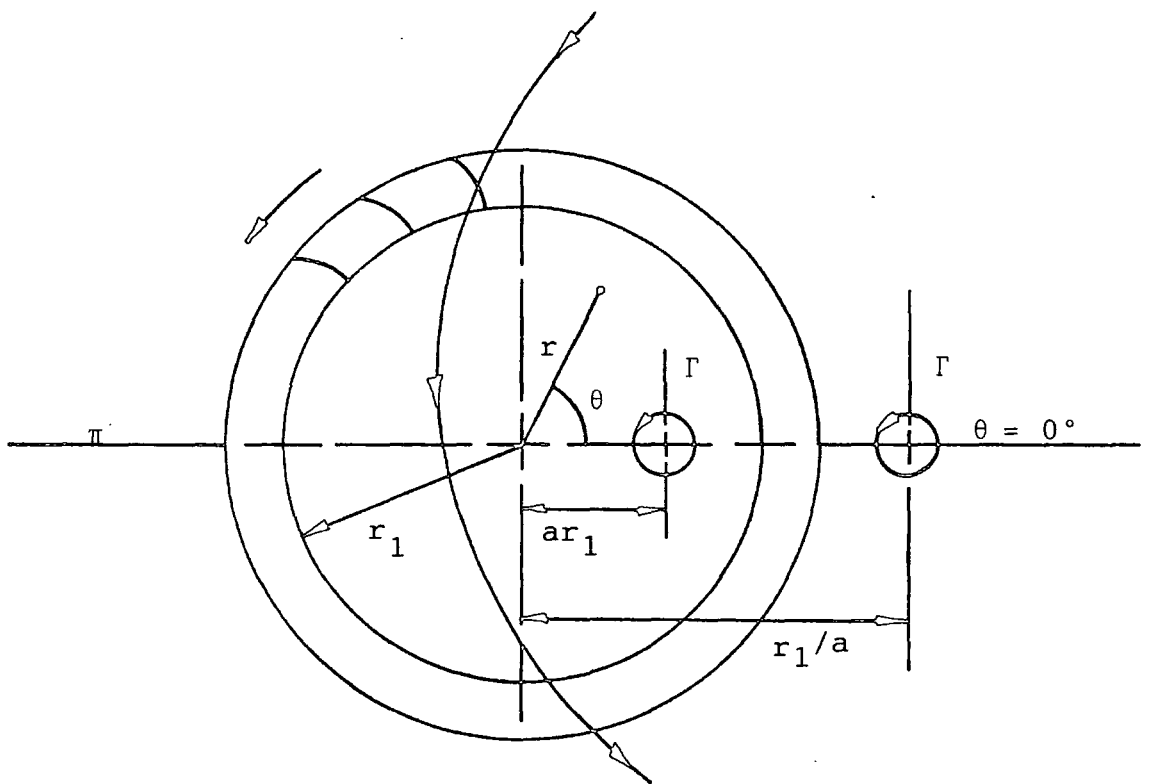
Figure 4.7   INTERNAL FLOW MODEL (IKEGAMI AND MURATA)
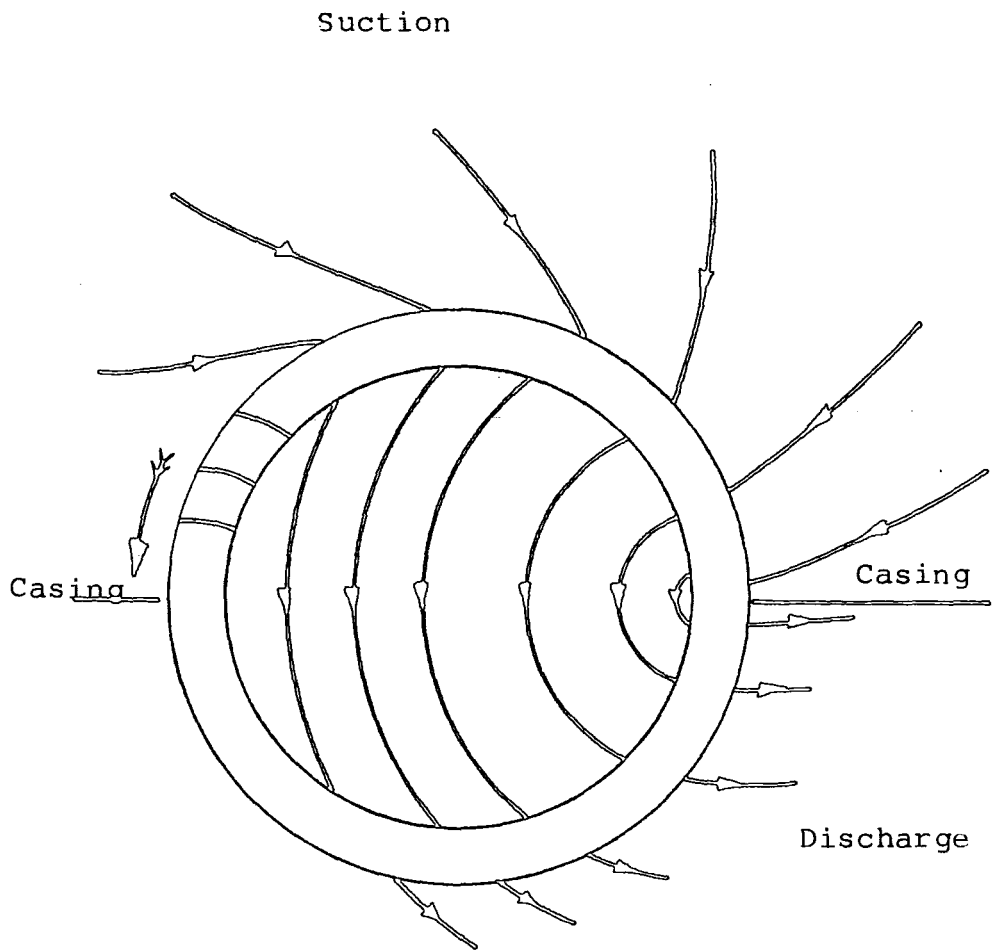
Suction

Vortex Core at a = 0.92, θ = 0°

Figure 4.8   THEORETICAL FLOW PATTERN (IKEGAMI AND MURATA)

and (7).

For the flow in the suction region, IKEGAMI and
MURATA used LAPLACE'S equation rigorously. The primary
solutions took the form;

$$\psi(r, \theta) = \Sigma_n \left\{ A_n \cos n\theta + B_n \sin n\theta \right\} \qquad (8)$$

and

$$\psi(r, \theta) = \Sigma_n \left\{ C_n r^n + D_n r^{-n} \right\} \qquad (9)$$

The product of these solutions was also a solution

$$\psi(r, \theta) = \Sigma_n \left\{ (A_n \cos n\theta + B_n \sin n\theta)(C_n r^n + D_n r^{-n}) \right\}$$

A periodicity was introduced to this function

$$\psi(r, \theta) = \psi(r, \theta + 2\pi)$$

which in turn implies that 'n' had to be integer and
therefore

$$\psi(r, \theta) = P + Q\theta + \Sigma_n \left\{ (A_n \cos n\theta + B_n \sin n\theta)(C_n r^n + D_n r^{-n}) \right\}$$

The boundary conditions applied to this flow field were:

(i) $\psi(r, \theta)$ to be finite for $r \to \infty$ and

(ii) $\psi(r, \theta)$ to be constant for $\theta = 0$ and π for $r_2 < r < \infty$

C_n was set to zero which satisfied condition (i) and for
both $\theta = 0$ and Π it was found

$$\psi(r, \overset{0}{\pi}) = P + Q\pi \overset{+}{-} \underset{n}{\Sigma} \frac{A_n}{r^n}$$

and if $A_n = 0$, was then independent of r which satisfied
condition (ii).

The total solution finally read

$$\psi(r, \theta) = P + Q\theta + \Sigma_n B_n r^{-n} \sin n\theta$$

which in the form of IKEGAMI and MURATA read

$$\psi(r, \theta) = k\theta + \Sigma_n \frac{Kn}{r^n} \sin n\theta + \text{constant} \qquad (10)$$

They achieved the evaluation of the unknown constants k and k_n by mathematically linking the equations for the suction and interior regions so that the streamlines of both were connected coherently at the outer periphery of the impeller. The equation of continuity was used in the form

$$\psi_{r = r_1} = \psi_{r = r_2} + \text{constant} \qquad (10a)$$

giving k_n' , shown to be a Fourier coefficient of a sine series.

$$k_n' = \frac{2}{\pi} \int_0^\pi f(\theta) \sin n\theta \ d\theta \ , \ \text{for} \ \ n \ \text{integer} \qquad (10b)$$

where,

$$f(\theta) = -\frac{1}{2} \ln\left\{ \frac{(1 - 2a \cos\theta + a^2)}{(1 - a)^2} \right\} + \frac{\theta}{\pi} \ln\left\{ \frac{1 + a}{1 - a} \right\} \qquad (10c)$$

IKEGAMI and MURATA were then in a position to produce theoretical performance characteristics, by moving the vortex in a radial sense. The flow rate through the impeller was expressed

$$Q = \psi_{\theta = 0} - \psi_{\theta = \pi}$$

and in dimensionless terms

$$\Phi = \frac{Q}{2r_2 U_2} = \left(\frac{r_1}{r_2} \right)^2 \ln\left\{ \frac{1 + a}{1 - a} \right\} \qquad (11)$$

per unit length of rotor.

The cross flow impeller does not give uniform energy transfer to each streamline and so the total pressure rise had to be expressed as a mean value of energy transfer to each streamline passing through the machine. The total pressure rise for an arbitrary streamline was given by

$$\frac{P_t}{\gamma} = \frac{U_2}{g} \left(C_{2D\theta} + C_{2S\theta} \right) \tag{12}$$

where $\gamma = \rho g$

and hence the mean value became

$$\tilde{P}_t = \frac{1}{Q} \int_0^{\pi} P_t \, C_{2Dr} \, r_2 \, d\theta \tag{13}$$

P_t was eliminated between eqns. (12) and (13). The inlet absolute velocity, $C_{2S\theta}$, was determined from the differential of eqn. (10) and the outlet absolute velocity C_{2Dr} was found from the outlet velocity triangle together with the equation of continuity. The total pressure coefficient defined by

$$\Psi = \frac{\tilde{P}_t}{\frac{1}{2}\rho U_2^2}$$

was then expressed in full

$$\Psi = f\left\{ a, \frac{r_1}{r_2}, \beta_2 \right\}$$

$$= \frac{2a}{\ln\left\{\frac{1+a}{1-a}\right\}} \cdot \int_0^{\pi} \left[1 + \left(\frac{r_1}{r_2}\right)^2 \left\{ \frac{2a \sin\theta}{1 + a^2 - 2a\cos\theta} \cot \beta_2 \right. \right.$$

$$\left. \left. - 2 \sum_n nk^n \sin n\theta \right\} \frac{\sin\theta}{1 + a^2 - 2a\cos\theta} \right] d\theta \tag{14}$$

IKEGAMI and MURATA cross plotted eqns. (11) and (14) to reveal the first theoretical performance characteristics as a function of the rotor geometry and the position of the vortex core. Figure 4.9 shows the effect of the blade angle β_2, indicating the difference between each graph increasing as capacity increases, with the smaller values of β_2 giving a correspondingly higher pressure rise. They demonstrated also the small influence of diameter ratio on the

$r_1/r_2 = 0.8$
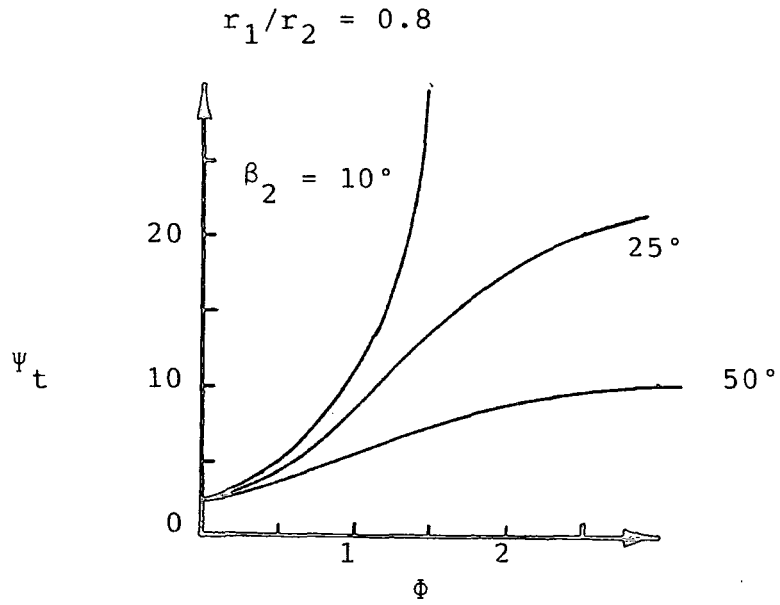
Figure 4.9 THEORETICAL PERFORMANCE CHARACTERISTICS (IKEGAMI
AND MURATA)
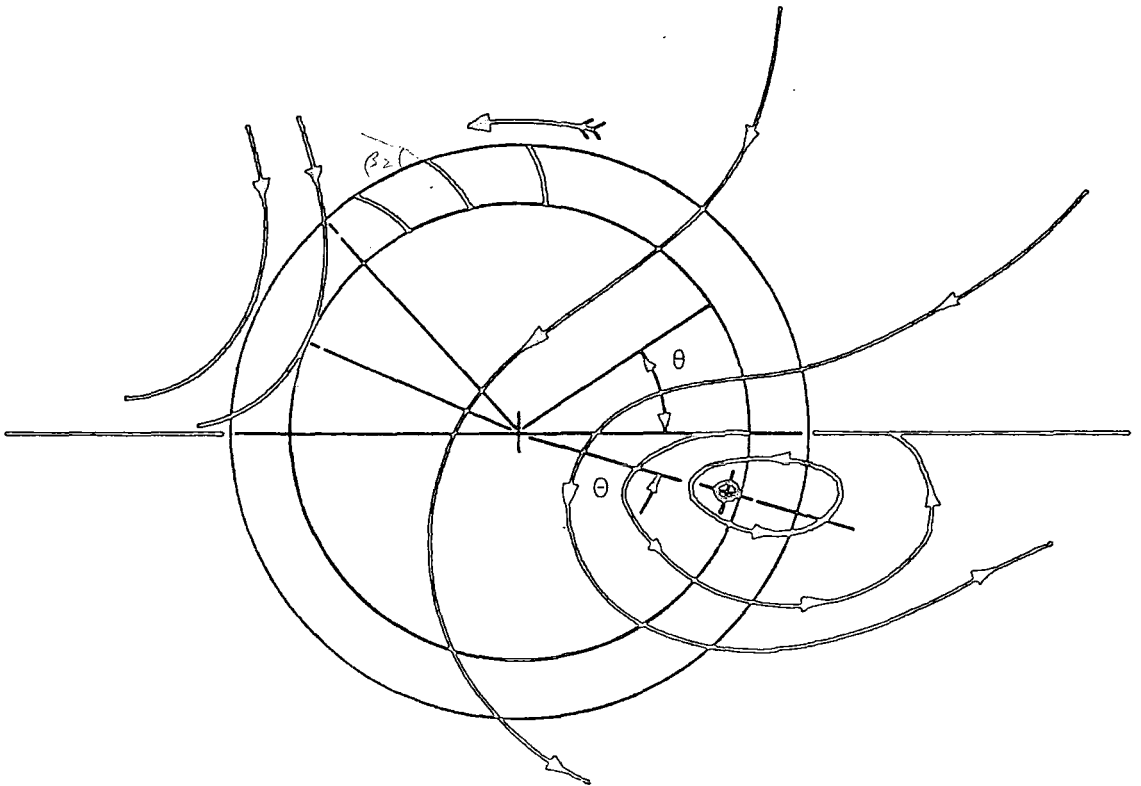
Figure 4.10 THEORETICAL FLOW PATTERN WITH PERIPHERAL
MOVEMENT OF VORTEX (IKEGAMI AND MURATA)

performance.

To allow the vortex total freedom within the impeller, they accounted for circumfrential as well as the previous radial motion. Inflow and outflow now occurred in both the suction and discharge regions as shown in Fig.4.10 , which implied that the flow in all regions differed from potential. They then argued that if the effective flow was not influenced by the other flows, performance characteristics could be calculated by changing the integration limits in eqn. (14) to cover the range of θ and $\Pi - \theta$ (θ being the peripheral displacement of the vortex core). It was then possible to evaluate a performance curve having previous knowledge of the locus of the vortex core over the flow range.

The final section of their paper considered the flow within the impeller rotational, i.e. with the right hand side of eqn. (4) non-zero. By introducing dimensionless terms for the stream function and the radius (asterisk terms), the flow regime was described by

$$\frac{d^2\psi^*}{dr^{*2}} + \frac{1}{r^*}\frac{d\psi^*}{dr^*} + \frac{1}{r^{*2}}\frac{d^2\psi^*}{d\theta^{*2}} = \left\{ \frac{1}{2\frac{d\psi^*}{d\theta}} \cdot \frac{d^2\psi^*}{dr^* \, d\theta} \right\}_{r^* = 1}$$

$$\equiv \sigma^*\,(r^*,\ \theta) \qquad\qquad (15)$$

and substitution of eqns. (7) and (10) yielded

$$\sigma^*\,(r^*,\ \theta) = \frac{1 + a^2 - 2a\,\cos\theta}{2a\,\sin\theta}\ \sum_n n^2\,k'_n\,\cos n\theta \qquad (16)$$

After finding convergence problems with eqn. (16), due to the n^2 term, IKEGAMI and MURATA found it possible to evaluate σ^* graphically, by using the distribution of

absolute velocities in the suction region. As only radial

vortex motion was being considered, the flow pattern was

symmetrical about the horizontal and so it was convenient to

transform the semi-circular region into a simpler rect-

angular region by the transformation function

$$\zeta = \ln r \qquad\qquad \eta = \theta$$

which applied to eqn (15) gave the elliptic partial differ-

ential equation

$$\frac{d^2\psi}{d\zeta^2} + \frac{d^2\psi}{d\eta^2} = e^{2\zeta}\,\sigma* \qquad\qquad (17)$$

Equation (17) was solved by direct application of the

relaxation method, once singularities had been removed,

which proved to be a non-trivial task. The solution to

eqn (17) indicated a more complex flow but as the magni-

tude of the values to be added to the purely potential

solution were relatively small, the total flow approximated

to the purely potential solution.

IREGAMI and MURATA concluded;

(i) the blade angle β_2 gave a remarkable influence on

the performance characteristics, while simple analyses

based on velocity diagrams, produced contrary results,

(ii) peripheral displacement of the vortex gave higher

pressure for small capacity than radial displacement,

(iii) inlet guide vanes designed suitably for a 'shockless'

inflow will bring desirable results and

(iv) since the effect of additional rotational flow is

small, the flow inside the impeller may be treated as

purely potential.

4.5.1 Problems with the Theory of IKEGAMI and MURATA

The paper of IKEGAMI and MURATA is the only publication devoted to a purely theoretical treatment of the cross flow fan. Apart from their own studies, it was likely that they drew experience from the work of many experimenters, notably BRUNO ECK (Ref.10). Unlike other fixed flow analyses, particularly COESTER'S, they were able to present a flow model which included a simple casing and allowed the vortex total mobility within the impeller. Although the mathematical analysis presented for radial vortex motion is correct and in order, errors have been found when computing the performance characteristics. Fig.4.9, taken from their paper, indicates the tendency for the graphs to plateau at high flow rates, especially for large values of β_2. The author found that the curves rose continuously for all values of β_2. The discrepancy arose over the calculation of the constant K'_n. For the calculation of eqn (14), numerical techniques were called for and therefore great care was required in ensuring complete convergence of equation elements. The author improved the computation by using up to 100 strips for the quadrature and included the effect of 25 harmonics for summations. This extension was observed to be most important when peripheral vortex motion was considered.

In section 4.5, the possibility of the vortex moving in a peripheral sense was examined by IKEGAMI and MURATA. It appears that the flow arrangement for the interior consisted of a pair of vortices (as before) but there is

some confusion over the position of the outside vortex; whether on the linear casing at $\theta = 0$ or on the same radial line as the main vortex. Their flow diagram, shown in Fig.4.10 seemed to indicate the former as the internal streamlines were no longer circular. However, eqn (14) integrated between Θ and $(\pi - \epsilon)$, seems to suggest the latter. Their calculation of the flow rate between θ and $(\pi - \Theta)$ was in order, as the $\theta = 0$ line had been rotated clockwise by Θ. However, their evaluation of the total pressure rise is in dispute as the values k' and k'_n are altered by the rotation of the internal flow field. In other words, what ever alteration was made to the flow field within the impeller, should have manifested itself as a change in k' and k'_n, which in turn should have produced a corresponding effect on the suction region. To be precise, the expression for stream function inside the impeller is given by

$$\psi = \frac{-r_1 u_1}{2} \ln\left\{ (r^2 + a^2 r_1^2 + 2arr_1 \cos(\theta + \Theta))(r^2 + \frac{r_1^2}{a^2} + \frac{2rr_1}{a} \cos(\theta + \Theta)) \right\} + \text{constant} \quad (18)$$

maintaining the same co-ordinate system as originally specified. This then gives

$$f(\theta) = \frac{1}{2}\ln\left\{ \frac{1 + a^2 - 2a \cos\theta}{1 + a^2 - 2a \cos(\theta + \Theta)} \right\} - \frac{\theta}{2\pi} \ln\left\{ \frac{1 + a^2 - 2a \cos\theta}{1 + a^2 + 2a \cos\theta} \right\} \quad (19)$$

from which eqn (10b) yields k'_n. The author used a formulation based on the above eqns (18) and (19) and integration between the limits of 0 to $(\pi - 2\Theta)$ gave results similar to those published by IKEGAMI and MURATA. Figure 4.11

133
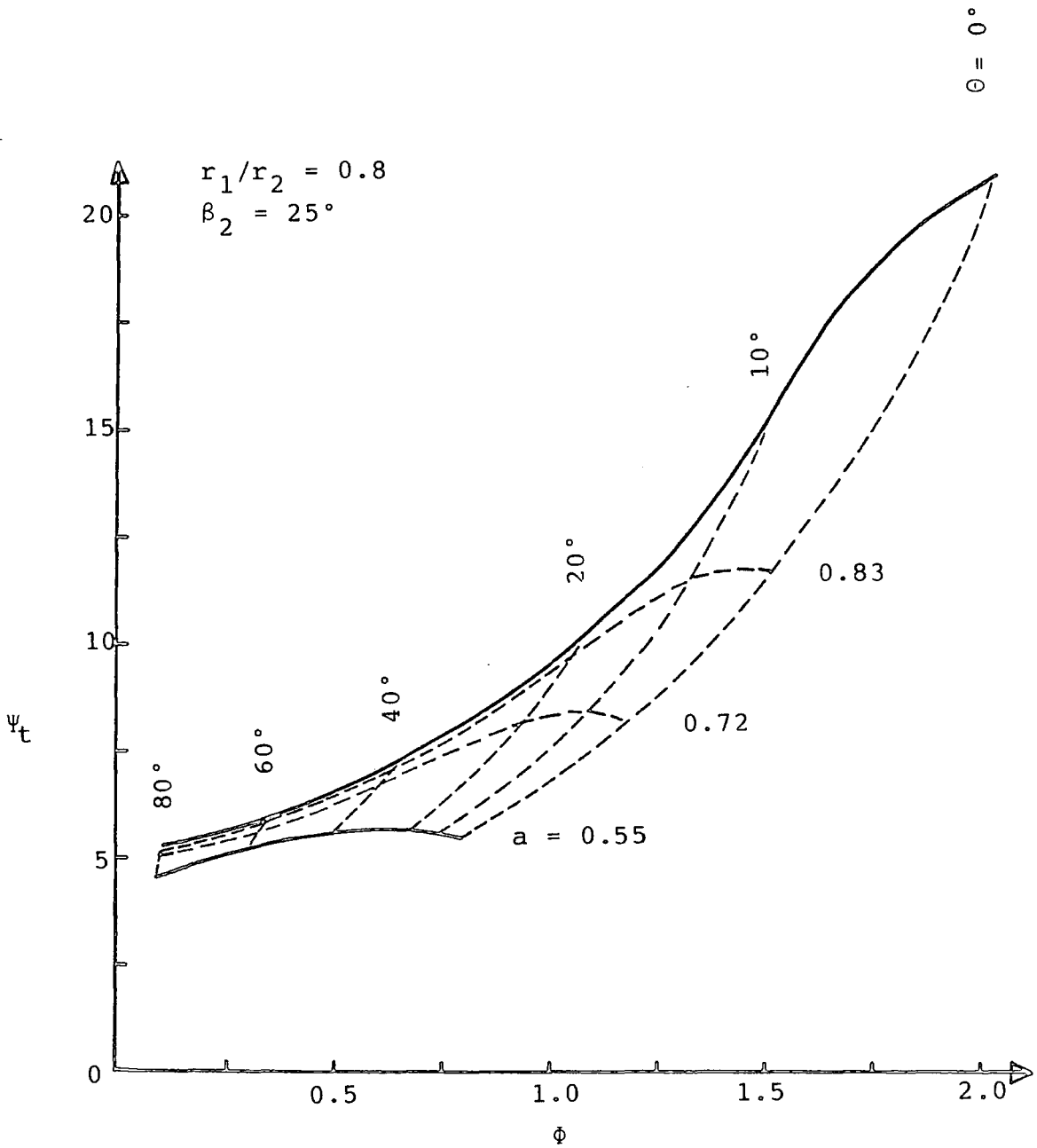
Figure 4.11   THEORETICAL PERFORMANCE

corrects their computations and compared with their study

is seen to be dissimilar for a = 0.92 with k_n' being the

responsible term, as previously discussed. At low capa-

cities, the form of the characteristic is almost inde-

pendent of the radial vortex position. Above $\phi = 1.0$,

higher pressure may be achieved by radial motion and in

some cases a fall in pressure is apparent for peripheral

motion. Figures 4.12 and 4.13 show the effect of the diameter

ratio.. For $r_1/r_2 = 0.7$ (Fig.4.12), a small performance net

is evident but it is interesting that for $r_1/r_2 = 0.9$ the

form of the characteristic is virtually independent of

the radial vortex position for flow rates up to $\phi = 1.0$.

Figures 4.14 and 4.15 display the effect of the outer blade

angle β_2. Figure 4.14 shows that for large forward curva-

ture, high values of pressure can be expected, however,

with less curvature, Fig.4.15 indicates a considerably lower

pressure rise with a virtually constant value of Ψ at low

flow rates.

Overall, the diameter ratio had a relatively small

effect on the slope of the characteristic but its chief

effect seems to be on the value of total pressure at zero

flow, $\Psi_{\phi=0}$, where higher values of r_1/r_2 are seen to

produce higher total pressure at zero flow. Larger chara-

cteristic slopes were evident with larger forward curva-

ture of the rotor blades with a corresponding increase in

$\Psi_{\phi=0}$.

As previously stated, Fig.4.10 appeared to suggest that

the vortex outside the rotor lay on the radial line $\theta = 0$,

producing non-circular streamlines within the rotor. The
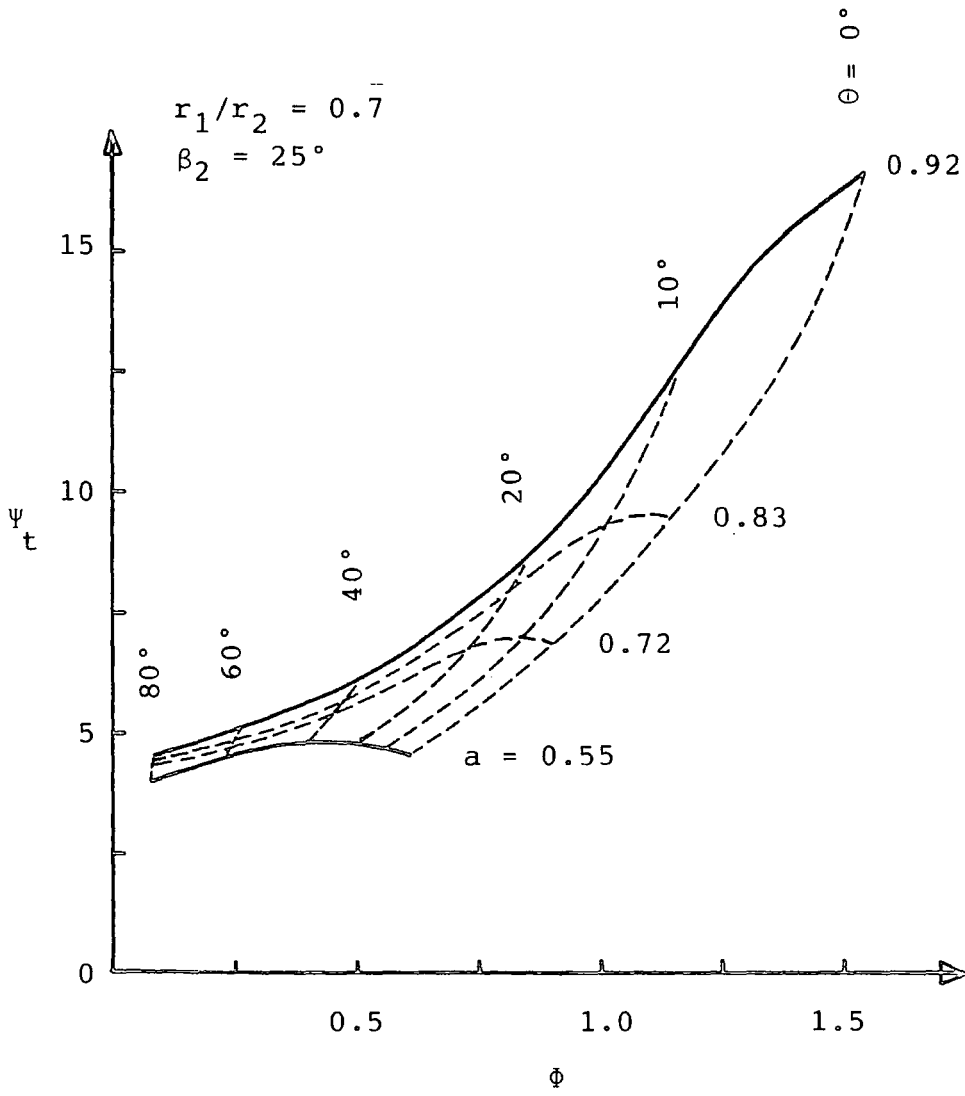
Figure 4.12   THEORETICAL PERFORMANCE
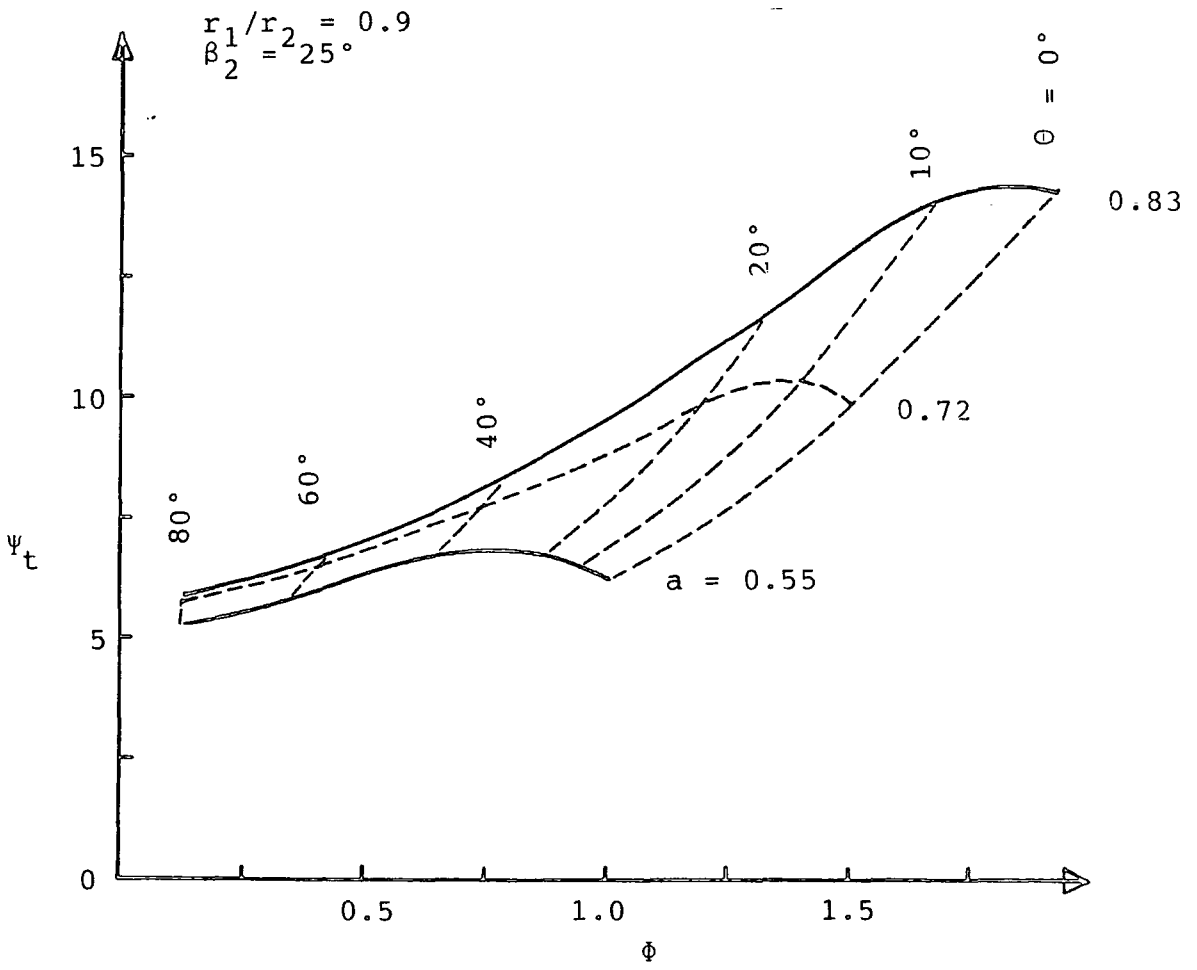
Figure 4.13   THEORETICAL PERFORMANCE
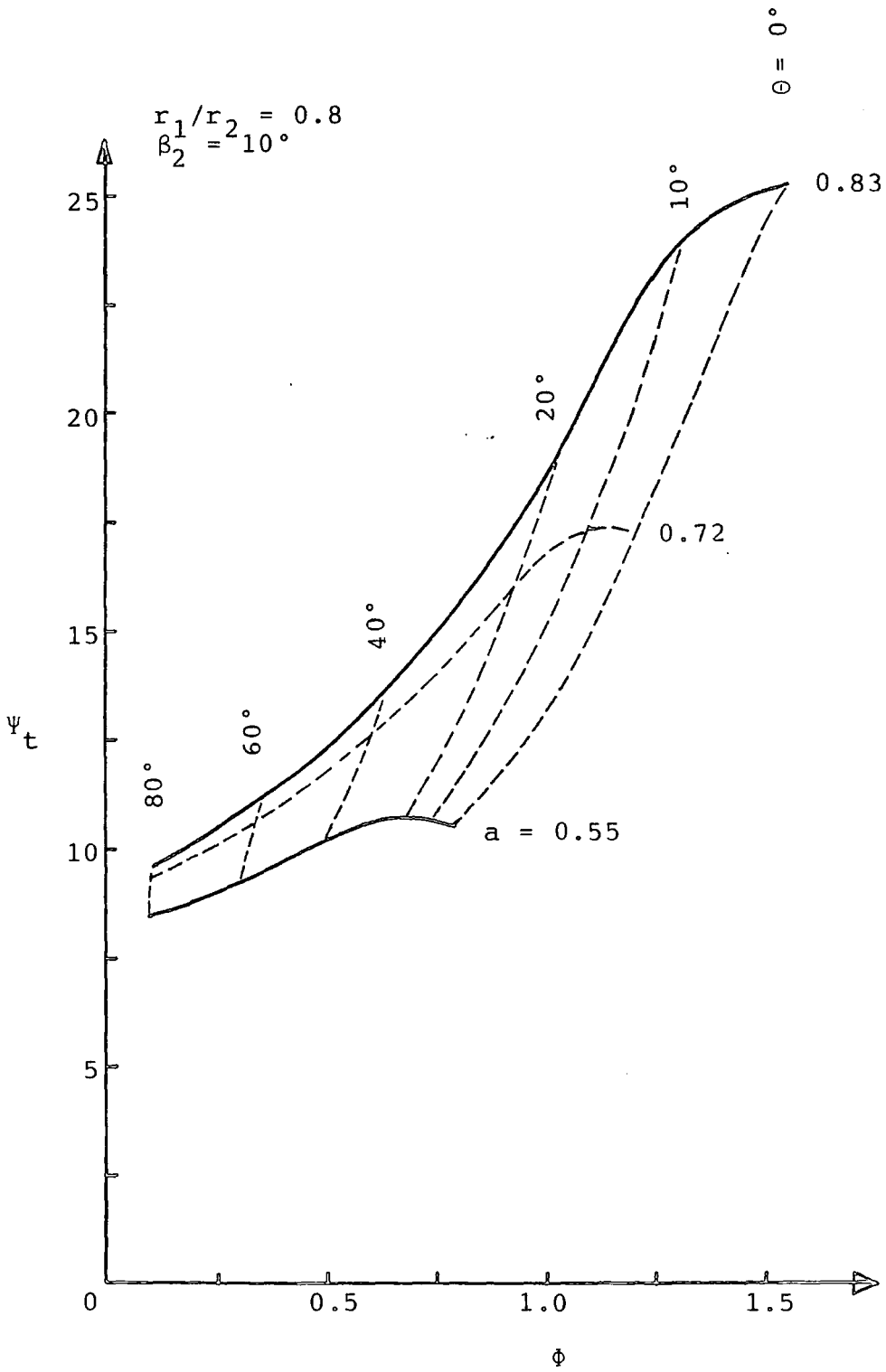
Figure 4.14 THEORETICAL PERFORMANCE
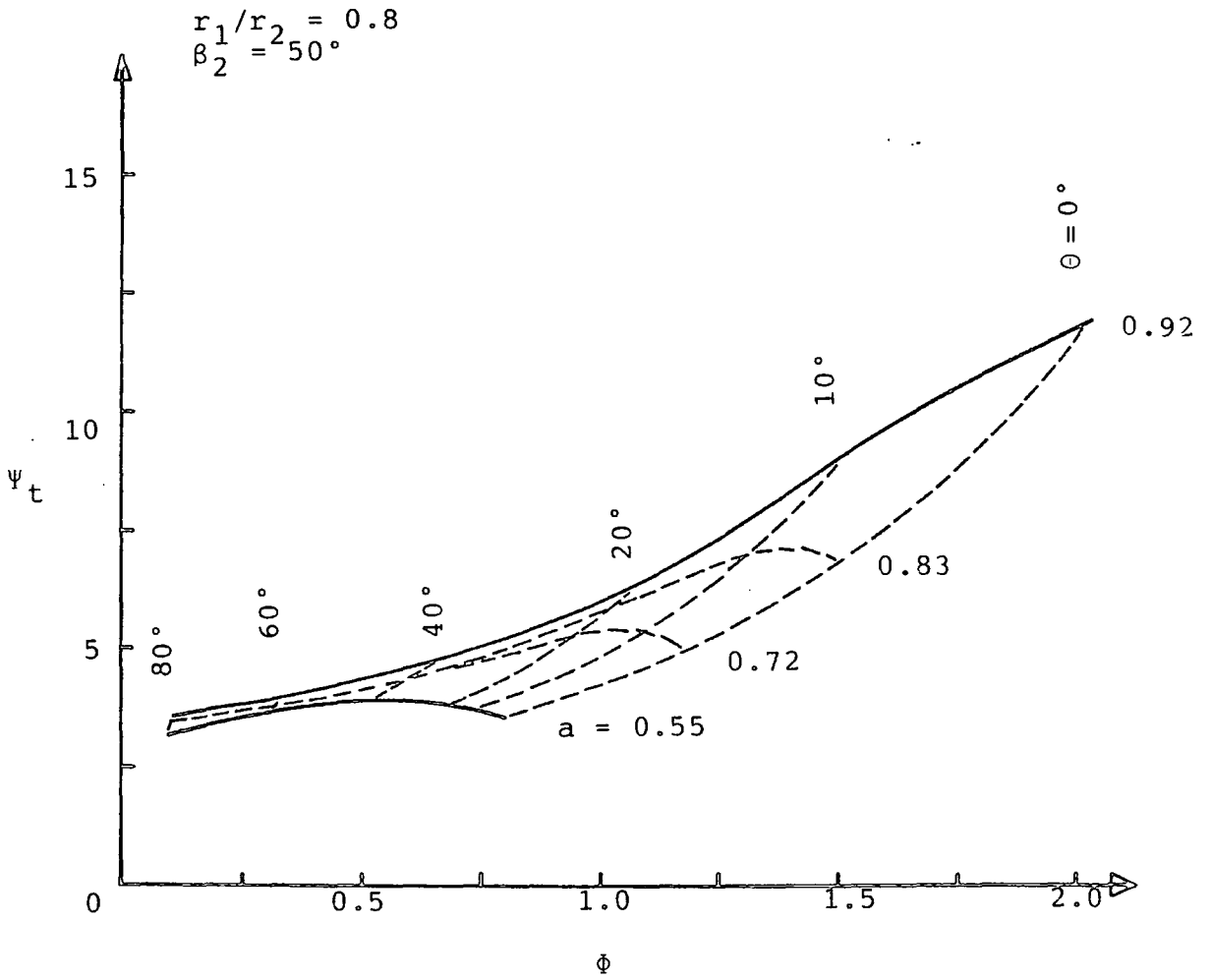
Figure 4.15   THEORETICAL PERFORMANCE

formula for the stream function within the rotor would then become

$$\psi = -\frac{r_1 u_1}{2} \ln \left\{ (r^2 + a^2 r_1^2 - 2arr_1 \cos(\theta + \Theta))(r^2 + \frac{r_1^2}{a^2} - \frac{2rr_1}{a} \cos\theta) \right\} + \text{constant} \quad (21)$$

A similar procedure was carried out as before. Unlike the vortices on the same radial line, the dividing streamline about the rear wall appeared radially opposite the vortex core. A superior velocity distribution was found around the rotor on the suction side. Figure 4.16 may be directly compared with Fig. 4.14 which shows that the lower limit for the flow rate has been raised from 0.2 to 0.5 and at low capacity the radial motion of the vortex gives higher pressure than peripheral motion. The effect of the blade angle β_2 is shown by comparing Figs. 4.16 and 4.17 where the dominance of this parameter is still evident, predicting results higher than those based on Euler triangle analyses.

4.5.2 A Parameter for Blade Geometry

To include a parameter for the number of blades and the thickness to chord ratio of the individual blades, a factor was introduced. Due to the geometry of the rotor, the flow restriction is more on the inner periphery than the outer. Thus, a factor for each was defined;

$$b_1 = \frac{2\pi r_1 - Nt}{2\pi r_1} \quad (22)$$
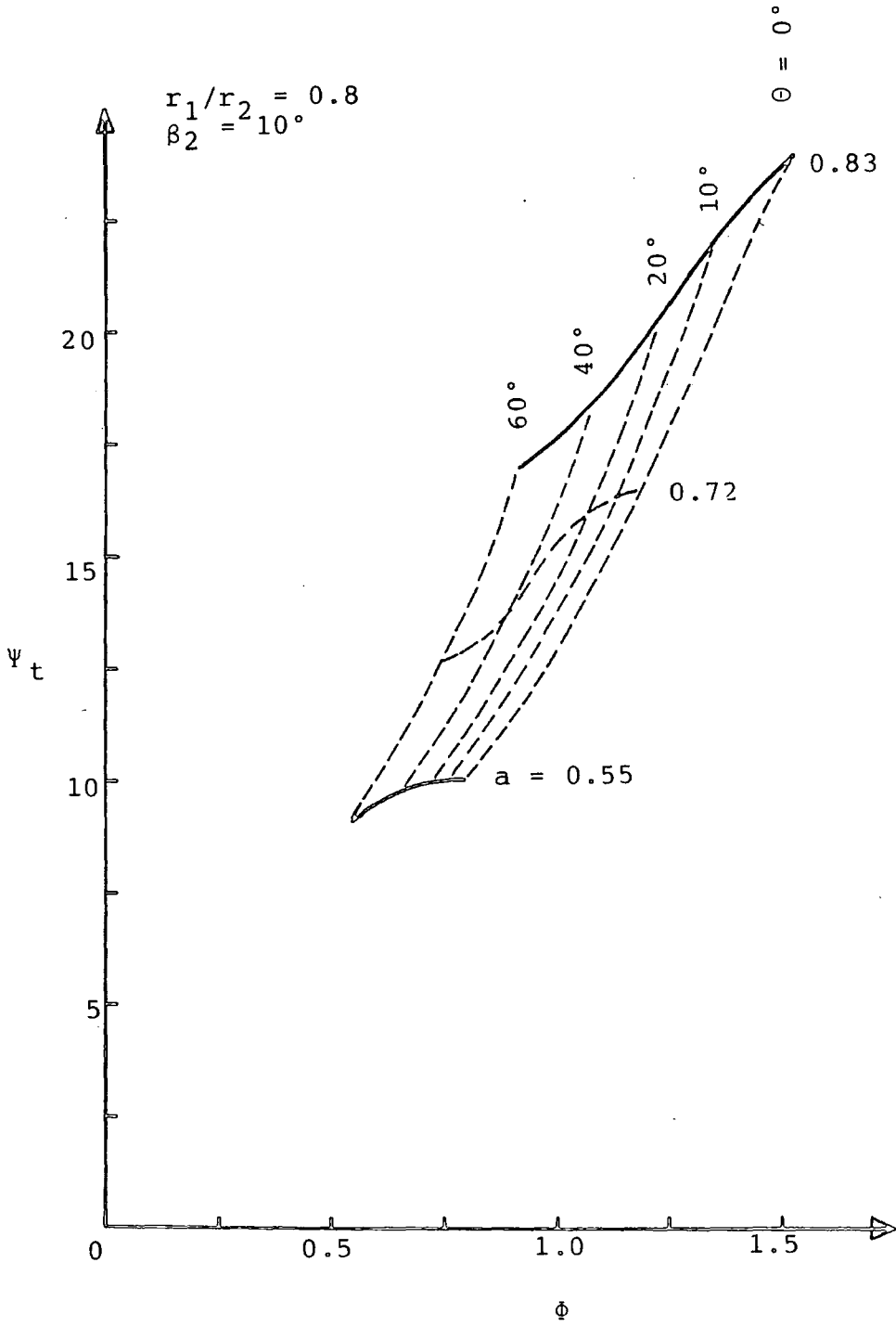
Figure 4.16 THEORETICAL PERFORMANCE
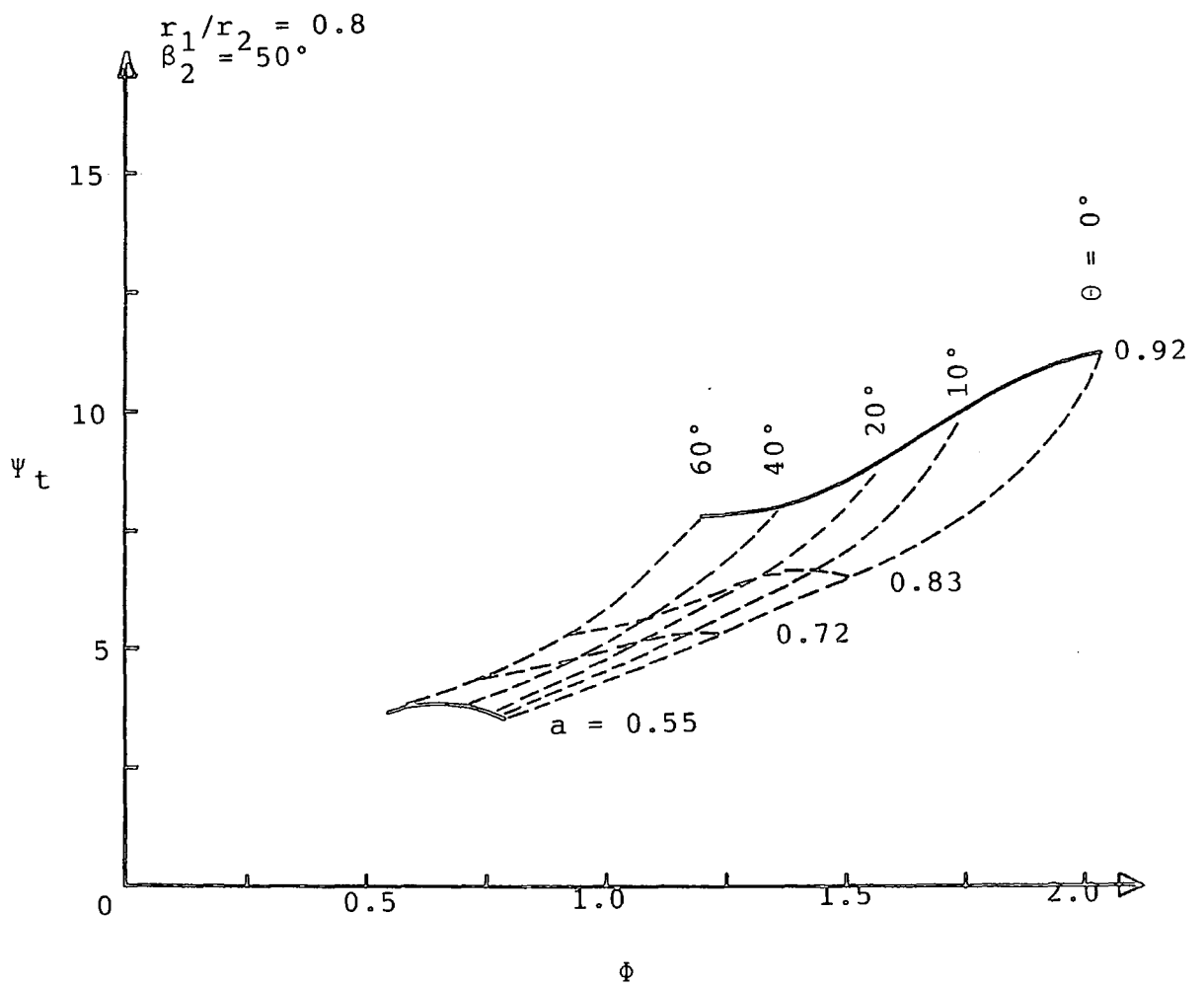
Figure 4.17   THEORETICAL PERFORMANCE

for the inner periphery and

$$b_2 = \frac{2\pi r_2 - Nt}{2\pi r_2} \tag{23}$$

for the outer periphery where;

N is the blade number,

t is the blade thickness

and r_1 and r_2 are the inner and outer radii respectively.

The equation of continuity was written

$$\left\{ \frac{2\pi r_2}{N} - t \right\} C_{2r} = \left\{ \frac{2\pi r_1}{N} - t \right\} C_{1r} \tag{24}$$

and rearranging eqns. (22), (23) and (24) gave

$$b_2\, r_2\, C_{2r} = b_1\, r_1\, C_{1r} \tag{25}$$

by definition

$$C_{2r} = \left\{ \frac{1}{r}\, \frac{d\psi}{d\theta} \right\}_{r=r_2} \quad \text{and} \quad C_{1r} = \left\{ \frac{1}{r}\, \frac{d\psi}{d\theta} \right\}_{r = r_1} \tag{26}$$

and substituting in eqn (25) gave

$$b_1 \left(\frac{d\psi}{d\theta} \right)_{r=r_1} = b_2 \left(\frac{d\psi}{d\theta} \right)_{r=r_2} \tag{27}$$

From which integration yielded

$$\frac{b_1}{b_2}\, \psi_{r=r_1} = \psi_{r=r_2} + \text{constant} \tag{28}$$

Finally, let $B = {}^{b}1/b_2$ and redefine the blade thickness as a thickness to chord ratio percentage, T%.

$$B = \frac{200\pi + NT\,(1 - \frac{r_2}{r_1})}{200\pi + NT\,(\frac{r_1}{r_2} - 1)} \tag{30}$$

The computation was repeated with eqn. (10a) replaced by eqn. (28) for a variety of blade profiles and blade number. Figure 4.18 shows that the more slender profiles are associated
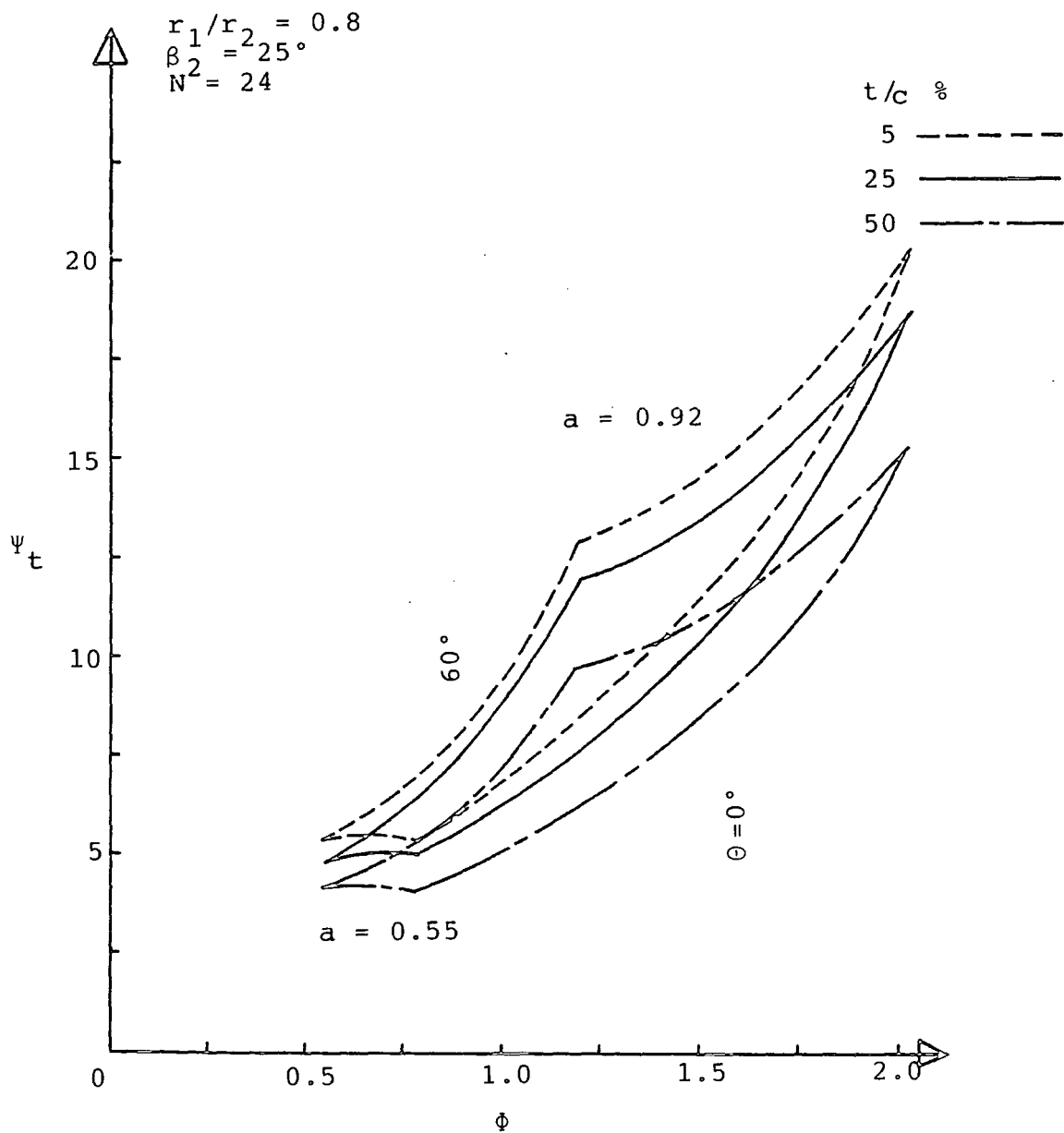
Figure 4.18 EFFECT OF BLADE PROFILE ON THEORETICAL
PERFORMANCE

with the higher pressure rises. Figure 4.19 indicates that
the blade number had little effect on the overall perfor-
mance with fewer blades giving a marginally better result.
It is well known that forward curved rotors require more
blades than their backward curve counterparts, due to an
effect known as whirl slip. Interestingly enough, Fig 4.19
does not share the same view, as an increased blade number
would also increase the associated friction loss. However,
the theory could not possibly detect whirl slip, as it
assumes perfect guidance of the fluid through the blade
passages.

4.5.3   The Reflex Curvature of the Streamlines

The flow visualisation and aerodynamic studies
showed that the curvature of the streamlines within the
rotor tended to increase more rapidly than expected across
a radial line through the vortex core and in some cases
a reversed curvature occurred towards the rear wall leading
edge. To model this reversed curvature, a source and
sink were positioned opposite the vortex core, as shown
in Fig 4.20, and just displaced from the inner periphery to
avoid singularities when introducing the boundary condition.
The stream function due to the source sink is by defi-
nition

$$\psi = \frac{m}{2\pi} (\theta_1 - \theta_2) \qquad (31)$$

and from the geometry in Fig. 4.20

$$\theta_1 - \theta_2 = \text{Arcos} \left\{ \frac{d_1^2 + d_2^2 - 4b^2}{2d_1 d_2} \right\} \qquad (32)$$
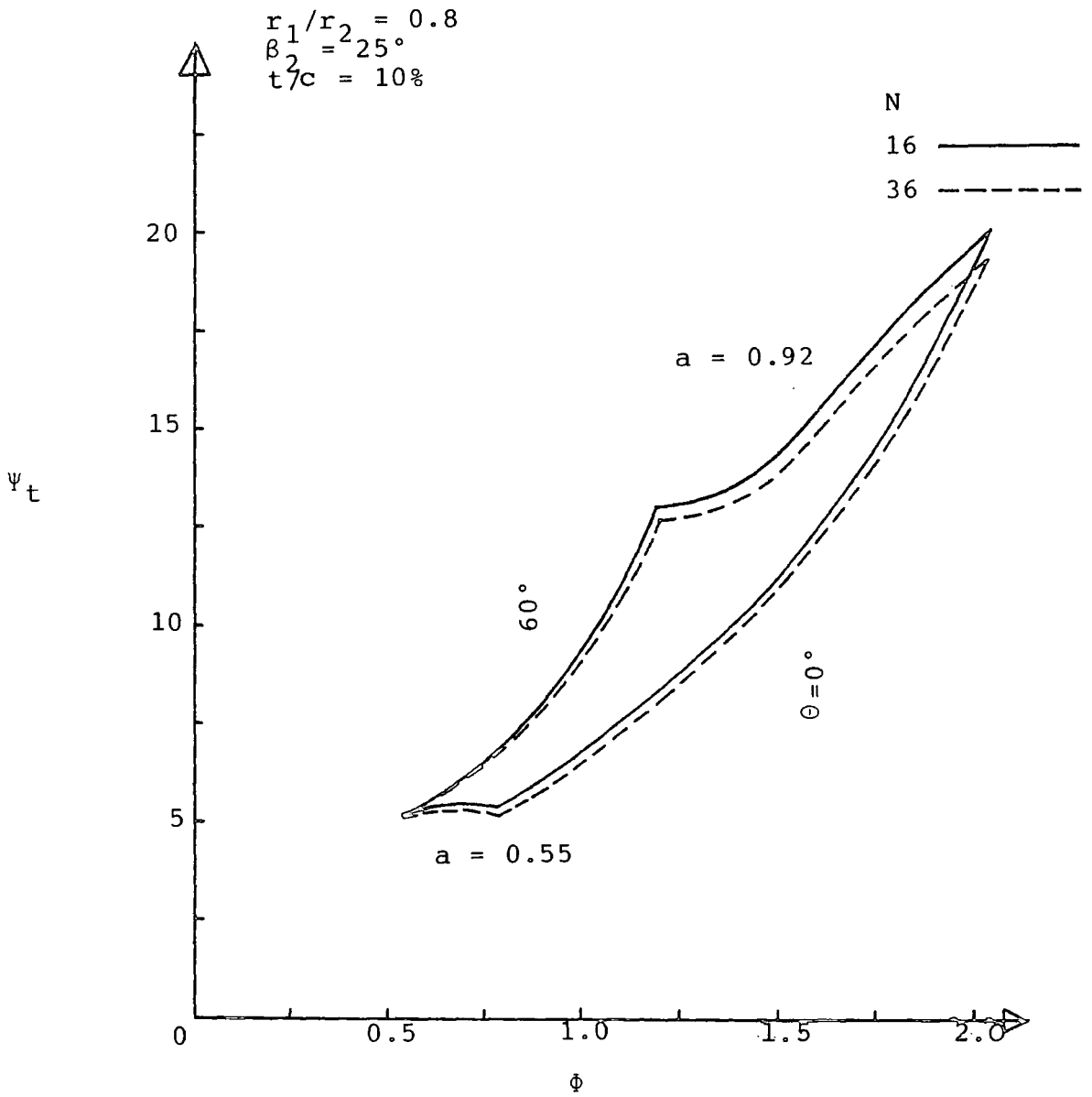
Figure 4.19   EFFECT OF BLADE NUMBER ON THEORETICAL
              PERFORMANCE
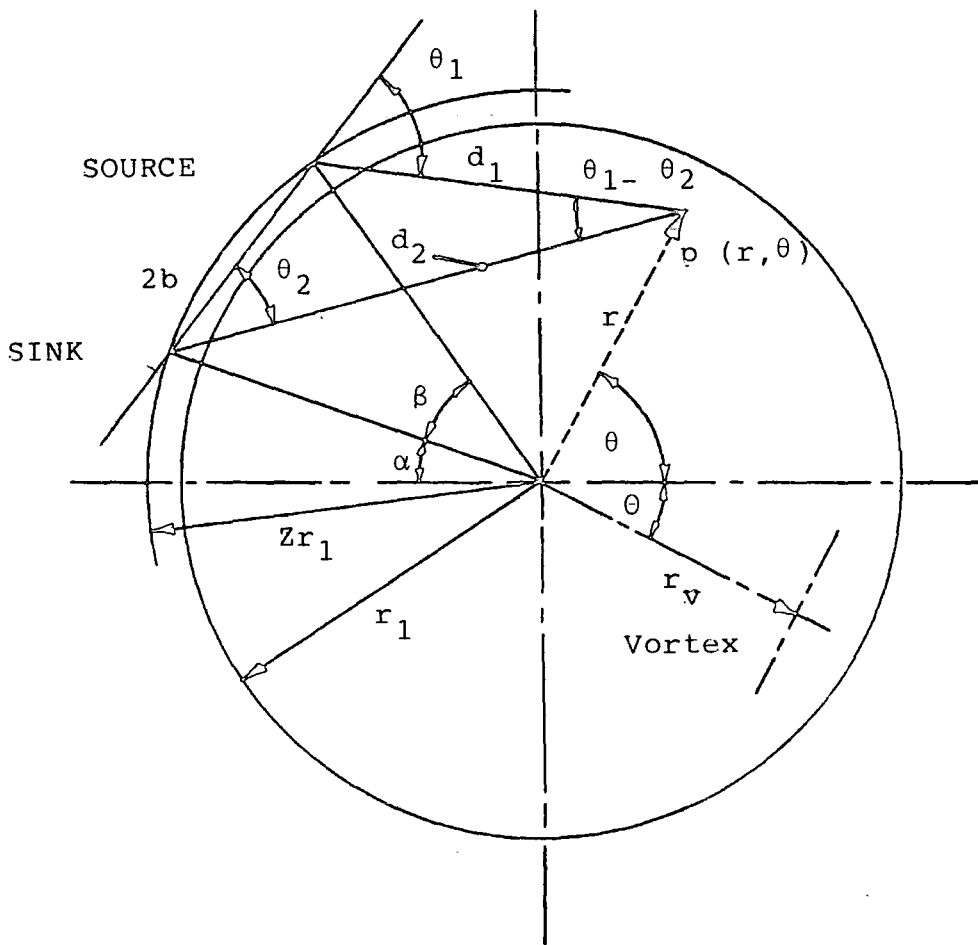
Figure 4.20 ADDED SOURCE AND SINK TO MODIFY THEORETICAL
INTERNAL FLOW

147

giving

$$\psi = \frac{m}{2\pi} \text{Arcos} \left\{ \frac{r^2 + zrr_1\{\cos(\theta+\alpha) + \cos(\theta+\alpha+\beta)\} + (zr_1)^2\cos\beta}{\left[\{r^2 + (zr_1)^2 + 2zrr_1 \cos(\theta+\alpha+\beta)\}\{r^2 + (zr_1)^2 + 2zrr_1 \cos(\theta+\alpha)\}\right]} \right\}$$

(33)

The new expression for the stream function for the internal region was the summation of eqn (33) with eqn (6). The performance was then evaluated as described earlier. Fig 4.21 indicates the existence of a streamline which passed through the rotor from a position θ_x on the periphery. The calculation of the flow rate was unaffected by this as $\psi_{\theta=\theta_x} = \psi_{\theta=\pi}$, but the arc between θ_x and π did not contribute towards the throughflow or the pressure rise. The program was therefore designed to calculate the position of θ_x and provide the upper integration limit for the modified version of eqn (14).

For all flow conditions, the boundary condition given in eqn (5) was strictly observed. A subroutine was provided with the strength and position of all flow inducing agents, which satisfied eqn (5) by allowing the strength of the vortices to alter freely, which in turn depended on the co-ordinates of the main vortex. Initially, the source was positioned directly opposite the vortex core and the sink positioned on the rear wall leading edge at $\theta = \pi$, i.e $\alpha = 0$ and $\beta = \theta$, as shown in Fig.4.20 The source and sink were of unit strength and located on a circle slightly displaced from the inner periphery. This was to avoid singularities within the flow field, as the velocity at

148

the centre of a source or sink is infinite (zr_1 may be considered as the rear wall clearance).

Figure 4.22 shows the variation in the vortex strength as a function of position within the rotor, which is seen to change considerably for peripheral movement, although not for radial movement, apart from the region close to the inner periphery of the blade row. The resulting performance diagram was not significantly different to that of Fig.4.11. This change in the vortex strength substantiates experimental investigations carried out by the author and mentioned in Chapter 2.

A description of the cross flow fan performance, resulting from changes in the vortex strength, is called for which will require a better modelling of the strengths and locations of the source and sink. An example of the effect of the source and sink on the overall flow field is shown in Fig.4.23 The flow chart for the theoretical performance computer program is detailed in Fig.4.24

4.5.4 Losses within Cross flow fans

The losses occuring within cross flow fans may be divided into two categories;
(i) shock losses resulting from the inlet relative flow angle not being equivalent to the outer blade angle and
(ii) losses within the vortex.
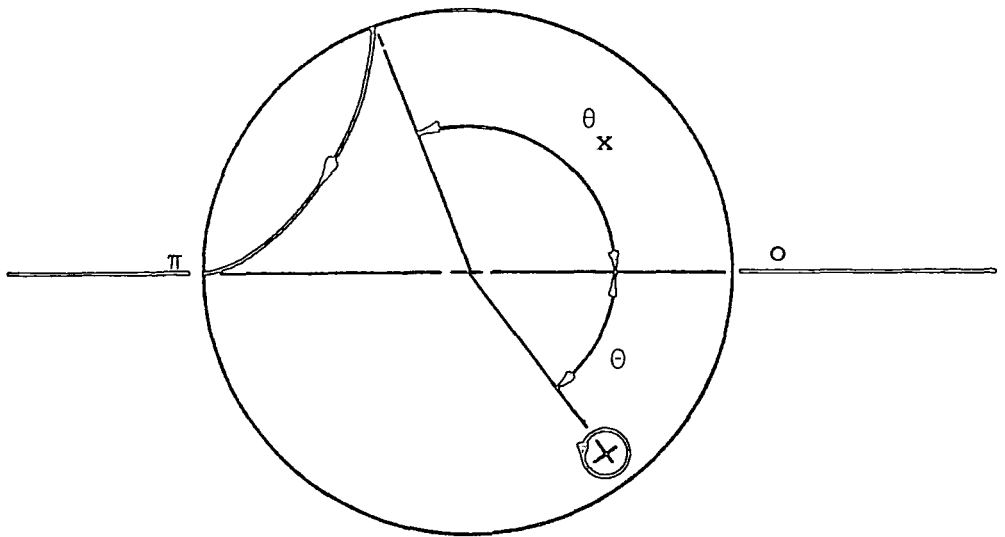
Figure 4.21   DIVIDING STREAMLINE IN INTERNAL REGION
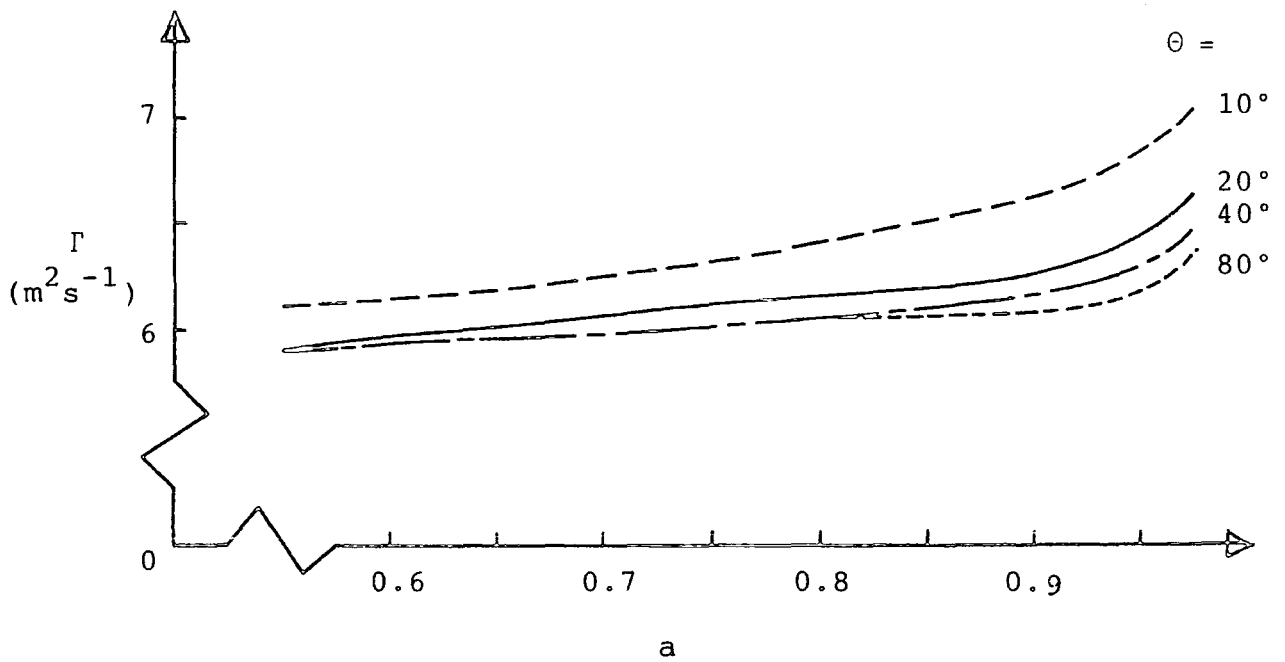
Figure 4.22   THEORETICAL VARIATION OF VORTEX STRENGTH
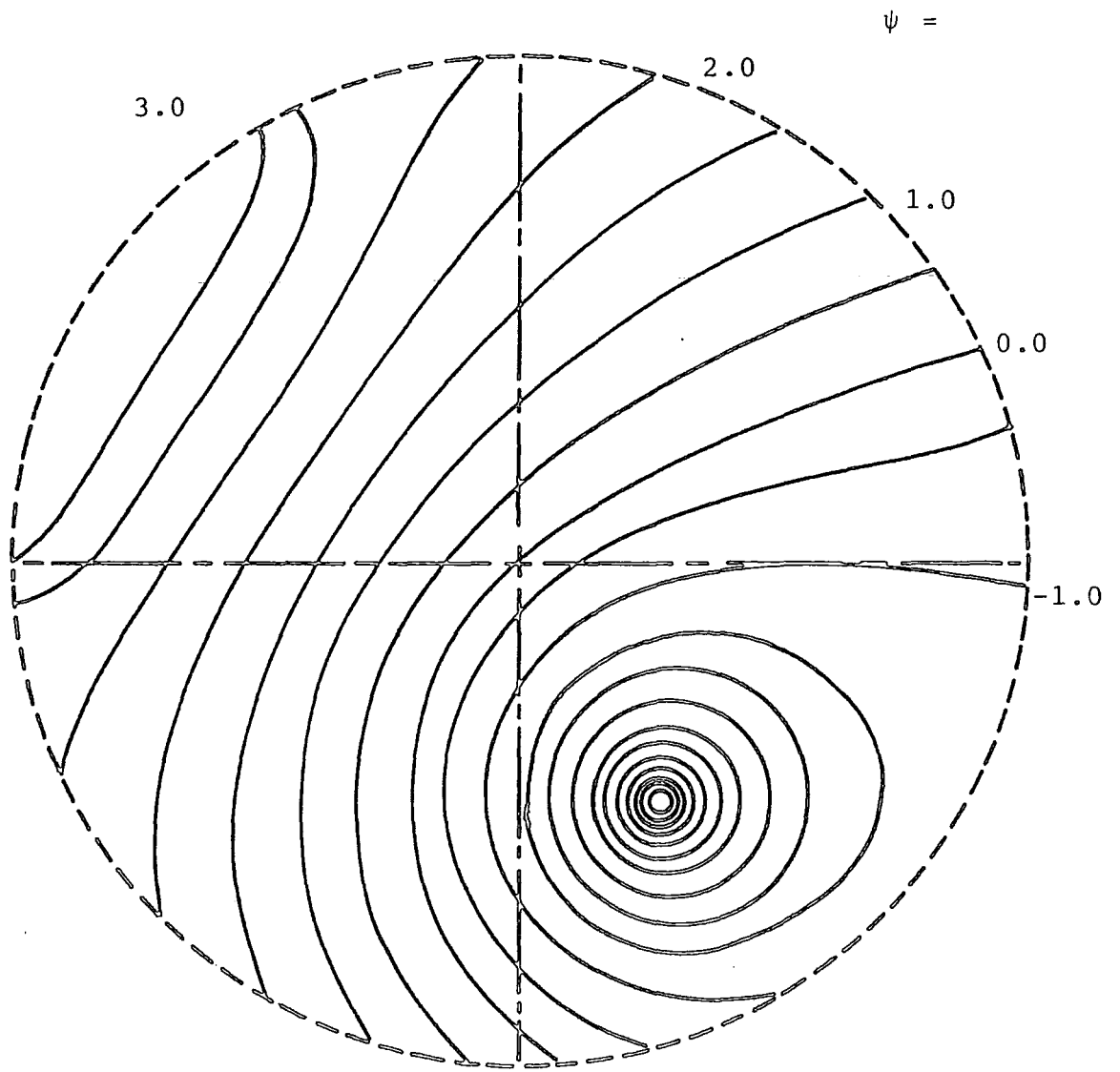
Figure 4.23   FLOW FIELD WITH MODIFICATIONS OF FIG. 4.20

151

Theoretical Performance Computer Flow Chart

START → Read Data
r_1/r_2, β_2, t/c, N, α, Z, m, Γ.

Evaluate β
$\beta = f\{\alpha, \theta\}$.

Calculate Blockage Factor, B.

Select first value of θ

Select first value of 'a'

CALL INNER to correct for boundary condition, u_1

Evaluate q_θ at $r = r_1$ due to source and sink + vortices.

Does q_θ (at $r = r_1$) = u_1?

NO → Increment Γ

YES → Return value of Γ to main prog.

Evaluate k'_n + check convergence

Evaluate Φ

Calculate θ_x, where $\psi_{\theta=\pi} = \psi_{\theta=\theta}$

Evaluate C_{2Dr}

Evaluate integrand of ψ integrating from O to θ_x

Write Φ, ψ, a, θ, Γ

Increment 'a'

Increment θ

End of θ Array → STOP → END

Fig. 4.24   152

4.5.4.1 Inlet 'shock' losses

The inlet shock losses were examined by using the expression for the stream function in the suction region, given by eqn (10). The peripheral component of the absolute velocity was then found to be

$$C_{2\theta} = \left\{-\frac{\delta\psi}{\delta r}\right\}_{r=r_2} = \frac{2r_1}{r_2} U_1 \sum_n nk_n' \sin n\theta \qquad (34)$$

and the corresponding radial component

$$C_{2r} = \left\{\frac{1}{r}\frac{\delta\psi}{\delta\theta}\right\}_{r=r_2} = \frac{2r_1}{r_2} U_1 (k' + \sum_n nk_n' \cos n\theta) \qquad (35)$$

Figure 4.25 shows the variation of the tangential and radial velocities around the outer periphery of the rotor, together with the deviation of the relative velocity from the blade angle. It is seen that the majority of shock losses occur near the vortex wall, where the radial velocities are highest. Clearly, the blades cannot always be presented at zero incidence to the relative flow and so, unless inlet guide vanes are used (designed using eqn (10)), shock losses will always be present, to an extent.

4.5.4.2 Viscous Losses within a Rankine Vortex

The second form of losses are those present within the vortex. These losses may be both viscous and inertial (as suggested by MOORE (Ref.16)). For the purpose of this analysis it was assumed that the vortex was unbounded, i.e. lying within an infinite expanse of fluid. The vortex was of a Rankine type, with the forced region described by
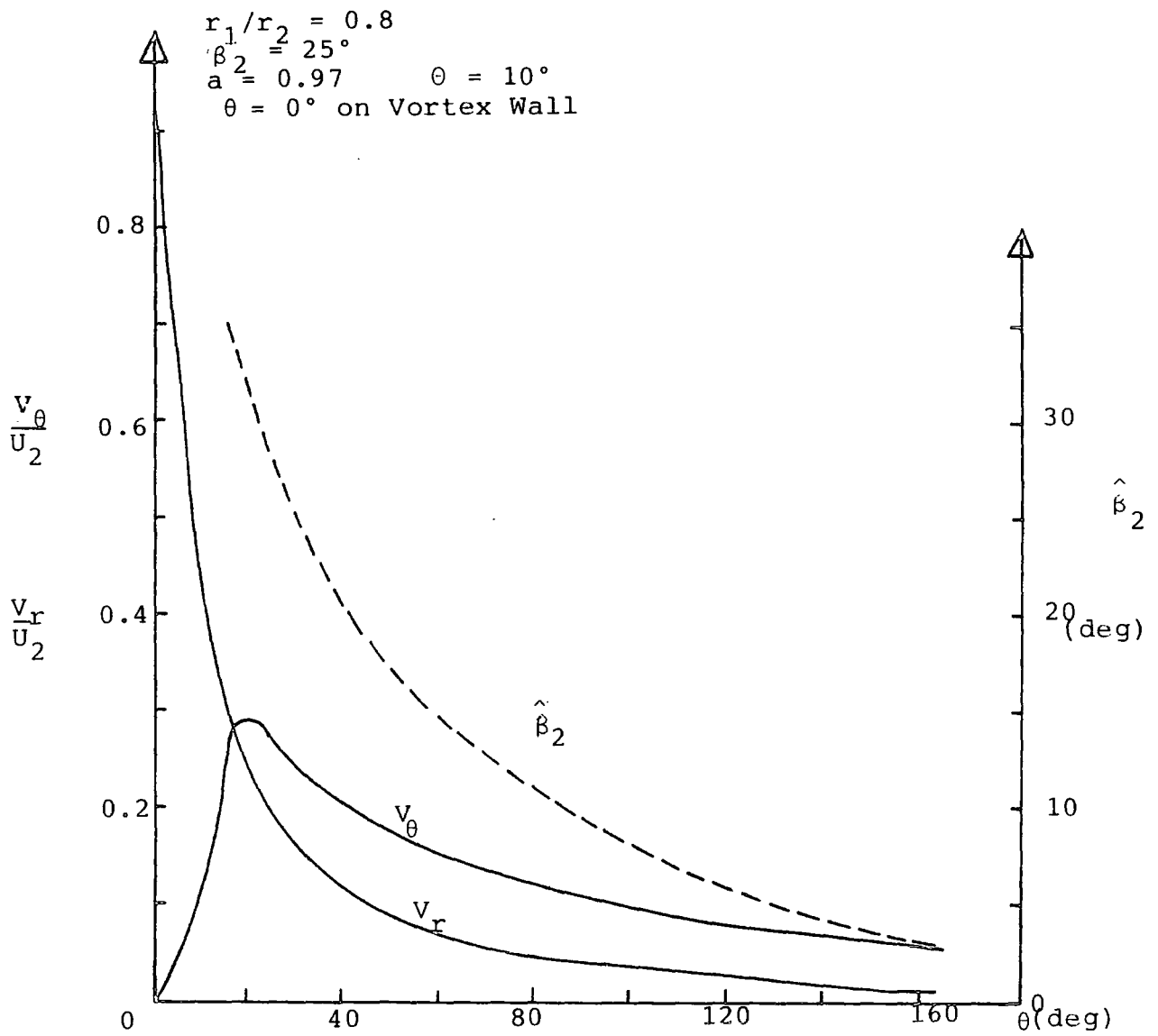
Figure 4.25   THEORETICAL VARIATION OF VELOCITY AND DEVIATION
IN THE SUCTION REGION

154

$$V_\theta = rw \qquad (36)(a)$$

and the surrounding free vortex given by

$$rV_\theta = \frac{\Gamma}{2\pi} \qquad (37)(a)$$

The theoretical velocity profile is shown in Fig.2.18 with an element of this flow in Fig.4.26 The power input to each face of the element was calculated as the vector sum of the pressure and shear stress terms.

For element face AB

$$P_{AB} = \left(P + \frac{dp}{dr}\frac{dr}{2}\right)\left(V_\theta + \frac{dV_\theta}{dr}\frac{dr}{2}\right)dr - \left(\tau + \frac{d\tau}{dr}\frac{dr}{2}\right)\left(V_r + \frac{dV_r}{dr}\frac{dr}{2}\right)dr \qquad (36)$$

and for face BC

$$P_{BC} = -\left(P + \frac{dp}{dr}dr + \frac{dp}{d\theta}\frac{d\theta}{2}\right)\left(V_r + \frac{dV_r}{dr}dr + \frac{dV_r}{d\theta}\frac{d\theta}{2}\right)(r + dr)d\theta$$

$$+ \left(\tau + \frac{d\tau}{dr}dr + \frac{d\tau}{d\theta}\frac{d\theta}{2}\right)\left(V_\theta + \frac{dV_\theta}{dr}dr + \frac{dV_\theta}{d\theta}\frac{d\theta}{2}\right)(r + dr)d\theta \qquad (37)$$

Similarly for face CD

$$P_{DC} = -\left(P + \frac{dp}{dr}\frac{dr}{2} + \frac{dp}{d\theta}d\theta\right)\left(V_\theta + \frac{dV_\theta}{dr}\frac{dr}{2} + \frac{dV_\theta}{d\theta}d\theta\right)dr$$

$$+ \left(\tau + \frac{d\tau}{dr}\frac{dr}{2} + \frac{d\tau}{d\theta}d\theta\right)\left(V_r + \frac{dV_r}{dr}\frac{dr}{2} + \frac{dV_r}{d\theta}d\theta\right)dr \qquad (38)$$

and finally for face DA

$$P_{DA} = \left(P + \frac{dp}{d\theta}\frac{d\theta}{2}\right)\left(V_r + \frac{dV_r}{d\theta}\frac{d\theta}{2}\right)r\,d\theta - \left(\tau + \frac{d\tau}{d\theta}\frac{d\theta}{2}\right)\left(V_\theta + \frac{dV_\theta}{d\theta}\frac{d\theta}{2}\right)r\,d\theta \qquad (39)$$

The total rate of energy dissipation within the element of fluid was found by adding eqns (36), (37), (38) and

$p + \dfrac{dp}{dr}\,dr + \dfrac{dp}{d\theta}\,\dfrac{d\theta}{2}$

$\tau + \dfrac{d\tau}{dr}\,dr + \dfrac{d\tau}{d\theta}\,\dfrac{d\theta}{2}$

$\tau + \dfrac{d\tau}{dr}\,\dfrac{dr}{2}$

$(r+dr)d\theta$

$\tau + \dfrac{d\tau}{dr}\,\dfrac{dr}{2} + \dfrac{d\tau}{d\theta}\,d\theta$

B

C

dr

$r\,d\theta$

A

D

$p + \dfrac{dp}{dr}\,\dfrac{dr}{2}$

$\tau + \dfrac{d\tau}{d\theta}\,\dfrac{d\theta}{2}$

$p + \dfrac{dp}{dr}\,\dfrac{dr}{2} + \dfrac{dp}{d\theta}\,d\theta$

$p + \dfrac{dp}{d\theta}\,\dfrac{d\theta}{2}$

$d\theta$
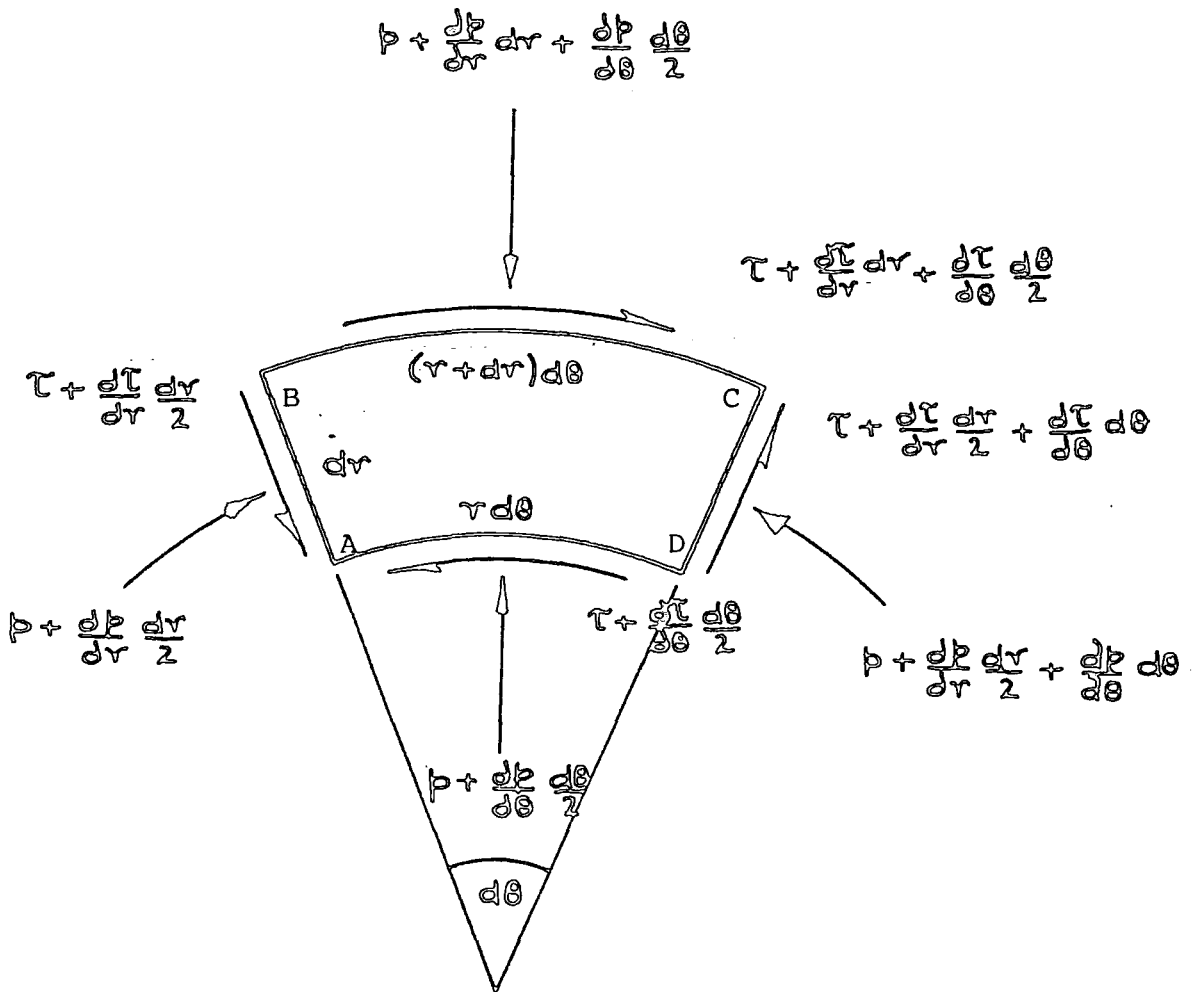
Figure 4.26   ELEMENT OF VORTEX FLOW

156

(39) and dividing by rdr dθ (unit volume)

$$\dot{E} = -\frac{p}{\gamma}\frac{dV_\theta}{d\theta} - \frac{V_\theta}{\gamma}\frac{dp}{d\theta} + \frac{\tau}{\gamma}\frac{dV_r}{d\theta} + \frac{V_r}{\gamma}\frac{d\tau}{d\theta} - \frac{pV_r}{\gamma} - p\frac{dV_r}{dr} - V_r\frac{dp}{dr} + \frac{\tau V_\theta}{\gamma} + \tau\frac{dV_\theta}{dr} + V_\theta\frac{d\tau}{dr}$$

$$= \frac{1}{\gamma}\left\{\frac{d}{d\theta}(\tau V_r) - \frac{d}{d\theta}(pV_\theta) + \tau V_\theta - pV_r\right\} - \frac{d}{dr}(pV_r) + \frac{d}{dr}(\tau V_\theta)$$

per unit volume. (40)

For a Rankine type vortex, continuity of v_θ must exist at the boundary. Equations (36)(a) and (37)(a) then gave

$$\omega = \frac{\Gamma}{2\pi a^2} \tag{41}$$

and hence for the forced vortex

$$V_\theta \text{ (forced)} = \frac{r\Gamma}{2\pi a^2} \tag{42}$$

The radial pressure variation in a free vortex is given from eqn (37)

$$\frac{dp}{dr} = \rho\left\{\frac{\Gamma}{2\pi}\right\}^2 \frac{1}{r^3} \tag{43}$$

and integrating yields

$$p \text{ (free)} = -\rho\left\{\frac{\Gamma}{2\pi}\right\}^2 \frac{1}{2r^2} + \text{constant} \tag{44}$$

Similarly, eqn (36) yielded the pressure variation across a forced vortex

$$\frac{dp}{dr} = \rho r\left\{\frac{\Gamma}{2\pi a^2}\right\}^2 \tag{45}$$

and integrating

$$p \text{ (forced)} = \rho \frac{r^2}{2} \left\{ \frac{\Gamma}{2\pi a^2} \right\}^2 + \text{constant} \qquad (46)$$

The expression for shear stress in polar co-ordinates

$$\tau = \mu r \frac{d}{dr} \left(\frac{v_\theta}{r} \right) \qquad (47)$$

produced for the free region

$$\frac{d}{dr}\left(\frac{v_\theta}{r} \right) = - \frac{\Gamma}{\pi r^3} \qquad (48)$$

and therefore

$$\tau \text{(free)} = - \frac{\mu \Gamma}{\pi r^2} \qquad (49)$$

As $v_\theta/r = \omega$, the shear stress terms vanished in the forced region. According to the initial assumptions, the stream-lines in both regions are concentric circles and as such the radial velocity and the peripheral pressure gradient is zero, i.e $v_r = 0$ and $dp/d\theta = 0$. Equation (40) then became

$$\overset{\circ}{E} = \frac{1}{r}\left(\tau v_\theta \right) + \frac{d}{dr}\left(\tau v_\theta \right) \text{ , per unit volume. } (50)$$

For the free vortex

$$\tau v_\theta = - \mu \frac{\Gamma^2}{2\pi^2 r^3} \qquad (51)$$

and hence

$$\overset{\circ}{E} \text{ (free)} = \frac{\mu \Gamma^2}{\pi^2 r^4} \qquad \text{, per unit volume} \qquad (52)$$

Again, the energy within the forced region was zero. An elemental annulus has volume $2\pi rdr$ and the total rate of energy dissipated was calculated from

$$\dot{E}_{TOTAL} = \int_{a}^{\infty} \frac{\mu\Gamma^2}{\pi^2} \frac{1}{r^4} 2\pi rdr$$

$$\doteq \frac{\mu\Gamma^2}{\pi a^2} \qquad (53)$$

and using eqn (37) gave

$$\dot{E}_{TOTAL} = \frac{4\mu\pi r^2 v_\theta^2}{a^2} \qquad (54)$$

Finally, values at the boundary between the free and forced regions were introduced,

$$v_\theta = v_{\theta i} \text{ at } r = a$$

which produced the total rate of energy dissipation,

$$\dot{E}_{TOTAL} = 4\pi\mu v_{\theta i}^2 \qquad (55)$$

Therefore, eqn (55) shows that the energy loss within the vortex is proportional to the square of the strength and inversely to the square of the vortex core diameter. This means that this loss is highest at the higher values of flowrate and is typically the order of a few watts.

4.5.4.3   Losses within the Vortex of the Cross Flow Fan

Equation (50) was deduced by assuming concentric streamlines throughout the rotor. If a radial velocity component was present, then this would not be the case

and pressure terms would appear in the energy equation.

The energy dissipation equation for an element of fluid,

$$\overset{\circ}{E} = \frac{1}{r}\left\{\frac{d}{d\theta}(\tau V_r) - \frac{d}{d\theta}(p V_\theta) + \tau V_\theta - p V_r\right\} - \frac{d}{dr}(p V_r) + \frac{d}{dr}(\tau V_\theta) \ ,$$

per unit volume as derived earlier. (Eqn (40)).

A free vortex with a forced vortex core is considered rotating in an infinite expanse of fluid. The free vortex has circulation Γ and the forced region has a radius 'a'. All terms with a superscript '~' refer to the free region.

1. For the free vortex, the balance of centripetal and pressure forces yields,

$$\frac{d\tilde{p}}{dr} = \rho\left\{\frac{\Gamma}{2\pi}\right\}^2 \frac{1}{r^3} \tag{56}$$

from which,

$$\tilde{p} = - \ \rho\left\{\frac{\Gamma}{2\pi}\right\}^2 \frac{1}{2r^2} + c_1$$

As $r \to \infty$, then $\tilde{p} \to 0$ $\therefore$ $c_1 = 0$,

$$\therefore \quad \tilde{p} = - \ \frac{\rho}{2r^2}\left\{\frac{\Gamma}{2\pi}\right\}^2 \tag{57}$$

At the boundary between the regions, the tangential velocity is continuous.
Therefore,

$$\omega a = \frac{\Gamma}{2\pi a}$$

$$\therefore \quad \omega = \frac{\Gamma}{2\pi a^2}$$

and this yields within the forced region,

$$V_\theta = \frac{r\,\Gamma}{2\pi a^2} \qquad\qquad (58)$$

and by a similar consideration,

$$\frac{dp}{dr} = \rho\, r\left\{\frac{\Gamma}{2\pi a^2}\right\}^2 \qquad\qquad (59)$$

and integration yields,

$$p = \frac{\rho r^2}{2}\left\{\frac{\Gamma}{2\pi a^2}\right\}^2 + C_2$$

At the boundary between the regions, the static pressure is continuous,

i.e. when $r = a$, then $p = \tilde{p}$

Hence, $\quad \dfrac{\rho a^2}{2}\left\{\dfrac{\Gamma}{2\pi a^2}\right\}^2 + C_2 = -\dfrac{\rho}{2a^2}\left\{\dfrac{\Gamma}{2\pi}\right\}^2$

$$\therefore \quad C_2 = -\frac{\rho}{a^2}\left\{\frac{\Gamma}{2\pi}\right\}^2$$

and the static pressure in the forced vortex is given by,

$$p = \frac{\rho}{a^2}\left\{\frac{\Gamma}{2\pi}\right\}^2\left(\frac{r^2}{2a^2} - 1\right)$$

$$0 < r < a$$

From eqn.(40) , τ is expressed in polar co-ordinates,

$$\tau = \mu r\,\frac{d}{dr}\left\{\frac{V\theta}{r}\right\} \qquad\qquad (61)$$

As $V_\theta/r = \omega$, for a forced vortex, then $\tau = 0$. For the free vortex,

$$\tilde{\tau} = \mu r\,\frac{d}{dr}\left\{\frac{\Gamma}{2\pi r}\cdot\frac{1}{r}\right\}$$

$$\tilde{\tau} = -\frac{\mu\,\Gamma}{\pi r^2} \qquad\qquad (62)$$

As the value of any small radial velocity component is

unknown, the differential form is introduced,

$$V_r = - \frac{1}{r} \frac{d\psi}{d\theta} \tag{63}$$

2. Consider the energy dissipation in the forced vortex region. Equation (40) becomes,

$$\overset{\circ}{E} = - \rho \frac{V_r}{r} - V_r \frac{\partial \rho}{\partial r} - \rho \frac{\partial V_r}{\partial r} \tag{64}$$

and substitution gives,

$$\overset{\circ}{E} = \frac{\rho}{r} \frac{1}{r} \frac{\partial \psi}{\partial \theta} + \frac{1}{r} \frac{\partial \psi}{\partial \theta} \frac{\partial \rho}{\partial r} - \rho \frac{d}{dr} \left\{ - \frac{1}{r} \frac{\partial \psi}{\partial \theta} \right\}$$

$$= \frac{\rho}{r^2} \frac{\partial \psi}{\partial \theta} + \frac{1}{r} \frac{\partial \psi}{\partial \theta} \frac{\partial \rho}{\partial r} - \rho \left\{ \frac{1}{r^2} \frac{\partial \psi}{\partial \theta} \right\} + \rho \left\{ \frac{1}{r} \frac{\partial^2 \psi}{\partial r \partial \theta} \right\}$$

The last term of this expression has been shown to be small from the experiments described in Chapter 2. The slope of the curves shown in Fig.2.17 is $\frac{\delta\psi}{\delta\theta}$ and there appears to be little change in this parameter with respect to radial position.

The above expression then reduces to,

$$\dot{E} = \frac{1}{r} \frac{\delta\psi}{\delta\theta} \cdot \frac{\rho r}{a^4} \left\{ \frac{\Gamma}{2\pi} \right\}^2$$

Therefore,

$$\dot{E} = \frac{\rho}{a^4} \left\{ \frac{\Gamma}{2\pi} \right\}^2 \frac{\delta\psi}{\delta\theta} \quad \text{per unit volume} \tag{65}$$

The total rate of energy dissipation within the forced region may be expressed,

$$\dot{E}_{TOT} = \int_0^a \overset{\circ}{E} \, 2\pi r \, dr \tag{66}$$

162

and from eqn (65),

$$\dot{E}_{TOT} = \left\{\frac{\Gamma}{2\pi}\right\}^2 \frac{2\pi\rho}{a^4} \frac{\delta\psi}{\delta\theta} \int_0^a r\,dr$$

$$= \frac{\pi\rho}{2} \left\{\frac{\Gamma}{2\pi}\right\}^2 \frac{\delta\psi}{\delta\theta}$$

The tangential velocity at the regions' boundary,

$$V_{\theta i} = \frac{\Gamma}{2\pi a} \tag{67}$$

and so,

$$\dot{E}_{TOT} = \pi\rho V_{\theta i}^2 \frac{\delta\psi}{\delta\theta} \tag{68}$$

3. Consider the energy dissipated in the free vortex region. Equation (40) becomes,

$$\tilde{E} = \frac{1}{r}\left\{\tilde{\tau}\tilde{v}_\theta - \tilde{p}V_r\right\} - V_r\frac{d\tilde{p}}{dr} + \frac{d}{dr}(\tilde{\tau}\tilde{v}_\theta) - \tilde{p}\frac{dV_r}{dr} \tag{69}$$

and substitution yields,

$$\tilde{E} = \frac{1}{r}\left\{-\frac{\mu\Gamma}{8r^2}\frac{\Gamma}{2\pi r} - \frac{\rho}{2r^2}\left(\frac{\Gamma}{2\pi}\right)^2\frac{1}{r}\frac{d\psi}{d\theta}\right\} + \frac{1}{r}\frac{d\psi}{d\theta}\rho\left(\frac{\Gamma}{2\pi}\right)^2\frac{1}{r^3}$$

$$+ \frac{d}{dr}\left\{-\frac{\mu\Gamma}{\pi r^2}\frac{\Gamma}{2\pi r}\right\} + \frac{\rho}{2r^2}\left(\frac{\Gamma}{2\pi}\right)^2\frac{d}{dr}\left\{-\frac{1}{r}\frac{d\psi}{d\theta}\right\}$$

$$= -2\mu\left(\frac{\Gamma}{2\pi}\right)^2\frac{1}{r^4} - \frac{\rho}{2}\frac{d\psi}{d\theta}\left(\frac{\Gamma}{2\pi}\right)^2\frac{1}{r^4} + \rho\frac{d\psi}{d\theta}\left(\frac{\Gamma}{2\pi}\right)^2\frac{1}{r^4}$$

$$+ 6\mu\left(\frac{\Gamma}{2\pi}\right)^2\frac{1}{r^4} + \frac{\rho}{2}\left(\frac{\Gamma}{2\pi}\right)^2\frac{d\psi}{d\theta}\frac{1}{r^4}$$

$$= 4\mu\left(\frac{\Gamma}{2\pi}\right)^2\frac{1}{r^4} + \rho\frac{d\psi}{d\theta}\left(\frac{\Gamma}{2\pi}\right)^2\frac{1}{r^4} \quad \text{per unit volume.} \tag{70}$$

163

Equation (66) becomes,

$$\overset{\approx}{E}_{TOT} = \int_a^\infty \tilde{E} \; 2\pi r dr \tag{71}$$

$$= \int_a^\infty \left\{ 8\pi\mu \left(\frac{\Gamma}{2\pi}\right)^2 \frac{1}{r^3} + 2\pi\rho \; \frac{\delta\psi}{\delta\theta} \left(\frac{\Gamma}{2\pi}\right)^2 \; \frac{1}{r^3} \right\} dr$$

$$= -4\pi\mu \left(\frac{\Gamma}{2\pi}\right)^2 \frac{1}{r^2} - \pi\rho \; \frac{\delta\psi}{\delta\theta} \left(\frac{\Gamma}{2\pi}\right)^2 \; \frac{1}{r^2} \Bigg]_a^\infty$$

$$= \pi \left(\frac{\Gamma}{2\pi}\right)^2 \frac{1}{a^2} \left\{ 4\mu + \rho \; \frac{\delta\psi}{\delta\theta} \right\}$$

and using eqn (67) yields,

$$\overset{\approx}{E}_{TOT} = \pi v_{\theta i}^2 \left\{ 4\mu + \rho \; \frac{\delta\psi}{\delta\theta} \right\} \tag{72}$$

The total energy dissipated within the combined vortex system is then given by,

$$\overset{\circ}{E}^* = 2\pi \; v_{\theta i}^2 \left\{ 2\mu + \rho \; \frac{\delta\psi}{\delta\theta} \right\} \tag{73}$$

Clearly, with no radial flow component,

$$\frac{\delta\psi}{\delta\theta} = 0$$

and eqn(73) reduces to the viscous losses in the free vortex region alone,

$$\overset{\approx}{E} = 4\pi\mu \; v_{\theta i}^2 \; ,$$

as derived earlier (eqn(55)).

However the major term in eqn(73) is

$$\chi = 2\pi \; v_{\theta i}^2 \; \rho \; \frac{\delta\psi}{\delta\theta}$$

A typical value of $V_{\theta i}$ for the large fan operating at $\Phi = 0.8$ is 20 ms^{-1}, giving

$$\chi \doteqdot 3000 \, \frac{\delta \psi}{\delta \theta}$$

and so, even with $\frac{\delta \psi}{\delta \theta}$ small, this momentum term may account for the reduced efficiency of the cross flow fan. Clearly, ensuring (by casing design, for example) $\frac{\delta \psi}{\delta \theta}$ is zero, benefits may be achieved.

4.6 Conclusions

The purpose of deriving a theory for the cross flow fan, like any other machine, is to provide the design engineer with useable data and to indicate where losses are likely to occur within the machine. Sensible modifications may then be attempted to improve the performance and efficiency.

It does seem that a fully predictive analytic theory is a long way off. However, some clues revealing the losses involved in such a machine have appeared. Those associated with the so-called 'shock' losses may be drastically reduced by the introduction of inlet guide vanes, although this introduces additional frictional losses and complicates the housing geometry. Losses occuring through energy dissipation within the vortex may overshadow all others and at this stage, it is unclear how these may be minimised.

Even so, the pursuit of a theoretical description is

165

paramount, for although empirical theories may produce better mathematical models, they ultimately limit the knowledge attainable from such machines and indeed the fluid dynamic processes present, which may be fundamental.

CHAPTER FIVE

CONCLUSIONS

"I can't believe God plays dice".

Albert Einstein 1879-1955

5. CONCLUSIONS

The goal of this research programme was to relate performance to aspects of aerodynamic behaviour for a large cross flow fan. Previous research has tended to concentrate on rotors of less than 300 mm diameter but there has been evidence to suggest that large rotors may behave quite differently (ref. 12).

This study complements and adds additional data to the previous research by HOLGATE and HAINES (ref. 12) and PORTER and MARKLAND (ref. 23), which may be compared to reveal important effects of the scale of cross flow machines.

Quantitative data were obtained from a large rotor previously installed in a purpose-built wind tunnel (see Chapter 2) and also from a smaller scale rotor placed in a water tank (see Chapter 3). This latter facility allowed the adoption of reliable flow visualization techniques.

A theoretical study (see Chapter 4) was aimed principally at improving the approach adopted by IKEGAMI and MURATA (ref. 13) and also contains a section detailing losses occurring in cross flow fans, as prompted by the work of MOORE (ref. 16).

51. The Aerodynamic Facility

The aerodynamic facility was designed as part of a previous research project and is reported in ref. 12. This design was a geometric scaling of a previous smaller machine that had given good results and was itself a combination

of the best designs as indicated from the results of PORTER

and MARKLAND (ref. 23) and PRESZLER and LAJOS (ref. 24).

These researchers generally agree that changes in the det-

ails of the impeller geometry have a far smaller effect

on performance than a change in the geometry of the surroun-

ding casing. Other effects of casing and rotor geometry

are more fully discussed in Chapter 2 with a summary towards

the end of this Chapter.

Tests were carried out to optimise certain casing para-

meters and any departures from previous studies were deemed

to be an effect of scaling, although the design guidelines

suggested in refs. 23 and 24 were broadly met. This com-

bined with results obtained from the hydrodynamic facility,

suggested that an examination of the aerodynamic perform-

ance of a fan operating under non-optimum conditions, would

not reveal any fundamental differences in the flow.

The flow range considered, overlapped the nomal opera-

ting region, comensurate with good efficiency.

To completely define the flow field, data were required

related to the velocity and direction of the main flow vec-

tor, together with a distribution of the total pressure

throughout the rotor interior. With these results avail-

able, it was then possible to test the validity of a Rankine

vortex model as the primary flow inducing agent.

The purpose built cranked three-hole probe (fig. 2.7)

had the added facility of hybrid operation, together with

a miniature hot-wire probe attached to the end of the shaft.

However, it was finally decided to dispense with hot-wire

amemometry for these reasons,

(i) Preliminary tests indicated highly turbulent flow within the rotor, particularly in the vicinity of the vortex core, making the use of hot-wire anemometry considerably difficult, without large time-constants being imposed on the DC output signals.

(ii) Close to the vortex core, the determination of flow direction was often difficult and the possibility of aerodynamic interference by the sensor support prongs was deemed to be a problem.

(iii) Without using several probe orientations at a given r, θ coordinate within the flow field, it was not possible to eliminate the cooling effect on the sensor resulting from the flow vector parallel to the axis of the rotor (partially due to secondary flows).

(iv) It is possible to deduce pressure distributions using a hot-wire probe but the analysis of such data can be difficult and, at best, is expressed in terms of a pressure gradient distribution.

For these reasons, it was decided to make use of the standard, proven three-hole probe technique; the calibration and subsequent use being very straightforward and reliable.

Figures 2.19(a) and (e) show the change in the streamline patterns over the flow range, $\Phi = 0.4$ to 0.8, which is generally considered to be the typical operating region for a cross flow fan. As an example of the changes observed, the streamline $\psi = 0.0$, passing through the rotor centre-line, exhibits a clockwise rotation as the flow rate is reduced. Clearly, this follows the position of the vortex core, which changes little over the flow range until

170

throttling reduced the flow rate towards $\Phi=0.4$, where it is seen to move radially.

A general acceleration of the flow is seen to occur across the rotor interior at all flow rates. The flow velocities in the vicinity of the vortex core (as judged by the radial separation between the streamlines) reduce dramatically as the flow rate reduces. The streamlines in the quadrant opposite the vortex core flatten and in some cases show reflex curvature as the distance away from the vortex increases. It is from this region that flow escapes back towards the suction region and over the leading edge of the rear wall (see visualization study, Chapters 3 and PELHAM (ref. 21) for confirmation).

The total pressure distributions shown in figs. 2.20(a) to (c), further confirm the existence of a Rankine type vortex within the impeller. The boundaries of the pressure regions, approximately follow the streamlines; themselves being lines of constant total pressure. As the flow rate reduces, the total pressure depression (related to the vortex strength) within the vortex becomes less intense as the flow velocities reduce, until at $\Phi = 0.4$, a single region is apparent around the vortex core, with the surrounding region becoming less depressed and more extensive.

A second region of depressed total pressure is present diametrically opposite the vortex, which is most apparent at higher flow rates. As the flow rate reduces and the flow from this region begins to pass towards the suction region, this quadrant becomes energised with a resulting increase in total pressure.

5.2 The Hydrodynamic Facility

Initial investigations were carried out to determine
which changes to the casing geometry caused significant
variations in the observed hydrodynamic performance, in
terms of flow reversal and separation, for example. Satis-
factory results were achieved following the guidelines
laid out in Chapter 2 and for the majority of tests, casing
geometries were used where dynamic similarity with the
aerodynamic facility was met.

Studies to date have used visualization techniques to
provide qualitative data yielding a development guide to
the design of full size machines. From the outset, this
research concentrated on photographic techniques suitable
for the extraction of quantitative data, so that a direct
comparison with the aerodynamic study would be made. Alth-
ough it was eventually possible to accurately measure local
flow velocities, as judged by streak lengths on the emul-
sion, several frames showing the same casing geometry and
throughflow, were needed to fully analyse the various flow
regions (see fig. 3.8). Many of the streaks had to be eli-
minated as they were deemed to have been caused by a part-
icle passing across the light beam during the open-shutter
period and as such, were comprised of a velocity component
parallel to the rotor axis (see fig. 3.10, for example)

Important information was revealed about the jet of
fluid passing over the rear wall from within the rotor.
Details of this flow region have been difficult to ascer-
tain from direct measurements on the aerodynamic facility
(PELHAM (21)). The visualization study shows how the flow

rate associated with this jet, increases as the throttling

increases. Extending the rear wall height,α_1 , attempting

to prevent this loss, has little benefit and can generate

a worse situation (see Table 3.2). From this consideration

alone, $\alpha_1 = 20°$ appears a reasonable optimum.

Analysis of photographic records is open to a more aut-

omated approach, rather than the tedious manual method

adopted here. However, flow visualization studies of this

kind, will continue to be a powerful design and analysis

tool when care is taken with accurate modelling and the

correct interpretation of the final photographic records.

5.3   Theory of the Cross Flow Fan

The mathematical model of IKEGAMI and MURATA (13) is

the only one able to predict a fan performance and include a

rudimentary casing. All other theories are for fixed flow

situations and include no effect of casing (7, 15, 16).

The development of an improved theory and the experi-

mental studies on both the aerodynamic and hydrodynamic

rigs, were carried out in parallel. Interesting experimen-

tal results were thus adapted for the mathematical model.

However, a primary feature of the original model is the

relationship between the locus of the vortex over the flow

range and the resulting fan performance curve. As previou-

sly mentioned, a change in the throughflow produced a

change in the total pressure distribution rather than a

significant movement of the vortex. Studies on both rigs

indicated reflex curvature of the streamlines for the flow

region opposite the vortex. Incorporating this in the

model, by means of a source and sink, allowed the strength
of the vortex to change as a function of its position with-
in the rotor. Figure 4.22 indicates a similar trend as
found by experiment, with large changes in strength occur-
ring as the vortex moves away from the inner periphery of
the rotor and in a peripheral sense, away from the vortex
wall.

5.4 Losses Within the Vortex

Losses within a vortex were examined theoretically,
as prompted mainly by the work of MOORE (16), who suggested
that these may account for the low efficiency generally
found in cross flow fans. The vortex was considered to
be of the Rankine type, consisting of a forced vortex core
surrounded by a free vortex region.

Important changes in the final equations were revealed,
when non-concentric streamlines were considered. This
implies a radial flow component, relative to the vortex
core centre, which is to be expected in practice, as the
fluid passing across the rotor interior experiences a deg-
ree of acceleration. Terms were developed related to the
momentum of the fluid (having ρ as a coefficient) which
when compared to the viscous loss, were found to be sev-
eral orders of magnitude higher.

Although the Rankine vortex was considered to lie in
an infinite expanse of fluid, eqn. 73 indicates the strong
possibility of non-concentric streamlines being respons-
ible for large losses in a cross flow rotor. It does seem
therefore that changes in casing geometry, yielding an

174

internal flow field with a tendency towards concentric
streamlines, are likely to produce an overall improved
efficiency.

5.5   The Modern Design of Cross Flow Fans

To clarify the design opinion of modern cross flow
fans, the author has compiled a list of all design para-
meters and features, giving optimum values where relevant.
This is based on the research by HOLGATE and HAINES (12),
IKEGAMI and MURATA (14), MURATA and NISHIHARA (18), PORTER
and MARKLAND (23), PRESZLER and LAJOS (24) with a more
recent study by ALLEN (1).

5.5.1   The Vortex Wall

This is the most important geometrical parameter. The
location of the vortex wall leading edge, α_2 (fig. 2.2)
should be in the range $30^\circ \lessgtr \alpha_2 \lessgtr 40^\circ$, for optimum per-
formance. The results from the visualization study (Chap-
ter 3) indicate a dividing streamline between the inflow
and outflow within this range, for a rotor operating in
unbounded fluid (see fig. 3.5). However quieter operation
occurs at lower values of α_2, at the expense of aerodyn-
amic performance.

The thickness of the vortex wall will generally be dic-
tated by the material stiffness but should not exceed 0.04
of the rotor diameter. A flat wall is recommended with
a rounded leading edge, as shaped walls only assist in

175

obstructing the inflow in what is clearly a high velocity region of the suction arc.

From performance and manufacturing considerations, the clearance of the vortex wall leading edge from the rotor blades, ε_2 , should be about 0.03 of the rotor diameter. Although noise levels reduce drastically with increased clearance, the aerodynamic performance suffers as a result.

5.5.2 The Rear Wall

The location of the rear wall leading edge, α_1, should be about 20° but efficiency does not appear to be affected with values as high as 40°.

The optimum value of the clearance of the rear wall leading edge from the rotor blades, ε_1 , is a function of other design parameters. If this cannot be deduced experimentally, values within the range $0.09 \leqslant \varepsilon_1/D_2 \leqslant 0.125$ should be found to be satisfactory.

It is generally accepted that a logarithmic spiral rear wall profile produces the best performance. This shape should be developed from the location $\alpha_1 = 0°$ to meet the duct base tangentially, directly below the vortex wall leading edge. Any height extensions to the rear wall ($\alpha_1 \geqslant 0°$) should be at a constant clearance of ε_1 , i.e., circular arc.

5.5.3 The Rotor

The length to diameter ratio, L/D_2 should be less than 2.3 to prevent the line vortex breaking into segments and greater than 1.0 to avoid secondary flows within the rotor. An optimum exists around 1.6.

The diameter ratio, D_1/D_2, lies ideally within the range $0.72 \leqslant D_1/D_2 \leqslant 0.76$ but good performance has been found over the wider range $0.70 \leqslant D_1/D_2 \leqslant 0.80$.

As a result of the large changes in flow velocity and deviation around the suction arc, no optimum value for the outer blade angle, β_2, exists (see fig. 4.25). However, the so called 'shock losses' may be reduced if the deviation is minimised over the portion of the suction arc where the throughflow is greatest, i.e. near the vortex wall. This yields an angle $25° \leqslant \beta_2 \leqslant 35°$ with higher performance towards the lower end of this range and 26° representing an optimum. It is important to maintain this angle at values greater than 22° for stable operation.

Theoretical studies, based on a simple Rankine vortex lying within the rotor, for example, require the inner blade angle, β_1, to be 90°. Whilst most of these models are imperfect, little effect of changes in this angle within the range $60° \leqslant \beta_1 \leqslant 100°$ are usually observed. Therefore, there appears no reason why this angle should not be approximately radial.

Clearly there exists a trade-off between increasing the number of blades, giving improved guidance to the flow and a reduced blade number, lowering the resistance to flow. ECK (10) suggested 36 but COESTER (7) was most successful with 24. PORTER (22) experienced unstable flow conditions using 18 blades because of unsatisfactory flow guidance. For these reasons, a value within the range $24 \leqslant N \leqslant 36$, should give good results.

The blade profile is generally chosen as a circular arc camber, since each blade experiences flow reversal on passing from the suction to the discharge regions. There may be slight advantage in profiling the blades to suit the flow present at the first or second pass (as suggested by MOORE (16)) but the constructional complexity would generally prohibit such a development.

The optimum location and geometry of internal blades or bodies, is a function of flow rate amongst other fan design parameters. Elaborations of this kind would greater complicate the rotor geometry and as there is little evidence to support their use in terms of vortex location and stabilization, internal blades or bodies are not recommended.

Rotor inlet guide vanes would be a benefit if it was felt that the improved performance, resulting from the reduction in 'shock losses', justified the extra complication in housing geometry. Vane settings could be calculated as indicated in section 4.5.4.1 and the number of vanes refined by experiment.

PORTER and MARKLAND (23) improved operating stability by including a single recirculation vane in the suction region, towards the rear wall. This probably assisted in deflecting the flow lost over the rear wall, back towards the intake (as found in the visualization study, Chapter 3) but was not strictly an inlet guide vane.

Unless inlet guide vanes are to be used, the suction arc should be unobstructed by ducting, especially close to the vortex wall and ideally, the rotor should be allowed to draw fluid from free space.

5.5.4 Fans in Series

This arrangement is supposed to produce a compact, high-pressure unit. However, stability problems may arise because of flow distortion on entry to successive rotors, together with mis-matching of the individual rotors (see British Patent 816,689).

5.5.5 Fans in Parallel

This novel design by GUNTON and HOLGATE (v) has the advantage of a simplified casing geometry. However, the suction flow must be symmetrical about the duct centre-line, otherwise one of the fans may tend to 'windmill'.

As a general guide to cross flow fan design, it is found that the simplest casing design is the best to use. Future designers must be aware that complicated modifications which only marginally improve the performance or

efficiency will decrease the commercial competitiveness
of the cross flow fan.

REFERENCES

1   ALLEN, D.J.   :   "The Effect of Rotor and Casing Geometry on the performance of Cross Flow Fans."   International Conference on Fan Design and Applications, Guildford, 1982.

2   ANDERSON, E.L.   :   U.S. Patents nos.   1823 579 (1931), 1838 169 (1932), 1920 952 (1933).

3   ASANUMA, T. and TAKEDA, S.   :   "A study on the Flow Visualization by the Hydrogen Bubble Method."   Bulletin of J.S.M.E.,   8, 32, 1965, pp. 599-608.

4   BUCK, C.M.   :   U.S. Patents nos. 1893 857 (1933), 2033 273 (1936).

5   CLAYTON, B.R.   :   "A Review and Appraisal of Cross Flow Fans."   Building Services Engineer (I.H.V.E.), 42, Jan., 1975, pp. 230-247.

6   CLAYTON, B.R. and MASSEY, B.S.   :   "Flow Visualization in Water: a Review of Techniques."   J. Sci. Instrum.,

7   COESTER, R.   :   "Remarks on the Theory of Cross-Flow Fans."   H.V.R.A. Translation No. 39 of "Theoretische und experimentelle untersuchungen an querstromgeblasen."   Mitt. aus dem Institut für Aerodyn., E.T.H., Zurich, No. 28, 1959.   U.S. Patent No. 2965 284 (1960).

8   DALIN, H.   :   U.K. Patent No. 291 007 (1928).

9   DÄTWYLER, G. :   U.K. Patent No. 988 712 (1965).

10 ECK, B.   :   "Fans."   Oxford, Pergamon Press, 1973, pp. 156-182.
    U.K. Patent No. 757 543 (1954).

11 FAURE, J.   :   Houille Blanche, 18, 1963, pp. 298-306.

12 HOLGATE, M.J. and HAINES, P. : "Scaling of Cross flow fans - an Experimental Comparison." <u>Proc. I. Mech. E. Conference on Scaling for Performance Prediction in Rotodynamic Machines</u>, Stirling, 1977.

13 IKEGAMI, H. and MURATA, S. : "A Study of the Cross Flow Fan: Part 1: A Theoretical Analysis." <u>Technology Rep</u>. Osaka Univ., 16, 1966, No. 731.

14 IKEGAMI, H. and MURATA, S. : "Experimental Study of the Cross Flow Fan." Science of Machine, 18, 3, 1966, pp. 557-566. (In Japanese).

15 ILBERG, H. and SADEH, W.Z. "Flow Theory and Performance of Tangential Fans." <u>Proc. Inst. Mech. Engrs</u>., London, 180, 1965-66, pp. 481-496.

16 MOORE, A. : "The Tangential fan - analysis and design." <u>Conference on Fan Technology and Practice</u>, Institute of Mechanical Engineers, London, April 1972.

17 MORTIER, P. : U.S. Patent No. 507 445 (1893).

18 MURATA, S. and NISHIHARA, K. : "An Experimental Study of Cross Flow Fan (1st. Report, Effects of housing geometry on the Fan Performance)." <u>Bulletin of J.S.M.E.</u>, 19, March 1976, pp. 314-321.

19 MURATA, S. and NISHIHARA, K. : "An Experimental Study of Cross Flow Fan (2nd Report, Movements of Eccentric Vortex inside impeller)." <u>Bulletin of J.S.M.E.</u>, 19, March 1976, pp. 322-329.

20 MURATA, S., OGAWA, T., SHIMIZU, I., NISHIHARA, K. and KINOSHITA, K. : "A Study of the Cross Flow Fan with inner guide apparatus." <u>Bulletin of J.S.M.E.</u>, 21, April 1978, pp. 681-688.

21 PELHAM, G. : "Inlet Streamlines of the Cross Flow Fan." <u>Final Year Project</u>, Durham University, 1979.

22 PORTER, A.M. : "A Study of the Tangential Fan." Ph.D. Thesis,
    Queens University, Belfast, 1969.

23 PORTER, A.M. and MARKLAND, E. : "A Study of the Cross Flow Fan."
    Journal of Mechanical Engineering Science, 12, 6, 1970, pp. 421-
    431.

24 PRESZLER, L. and LAJOS, T. : "Experiments for the development of the
    Tangential Flow Fan." Proc. 4th Conf. on Fluid Machinery, (Budapest,
    1972), Akademiai Kiado, pp. 1071-1082.

25 ROBERSON, E.C. : Report of the National Gas Turbine Establishment
    No. R. 181, 1955.

26 TRAMPOSCH, H. : "Cross Flow Fan." Paper A.S.M.E. No. 64-WA FE-26,
    1964.

27 TUCKEY, P.R., HOLGATE, M.J. and CLAYTON, B.R. : "Performance and
    Aerodynamics of a Cross Flow Fan." International Conference on Fan
    Design and Applications, Guildford, 1982.

28 YAMAFUJI, K. : "Studies on the flow of Cross Flow Impellers (1st
    Report, Experimental Study)." Bull. Jap. Soc. Mech. Engrs., 18,
    Sept. 1975, pp. 1018-1025.

29 YAMAFUJI, K. : "Studies on the flow of Cross Flow Impellers (2nd
    Report, Analytical Study)." Bull. Jap. Soc. Mech. Engrs., 18, Dec.
    1975, pp. 1425-1431.

USEFUL REFERENCES (not mentioned in the text)

(i)   BUSH, E.H.: "Cross Flow Fans." Conference on Fan Technology and Practice, I. Mech. E., London, April, 1972.

(ii)   CLUTTER, D.W., and SMITH, A.M.O.: "Flow visualization by Electroylsis of Water." Aerospace Engineering, 20, Jan., 1961, pp. 24-27 and 74-76.

(iii)   DE-FRIES, J.R.: "66 Jahre Querstrom Ventilator." UDI-Berichte uber betriebswissen scheftliche, Arbeiten, Vol. 38, 1959, pp. 75-86.

(iv)   GELLER, E.W.: "An Electrochemical Method of visualiz-the Boundary Layer." Journal of Aeronautical Science, 22, 1955, pp. 869-870.

(v)   GUNTON, M. and HOLGATE, M.J.: "Research Note – A Twin Rotor Cross Flow Fan." Journal of Mech. Eng. Science, I. Mech., E., 1978.

(vi)   HAMA, F.R. and NUTANT, J.: "Detailed Flow Field Observations in the Transition Process in a Thick Boundary Layer." Proc. Heat Transfer Fluid Mech. Inst., 1963 pp. 77-93.

(vii)   LOCKLEY, D.J.: "The Tangential Fan." M.Sc. Thesis, Birmingham University, 1966.

(viii)   SCHRAUB, F.A., KLINE, S.J., HENRY, J., RUNSTADLER Jr., P.W. and LITTELL, A.: "Use of Hydrogen Bubbles for Quantitative Determination of Time-Dependent Velocity Fields in Low-Speed Water Flows." Journal Bas. Eng., 87, 1965, pp. 429-444

(ix)   SHAPIRO , A.H.: "Design of Tufts for Flow Visual-

         zation." A.I.A.A. Journal, 1, 1963, pp. 213-214.

(x)   SHAPIRO, A.H.: "Educational Films in Fluid Mechanisms."

         Nominated Lecture, Proc. Inst. Mech. Engrs., 178, 1, 1963-

         64, pp. 1187-1204.

(xi)   STEPANOFF, A.J.: "Turboblowers: theory, design and

         Application of centrifugal and axial flow compressors and

         fans." Published by Wiley, New York, 1955.

APPENDICES

Appendix 1   Determination of the mid-span Deflection of a Cross Flow Fan Blade.

An exercise was carried out to determine the mid-span deflection of a cross flow fan blade under the influence of centrifugal loading, assuming fluid pressure forces to be negligible and the end connections considered somewhere between encastre and pinned (pinned being the worst case).

The centrifugal loading is uniformly distributed along the blade length. Fig. A.1 represents the force system solved by the Macaulay method. The calculation yields

$$R_a = R_b = \frac{wl}{2} \qquad\qquad (1)$$

$$M_a = -M_b = \frac{wl^2}{12} \qquad\qquad (2)$$

and the maximum deflection given by

$$Y_{MAX} = \frac{-wl^4}{384 \ EI} \qquad\qquad (3)$$

The uniformly distributed load w can be easily determined but the value of I is less straightforward. Consider an element of a circular camber constant thickness blade, as shown in Fig. A.2

$$\delta A = r\delta\theta \ t \qquad\qquad (4)$$

The second moment of area about XX is given by

$$I_{XX} = \int y^2 \ \delta A = 2\int_o^{\alpha/2} (r \sin\theta)^2 \ rt \ \delta\theta$$

$$= \frac{r^3 t}{2}(\alpha - \sin\alpha) \qquad\qquad (5)$$
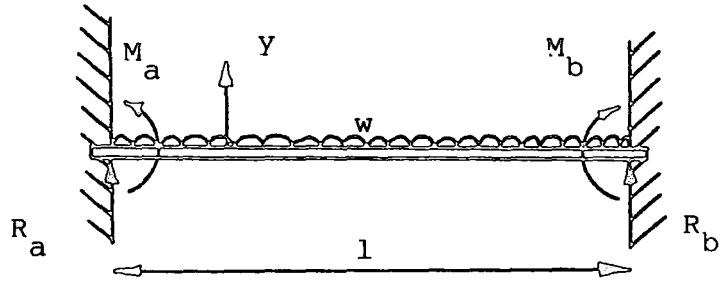
Figure A.1   BLADE LOADING DIAGRAM
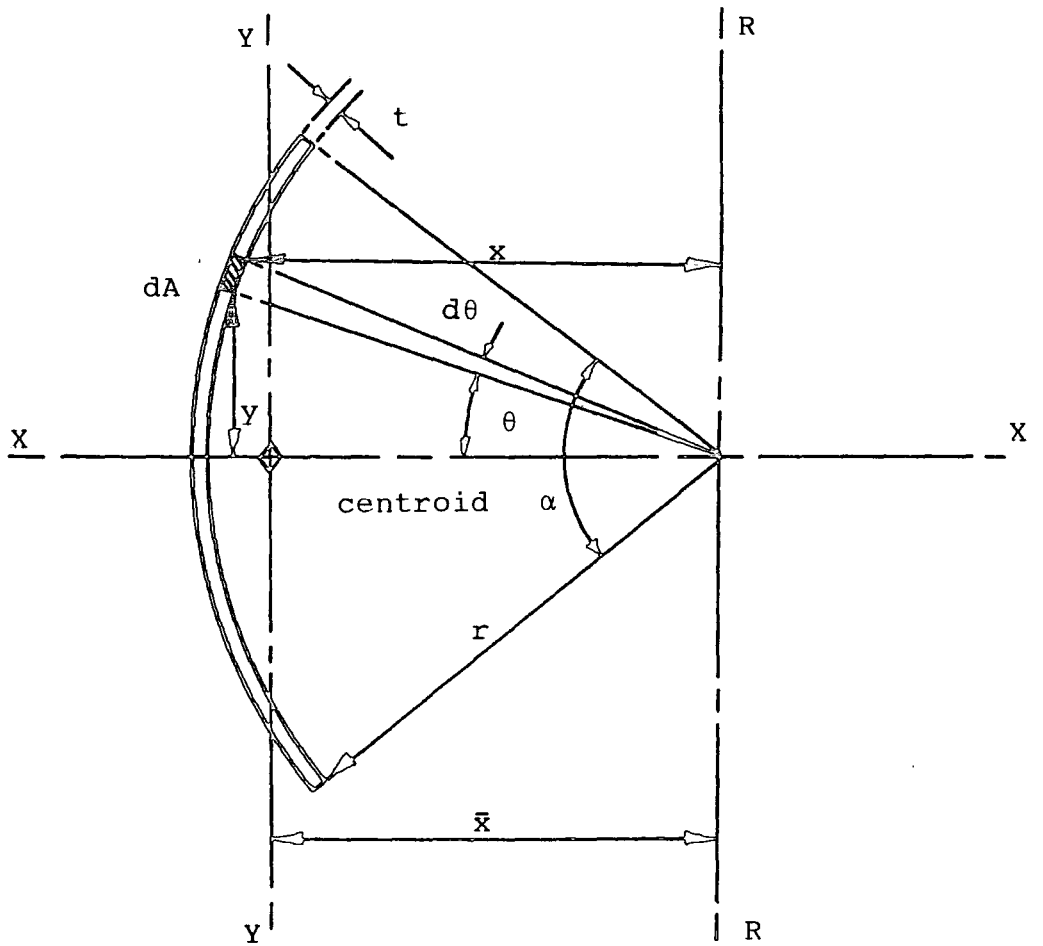
Figure A.2   CALCULATION OF BLADE MOMENT OF INERTIA

188

The second moment of area about RR is similarly

$$I_{RR} = \int x^2 \, \delta A = 2\int_0^{\alpha/2} (r \cos\theta)^2 \, rt \, \delta\theta$$

$$= \frac{r^3 t}{2} (\alpha + \sin\alpha) \tag{6}$$

Finally the second moment of area about YY

$$I_{YY} = I_{RR} - A\bar{x}^2 \tag{7}$$

The total blade area

$$A = 2\int_0^{\alpha/2} rt \, \delta\theta = rt\alpha \tag{8}$$

and as

$$A\bar{x} = \int x \, \delta A$$

then

$$\int x \, \delta A = 2\int_0^{\alpha/2} r \cos\theta \, rt \, \delta\theta$$

$$= 2r^2 t \, \sin\alpha/2$$

from which

$$\bar{x} = \frac{2r}{\alpha} \sin \alpha/2 \tag{9}$$

Therefore,

$$I_{YY} = \frac{r^3 t}{2}(\alpha+\sin\alpha) - rt\alpha\left(\frac{2r}{\alpha} \sin \alpha/2\right)^2$$

$$= r^3 t \left\{ \frac{(\alpha+\sin\alpha)}{2} - \frac{4}{\alpha} \sin^2 \alpha/2 \right\} \tag{10}$$

As an example of the calculation of the mid-span

189

deflection, the blades parameters are:

r = 21.66 mm, t = 1.22 mm and α = 55°

with, β_1 = 90° (radial), blade mass = 22.7 gms, l = 320 mm

the diameter of the rotor = 200 mm and N = 1000 rev. min^{-1}.

substitution into eqns.(5)&(10) yield:

$$I_{XX} = 872 \text{ mm}^4$$

and I_{YY} = 13.7 mm^4

The centrifugal loading is given by

$$F = mR\omega^2 = 24.89 \text{ N}$$

The forces may now be resolved on to the XX and the YY

planes;

$$F_{XX} = 22.08 \text{ N}$$

and F_{YY} = 11.49 N

Eqn.3 then yields the respective deflections;

$$d_{XX} = \frac{F_{XX} \, l^3}{384 E I_{XX}} = 3 \times 10^{-5} \text{ m}$$

$$d_{YY} \doteqdot \frac{F_{YY} \, l^3}{384 E I_{YY}} = 9.9 \times 10^{-4} \text{ m}$$

These deflections are finally resolved into the radial

direction

$$d_r = d_{XX} \cos\theta + d_{YY} \sin\theta$$
$$= 4.3 \times 10^{-4} \text{ m}$$

For the case with pinned ends

$$Y_{MAX} = \frac{-5w\, l^3}{384EI} \qquad (11)$$

and so the maximum deflection to be expected is 2.4 mm.

A composite design formula is written here for completeness.

$$d_r = \frac{\rho \alpha R N^2 \pi^2 l^4}{69000 E r^2}\left\{ \frac{2\,\cos^2\alpha/2}{\alpha - \sin\alpha} + \frac{\sin^2\alpha/2}{\tfrac{1}{2}(\alpha + \sin\alpha) - \frac{4}{\alpha}\sin^2\alpha/2} \right\} \qquad (12)$$

where, ρ = blade material density, $kg.m^{-3}$

     α = blade curvature angle ,   rad.

     R = fan rotor radius,   m

     N = fan rotation speed,   rev. min^{-1}

     l = blade length,   m

     E = YOUNG'S modulus,   Pa

and   r = blade curvature.   m

The author emphasises that this deflection is not the maximum to be expected. However, this radial component of deflection is important when designing the casing clearances.

It may be demonstrated from eqn (12) that the radial deflection as a ratio of the rotor radius can be expressed

$$\frac{d_r}{R} \propto \left\{\frac{L}{D}\right\}^4 U^2$$

$$= \text{(length to diameter ratio)}^4 \times \text{(blade tip speed)}^2 \quad (13)$$

For the fan tested in the aerodynamic rig, the mid-span deflection at 500 rev. min^{-1} was found from eqn (12) to be 13.50 mm.

PERFORMANCE AND AERODYNAMICS OF
A CROSS FLOW FAN

P. R. Tuckey

University College London, U. K.

M. J. Holgate

University of Durham, U. K.

B. R. Clayton

University College London, U. K.

Summary

Experimental results are presented which show the internal flow régime of a large cross flow fan of rotor length 1.0 m and outside diameter 0.625 m. Details of the flow field are examined for a range of flow coefficient ϕ between 0.4 and 0.8. Measurements are transformed into streamlines for the purposes of illustration and the corresponding variations of the total pressure coefficient are also given. Flow visualization techniques have been applied to a 1:6.25 dynamically similar scale model operating in water and photographs representing the flow are discussed. A Rankine-type vortex near the periphery is confirmed but it is found to remain substantially stationary over the flow range investigated. The total pressure distribution indicates the growth and weakened circulation of the forced vortex core as flow rate reduces. These data are used to improve a previous theoretical model in which the location of the vortex is used to define the operating point on the fan characteristic.

NOMENCLATURE

a   = factor relating radial vortex location

B   = blockage factor

c   = chord length

D   = diameter

h   = distance

k'   = suction region flow function

K   = constant value

L   = fan length

m   = strength of source (and sink)

N   = blade number

p   =. pressure

q   = local flow velocity

Q   = volume flow rate

r   = radius

$\tilde{t}$ = total pressure coefficient

u   = blade velocity

V   = fluid velocity

α   = casing location

β   = blade angle

$\hat{\beta}$ = deviation from blade angle

Γ   = vortex strength

ε   = casing clearance

θ   = angle

Θ   = peripheral vortex location

μ   = viscosity of air

ρ   = density of air

Φ   = $\frac{Q}{LD_2 u_2}$ flow coefficient

ψ   = stream function

Ψ   = $\frac{p}{\frac{1}{2}\rho u_2^2}$ pressure coefficient

ω   = rotational speed

Subscripts

1   = fan inner periphery

2   = fan outer periphery

r   = radial

s   = static

t   = total

to   = total on fan centre-line

θa   = tangential on free/forced vortex boundary

θ   = tangential

1. INTRODUCTION

Although cross flow fans have been designed and built for nearly a century there still remain ambiguities and a lack of precision in the description of the aerodynamic behaviour of these devices. Many of the difficulties arise from the presence of numerous geometric variables which are deemed to have an influence on performance and even now optimisation criteria are not universally accepted. Nevertheless, the dominant feature of a cross flow fan (and to a large extent its vertical axis wind turbine counterpart) lies in the inherent unsteady, non-uniform aerodynamics of the rotor. The passage of blades through vortex cores, the reversal of flow direction relative to the blade during one rotation and the presence of highly turbulent flow zones present problems of extreme difficulty for the analyst. An appraisal of these problems is given by Clayton (Ref. 1) who additionally brought together a wide range of data in order to provide design guide lines. Since that work was completed further information on the scaling of cross flow fans has been given by Holgate and Haines (Ref. 2). Japanese research workers have also completed programmes on small rotors e.g. Refs 3-6.

Yamafuji (Refs 3, 4) conducted experiments with a small (160mm o.d.) isolated rotor in an effectively unbounded flow contained by a water tank. He was able to show that a stable eccentric vortex could be formed, located close to the periphery of the rotor provided that the Reynolds number based on outer peripheral velocity and blade chord length exceeded about 250. Under these circumstances a through flow across the rotor was established. Using the implications of this and other experimental work an actuator disc theory was developed in Ref. 4. Good agreement with experiment was found including some examples in which simple casing geometries were specified.

Murata and Nishihara (Ref. 5) used a somewhat larger rotor of 240mm o.d. and examined the influence of a variety of casing parameters on performance. These generally tended to confirm the optimised values used for the present design. In Ref. 6 these workers investigated the shape of the fan performance curves in relation to controlled adjustments of the casing. In this and the previous work the vortex centre formed near the periphery of the rotor and was observed to move away from the vortex wall (or tongue) and towards the rotor centre line as the flow rate was reduced from its maximum value. Further systematic studies were conducted by Murata et al (Ref. 7) into the effects of guide vanes within the rotor which encircled the vortex region.

Previous workers have tended to use quite small rotors (i,e. less than 300mm o.d.) but there has been some evidence to show that large rotors may behave differently. In order to clarify some of the areas of doubt concerning the aerodynamics of cross flow fans an experimental and theoretical research programme has been undertaken. Quantitative data were obtained from a large rotor installed on a purpose-built wind tunnel and also from a smaller scale rotor placed in a water tank. This latter facility also allowed the adoption of reliable flow visualization techniques. The theoretical studies were aimed principally at improving the approach adopted by Ikegami and Murata (Ref. 8).

2. AERODYNAMIC FACILITY

The need for a simple, straight-through, open-circuit wind tunnel with a conventional test section led to the specification of a cross flow fan as the primary source of air supply. It was also possible to investigate the aerodynamic performance of the fan itself. A side elevation of the principal features of the complete rig is shown in Fig. 1. The requirements for the wind tunnel test section indicated that the fan needed to supply air at $10m^3s^{-1}$ and develop a static pressure rise of 1kPa. An examination of previous data showed that a value of the flow coefficient $\Phi = 0.6$ would correspond to optimum efficiency and approximately maximum static pressure coefficient $\Psi_s = 2.2$ and also result in a delivery flow reasonably free from pulsations i.e. a stable flow. These considerations resulted in the following rotor parameters; length L = 1.0m, outside diameter $D_2 = 0.625m$, rotational speed of 6.67 rev s $^{-1}$. A variable speed drive was incorporated between the motor and the fan so that fan speeds between 5 and 16 rev s^{-1} could be set. Experiments on this large fan which confirmed the expected performance have been previously reported by Haines and Holgate (Ref. 2).

2.1 Geometry of rotor

The main geometric parameters of a cross flow fan rotor are illustrated in Fig. 2.
Numerical values of these parameters for the rotor tested are summarized in Table 1
and were the same as those used in the previous research project (Ref. 2). The 24
identical blades are forward curved and symmetrically arranged round the circumference
of the rotor. Each end of the rotor is blanked-off by plates which carry the bearings
and housings for fixing to the main support frame.

The appraisal in Ref. 1 led to the formulation of some design 'rules'. For example,
a change in the details of the impeller geometry was found to have a far smaller
effect on performance than a change in the geometry of the surrounding casing. The
present fan blades are therefore of constant cross-section and rounded at the
leading and trailing edges. Since each blade experiences a flow reversal on passing
from the suction to the discharge region a circular arc camber has been used. It
was felt that any attempt to add a variable thickness profile to the blades was
unlikely to improve performance or reveal any otherwise unseen flow behaviour;
constructional complexity would also be increased. Using the continuity and momentum
equations it was shown by Eck (Ref. 9) that $\beta_1 = 90°$ although little effect of changes
in this angle over the range 60-100° is usually observed. Values of β_2, on the other
hand, have been optimised on the basis of measurements with the result that $\beta_2 > 22°$
for stability with, say, 26° representing an optimum. The number of blades appears to
be of secondary importance with the final choice resulting from a compromise between
torsional and bending rigidity, friction losses and the cascade effect on flow
deflection. A central shaft should be avoided and has been so in the present case.
The diameter ratio D_1/D_2 also appears not to be a critical parameter within the
range 0.70 - 0.85 and an average value was accepted.

It is possible to increase the flow rate linearly with increase of rotor length at a
given speed of rotation. There are limitations to this, however, owing to the
tendency for the line vortex to break down into shorter line vortices with a consequ-
ent deterioration in overall performance. Alternatively, if the rotor is too short
significant secondary flows develop between the ends and these grossly distort the
flow through the rotor core and at the discharge periphery.

2.2 Geometry of the vortex and rear walls.

Following the earlier controversy surrounding the function and geometry of the vortex
wall there now seems little doubt that a simple straight wall with a rounded leading
edge produces good fan performance. A compromise between noise and efficiency led to
a clearance (see Fig. 2) of $\varepsilon_2/D_2 = 0.04$, a value easily attainable with straight-
forward manufacturing techniques. The peripheral location of the leading edge of the
vortex wall was based on the results of Murata and Nishihara (Ref. 5), Ikegami and
Murata (Ref. 10), Porter and Markland (Ref. 11) and Preszler and Lajos (Ref. 12) and
a value of $\alpha_2 = 36°$ was chosen.

It has only been recently that the importance of the rear wall in helping to stabilize
the vortex core has been appreciated. A logarithmic spiral shaped rear wall was
advocated in Ref. 11 and has been used herein. A schematic layout of the present fan
and surrounding ductwork is shown in Fig. 3 and it can be seen that no straight wall
diffuser is attached to the discharge casing beyond the point where the tangent to
the rear wall becomes parallel to the vortex wall. An examination of previous work
indicated no clear recommendation for the incorporation of a straight walled
diffuser just downstream from the fan. The effectiveness of a diffuser is greatly
reduced by the presence of a strongly non-uniform velocity at its entrance and this is
precisely the condition at exit from the cross flow fan. Diffusion of the flow takes
place mainly in the region enclosed by the rear wall which acts as the volute plus the
natural diffusion due to the vortex location. It was found in Ref. 2 that diffusion
became too great, leading to flow separation and reversal, when a logarithmic rear
wall was used with its leading edge located diametrically opposite the leading edge of
the vortex wall. To combat this problem a logarithmic spiral was developed from the
leading edge at $\alpha_1 = 0$ (see Fig. 2) but with a circumferential extension attached to
the leading edge extending forwards to $\alpha_1 = 20°$ at a clearance $\varepsilon_1/D_2 = 0.05$ as shown
in Fig. 3. This geometry led to an optimum rotor, of large size, which combined the
attributes of high efficiency and low noise levels.

Four symmetrically placed pressure tapping holes were located in the casing in a plane 3 rotor diameters downstream from the leading edge of the vortex wall. The mean response from these tappings was used to calculate the static pressure rise across the fan and hence the static pressure coefficient ψ_s. The test section of the wind tunnel had been previously calibrated in terms of flow rate related to the centre line velocity and thus the flow coefficient ϕ and the total pressure coefficient ψ_t were easily determined. The performance curves for the present fan (at a rotational speed of 6.67 rev s^{-1})in terms of these parameters are shown in Fig. 4. It can be seen that the design requirement is met and subsequent data will be related to these curves.

3. HYDRODYNAMIC FACILITY

Flow visualization techniques are often used to indicate the general nature of the flow behaviour but with care some may be developed to yield quantitative data particularly for water flows (Ref. 13). Hydrolysis of water generates hydrogen bubbles from a cathode when d.c. is supplied between electrodes. If the cathode takes the form of a thin wire a very fine cloud of bubbles is formed which appears as a line when viewed edgewise. It is also possible to pulse the supply to obtain time-streak markers. However, the highly turbulent flow in and around a cross-flow rotor was found too great to allow any reasonably sustained stream to be observed especially on passing through blade passages where the bubbles were totally dispersed, although general flow patterns could be discerned. It was therefore decided to opt for a method by which neutral density polystyrene beads could be introduced into the flow.

The test facility consisted of a rectangular tank with sides made from heavy gauge perspex sheet. Deflections of the assembly when full of water were minimised by supporting the sides and bottom with a steel bracing framework. The model rotor, built to a geometric scale of 1:6.25, was installed towards one corner of the tank with its axis of rotation vertical. The drive shaft attached to the lower end of the rotor passed through a seal in the base of the tank and was attached by pulleys and a timing belt to an a.c. motor. Dynamically similar operating conditions were achieved by driving the rotor at a speed appropriate to equality of Reynolds number at a given operating condition. The blades of the rotor were constructed from stainless steel sheet but the end walls and the surrounding casing were constructed from perspex sheet to allow maximum light transmission for the purposes of observation and photography. Figure 5 shows the general layout of the model system. The vortex wall clearance and the circumferential extension of the rear wall could each be adjusted. It was on the basis of a previous flow visualization study with this easily adaptable arrangement along with the model aerodynamic studies reported in Ref. 2 that the large wind tunnel fan was designed.

Polystyrene beads of 0.5mm diameter were used as tracers after first soaking them in water to ensure a thoroughly wetted surface. Illumination was provided by three high-power, halogen strip lamps forming a 6mm slice of light transversely across the tank at the mid-span position of the rotor. A camera was mounted above the tank and was positioned directly above the rotor. By choosing a suitable shutter speed it was possible to record photographic streaks which represented the displacements of the beads and the corresponding directions of motion. Local velocities could then be estimated from the known camera shutter speed. Care was taken to ensure that the start and end of a streak was due solely to the chosen exposure time and not because the bead had a large axial velocity component which caused it to pass across the light beam. In this way the motion could be regarded as substantially two dimensional.

4. FLOW VISUALIZATION STUDY

The vortex wall and rear wall clearances of the model described in Section 3 were both set to 0.05 D_2 as it was unclear how these parameters would affect the conditions for dynamic similarity with the large rotor. Dynamic similarity with respect to other variables was maintained throughout all the tests.

For each resulting photograph, velocities in the various regions were determined from a knowledge of the camera shutter speed. The information extracted from each of the photographs took the form of:

(i)   the effective inflow arc,
(ii)   the general behaviour of the flow in the suction region,
(iii)   the flow velocities in the suction region,
(iv)   the size and velocity of the discharge jet over the rear wall,
(v)   the general behaviour of the flow in the interior region,
(vi)   the flow velocities in the interior region,
(vii)   the position of the vortex core,
(viii) the effective outflow arc,
(ix)   the general behaviour of the flow in the discharge region, and
(x)   the flow velocities in the discharge region.

From the resulting data it was possible to identify discrete zones of flow within the suction, interior and discharge regions as shown in Fig. 6.

The zones identified within the suction region were:
(a)   an inflow zone covering an arc beginning at the vortex wall,
(b)   a discharge jet from the rotor interior covering an arc beginning at the leading edge of the rear wall, and
(c)   a zone of entrained flow resulting from (b).

The zones identified in the interior region were:
(d)   a forced vortex core,
(e)   a recirculating flow return path from the discharge region,
(f)   a return flow path from the discharge region below the vortex wall,
(g)   a throughflow path,
(h)   a throughflow path from the suction region to the discharge jet over the rear wall, and
(i)   a low energy random zone.

The zones identified in the discharge region were:
(j)   a turbulent recirculation zone from the fan interior,
(k)   a diffusing throughflow zone, and
(l)   a flow path under the vortex wall returning essentially laminar flow to the fan.

The size of these zones and the associated velocities were found to be entirely dependent on the flow rate passing through the fan. Several casing configurations were examined but here we shall deal primarily with the geometry relating to the full scale wind tunnel fan having the 20°, constant radius extension above the rear wall.

For the fan operating under medium throttle conditions the flow in the suction region exhibited the three regions mentioned previously. Figure 7 shows the high velocity region close to the vortex wall where the majority of the flow enters the fan (region a), with velocities in this region estimated at $0.5u_2$. The geometric suction arc consists of 80% inflow with the remainder comprising the jet region b and its associated entrainment c. The velocity of the flow within the jet region is the order of the blade speed, showing clearly that the origin of the flow lies within the fan interior. The interior flow clearly shows the vortex core (region d) and the turbulent low energy region diametrically opposite (region i). In Fig.7 the outflow arc covers 65% of the geometric arc before meeting the recirculation region (region j) where vortices are seen to be shed from the main vortex core. The flow under the vortex wall is returning towards the fan (region ℓ). The velocities in the discharge region are about $3.0u_2$ (region k). As the fan outflow was throttled, the vortex moved by about 15° peripherally towards the rear wall but did not move significantly in a radial direction. Figure 8 is a high contrast, slow shutter speed photograph which shows the vortex core and a surrounding fainter region which corresponds to the flow returning from the discharge region below the vortex wall (region e).

Figure 9 illustrates the 'zero' flow criterion and shows the large recirculating region in the fan discharge (region j). It should be understood that zero flow relative to the fan cannot exist by throttling the outlet duct, as flow is always maintained through the fan owing to recirculation within the duct. A true zero flow condition can be imposed with a damper installed adjacent to the fan outlet. The vortex then moves to the centre of the rotor and becomes a forced vortex. The suction region velocities for a throttled fan are little different from those of the full flow condition. However, the inflow arc then diminishes to 50% of the geometric

arc with the rear wall jet region becoming increasingly dominant as it contains flow velocities of around $3.0u_2$. This jet region appears to be a major source of losses and hence poor efficiency of cross flow fans. On removing the 20° extension to the rear wall the jet region became more extensive and contained flow velocities lower than those previously recorded. Furthermore, the total inflow arc was somewhat smaller than that observed with the 20° extension. When the rear wall extension was set at 50° the jet became smaller but flow velocities higher. The total inflow arc was also smaller than the 20° extension case. Figures 10 and 11 show these two cases at 'zero' flow where they were found to be most dominant.

Table 2 summarizes the photographic records taken for the 0°, 20° and 50° extensions to the rear wall, with specific parameters labelled on Fig. 6. Figure 12 shows a more general view of the total flow fields mentioned previously and clearly indicates that the cause of pulsations found during the use of many of these units stems from the shed vortices and recirculation in the outlet duct. The flow visualization reveals that the interior flow field is rather different from those proposed in mathematical models and this divergence will be discussed later. The disturbed region within the impeller was always most predominant under low throttle conditions and the pressure distributions in the full scale wind tunnel fan showed similar trends.

5. AERODYNAMIC MEASUREMENTS

The results of traverses inside the rotor of the wind tunnel fan were related to a polar coordinate system located on the rotor centre-line, as shown in Fig. 13. Readings were taken at a number of r, θ grid coordinates using an improved 3-hole yaw probe. The probe was fixed to the end of a variable geometry 'Z' drive, with one arm concentric with the shaft of the fan, so that any radial location at mid-span could be adopted. Yawing was effected through a series of bevel gears attached to the hollow shafts which carried the pressure tubes. Measures were obtained of:

(i)   the angle of the flow relative to a radial line between the fan centre-line and the probe head,

(ii)   the velocity of the flow, and

(iii) the total pressure.

For a comparison with previous work the streamline pattern in the rotor was required. Figure 14 shows two adjacent streamlines associated with stream functions ψ_1 and ψ_2, with local velocities of q_1 and q_2 and making angles of θ_1 and θ_2 with respect to a radial line in the coordinate system. The streamlines are separated by the radial distance Δr. By definition,

$$\psi_2 = \psi_1 + \bar{u}d_n$$

where, d_n is the normal distance between the streamlines, and

$$\bar{u} = \tfrac{1}{2}\{q_1\sin(\theta + \theta_1) + q_2\sin(\theta + \theta_2)\}$$

Therefore,

$$\psi_2 = \psi_1 + \tfrac{1}{2}\{q_1\sin(\theta + \theta_1) + q_2\sin(\theta + \theta_2) \}\Delta r$$

and the stream function for the streamline crossing the rotor axis was arbitrarily chosen to be zero. The radial and tangential components of the velocities may be related to the stream function by the expressions,

$$\frac{\partial \psi}{\partial \theta} = - rV_r \qquad\qquad (1)$$

and

$$\frac{\partial \psi}{\partial r} = V_\theta \qquad\qquad (2)$$

From the experimental results, all the velocity and direction data were transformed into radial and tangential components, so that the above expressions could be used, in the form

$$\Delta\psi_\theta = -rV_r\Delta\theta \qquad\qquad (3)$$

and

$$\Delta\psi_r = V_\theta\Delta r \qquad\qquad (4)$$

The calculation procedure is as follows:

(i)   Plot V_r against θ, at all radii traversed (see Fig. 15 for $\Phi = 0.8$).

(ii)   Plot V_θ against r, at all peripheral positions traversed (see Fig. 16).

(iii) Begin the calculation procedure on the fan centre line at $\psi = 0$, designated coordinate r(0), θ(0).

(iv)   Using eqn (4) find the change in stream function between r(0), θ(0) and r(1), θ(270°), i.e. $\Delta\psi_1$.

(v)   Again using eqn (4) find the change in stream function between r(0), θ(0) and r(1), θ(275°), i.e. $\Delta\psi_2$.

(vi)   Using eqn (3) find the change in stream function between r(1), θ(270°) and r(1), θ(275°), i.e. $\Delta\psi_3$.

(vii) Two values of stream function are then found at coordinate r(1), θ(275°), and these are then averaged, e.g. at r(1), θ(275°)

$$\psi = \tfrac{1}{2}(\Delta\psi_1 + \Delta\psi_2 + \Delta\psi_3).$$

(viii) This method is repeated as the first radius r(1) is scanned ending finally at θ(270°) which is averaged with $\Delta\psi_1$. The second radius r(2) is treated similarly except that the radial changes in stream function derived from eqn (4) are added to those present on the first radius r(1) and so on.

(ix)   Curves are then drawn of ψ against r for constant θ and ψ against θ for constant r as shown in Figs 17 and 18, for example, from which coordinates are extracted for the final flow diagrams, as shown in Figs 19(a)-(e) for $\Phi = 0.4$ to 0.8.

Total pressures were measured inside the rotor and then used to form the dimensionless total pressure coefficient

$$\tilde{t} = (p_t - p_{to})/\tfrac{1}{2}\rho u_2^2 \tag{5}$$

Results are presented in Figs 20 (a)-(c) which indicate the locations and ranges of $\tilde{t}$ for three values of Φ. The data show that first, the total pressure along a particular streamline remains constant as it should, of course, and second, an indication of the type of vortex flow in existence may be established as follows. The pressure variation perpendicular to a streamline is given by

$$\frac{\partial p_s}{\partial r} = \rho \frac{V_\theta^2}{r} \tag{6}$$

For a free vortex (irrotational flow);

$$rV_\theta = \text{constant}, \; K \tag{7}$$

so that eqn (6) becomes

$$\frac{\partial p_s}{\partial r} = \rho \frac{K^2}{r^3} \tag{8}$$

Integration with respect to r gives

$$p_s = -\frac{\rho K^2}{2r^2} + \text{constant} \tag{9}$$

Now

$$p_t = p_s + \tfrac{1}{2}\rho V_\theta^2$$

$$= \frac{-\rho K^2}{2r^2} + \tfrac{1}{2}\rho\left(\frac{K}{r}\right)^2 + \text{constant} \tag{10}$$

and so in a free vortex p_t is constant. For a forced vortex

$$V_\theta = r\omega \tag{11}$$

and it is easy to show that

$$p_t = \rho V_\theta^2 + \text{constant} \tag{12}$$

Figure 21 shows typical velocity and pressure distributions in the rotor for the expected Rankine type vortex along with some measured data for velocity.

The conclusions from Figs 19-21 may now be summarized.

(a) For all flow rates, a Rankine type vortex was present within the rotor.

(b) The dimensionless total pressure was severely depressed in the vicinity of the vortex core and became further depressed as the flow rate increased and the vortex strengthened.

(c) A region of depressed total head (low energy) was present almost diametrically opposite that of the vortex core, which became more depressed and larger in area as the flow rate increased (see Section 4 for confirmation).

(d) The streamlines do not remain concentric with the vortex core as the fan is traversed radially. They are seen to flatten and indeed exhibit reversed curvature towards the rear wall.

(e) The streamlines indicate a general acceleration of the flow across the fan interior.

(f) The spacings between the streamlines yield a velocity profile across a diameter, including the vortex core, which has a peak at the boundary between the free and forced vortex regions and progressively falls towards the rear wall side.

(g) For $\phi = 0.8$ the velocities in the quadrant containing the vortex core are higher than those for $\phi = 0.4$, whereas the velocities in the opposite quadrant are similar for both flow rates.

(h) The position of the vortex core changed little in the range $\phi = 0.5$ to 0.8 but began to move peripherally and radially in the range $\phi = 0.4$ to 0.5.

6.   THEORY

Only a brief summary of the theory of cross flow fans is given here. A more comprehensive summary will be available shortly (Ref. 14). Notable work in the past has been undertaken by, for example, Coester (Ref. 15) who devised the first analysis, Ilberg and Sadeh (Ref. 16) and Moore (Ref. 17). These theories were formulated for a 'one-flow' situation and therefore could not be extended to overall performance prediction.

The work of Ikegami and Murata (Ref. 8) however, provided an inviscid flow analysis based on rotor geometry and a flow field which allowed mobility of the vortex within the impeller. Characteristics were deduced for a cross flow fan which consisted of a simple linear casing acting as a dividing streamline to separate the suction and discharge regions, and an impeller with an infinite number of blades. Laplace's equation was applied to the interior flow which was modelled by including a second vortex of equal strength Γ and direction as the internal vortex but located outside the impeller as shown in Fig. 22. The stream function for this combination can be expressed in the form

$$\psi = \frac{-\Gamma}{4\pi} \ln \left\{ (r^2 + a^2 r_1^2 + 2arr_1\cos\theta)(r + \frac{r_1^2}{a^2} + \frac{2rr_1}{a} \cos \theta) \right\} \tag{13}$$

The vortex strength

$$\Gamma = 2\pi r_1 u_1 \tag{14}$$

since the flow velocity at the rotor periphery equals the rotor velocity. The flows on the suction side and within the impeller are related by virtue of the expression

$$\psi_{r = r_1} = \psi_{r = r_2} + \text{constant} \tag{15}$$

The flow rate per unit length can be expressed in the form

$$Q = \psi_{\theta = 0} - \psi_{\theta = \pi} \tag{16}$$

so that in dimensionless terms

$$\phi = \frac{Q}{2r_2 u_2} = \left(\frac{r_1}{r_2}\right)^2 \ln \left\{ \frac{1 + a}{1 - a} \right\} \tag{17}$$

As the impeller does not impart uniform energy transfer to each streamline, the pressure rise was evaluated as a mean value of energy transfer to each streamline passing through the rotor. The dimensionless mean total pressure coefficient was found to be

$$\Psi_t = \frac{\bar{P}_t}{\frac{1}{2}\rho u_2^2} = \frac{2a}{\ln\left(\frac{1+a}{1-a}\right)} \int_0^\pi \left\{ 1 + \left(\frac{r_1}{r_2}\right)^2 \left(\frac{2a\sin\theta}{1+a^2-2a\cos\theta}\cot\beta_2\right.\right.$$

$$\left.\left. -2\sum_{n=1}^{15} n k_n' \sin n\theta\right)\left(\frac{\sin\theta}{1+a^2-2a\cos\theta}\right)\right\} \, d\theta \qquad (18)$$

and values of Φ and Ψ_t were plotted to show the effect of changes in the rotor geometry and the radial vortex location.

Although the mathematical analysis presented in Ref. 8 for the radial motion of the vortex was correct, a number of serious computation errors occurred especially for large values of a ; matters became worse when peripheral movement of the vortex was permitted. The authors have corrected these errors by including higher harmonics in eqn (18) to produce the data in Fig. 23 . The theory of Ikegami and Murata (Ref. 8) has been refined by including the effects of blade number and blade thickness-to-chord ratio. Equation (15) is replaced by

$$B\psi_{r = r_1} = \psi_{r = r_2} + \text{constant} \qquad (19)$$

where B is a 'blockage' factor. Figure 24 shows that blades of slender profile are associated with a high pressure rise; the number of blades has a small effect, as shown in Fig. 25.

The flow visualization and aerodynamics studies showed that the curvature of the streamlines within the rotor tended to increase more rapidly than expected across a radial line through the vortex core; in some cases a reversed curvature occurred towards the rear wall leading edge. To model this reversed curvature a source and a sink were positioned opposite the vortex core as shown in Fig. 26. The new expression for the stream function in the internal region was the summation of $\psi_{ss} = m(\theta_1 - \theta_2)/2\pi$ with ψ from eqn (13). To satisfy the boundary condition on the rotor periphery the vortex strength Γ varied with position as shown in Fig. 27. The resulting performance mesh was not significantly different to that in Fig. 23. The vortex strength varied considerably for peripheral movement although not for radial movement apart from the region close to the inner periphery of the blade row. An example of the modified flow diagram is given in Fig. 28.

Flow losses associated with cross flow fans fall into two categories;
(i)   shock losses at blade leading edge owing to the disparity between the inlet relative flow angle and the blade angle β_2, and
(ii)   losses within the vortex itself.
Shock losses were examined by using Laplace's equation for the velocities in the suction region. Figure 29 shows the variation of the tangential and radial velocities around the outer periphery of the rotor, together with the deviation of the relative velocity from the blade angle. It is seen that the majority of losses occur near the vortex wall, where the radial velocities are highest. Vortex losses were estimated from the energy losses of an element within the flow. Neglecting radial flow the total energy loss was found to be $E = 4\pi\mu V_{\theta a}$ where $V_{\theta a}$ is the tangential velocity component at the interface between the free and forced vortex zones, but the estimate appeared unrealistically low. When radial velocities were included, terms containing fluid density entered the original equations as a result of tangential pressure gradients. The size of this term suggests that momentum changes could account for a large proportion of the energy dissipated within a cross flow fan.

7.   CONCLUSIONS

The naturally formed vortex changes intensity and size according to its location. This location could be changed by sending a wake, generated outside the rotor, through the machine. The system resistance (which was unaltered) was not therefore the only agent responsible for vortex position. The internal streamlines are not circular. A Rankine combined vortex has been confirmed from the total pressure distribution in the rotor. For the present fan the vortex core is always close to the inner periphery. Important modifications to an existing theory allow for some losses, variable vortex strength and reflex curvature of streamlines in the suction region of the rotor.

REFERENCES

1. Clayton, B.R.: "A review and appraisal of cross flow fans". Building Services Engineer (I.H.V.E.), 42, Jan. 1975, pp 230-247.

2. Holgate, M.J. and Haines, P.: "Scaling of cross flow fans - an experimental comparison". Proc. I. Mech. E. Conference on Scaling for Performance Prediction in Rotodynamic Machines, Stirling, 1977.

3. Yamafuji, K.: "Studies on the flow of cross-flow impellers (1st Report, Experimental study)". Bull. Jap. Soc. Mech. Engrs, 18, Sept.1975, pp 1018-1025.

4. Yamafuji, K.:"Studies on the flow of cross-flow impellers (2nd Report, Analytical study)". Bull. Jap. Soc. Mech. Engrs, 18, Dec.1975, pp 1425-1431.

5. Murata, S. and Nishihara, K.: "An experimental study of cross flow fan (1st Report, Effects of housing geometry on the fan performance)". Bull. Jap. Soc. Mech. Engrs, 19, Mar. 1976, pp 314-321.

6. Murata, S. and Nishihara, K. "An experimental study of cross flow fan (2nd Report, Movements of eccentric vortex inside impeller)". Bull. Jap. Soc. Mech. Engrs, 19, Mar. 1976, pp 322-329.

7. Murata, S., Ogawa, T., Shimizu, I., Nishihara, K. and Kinoshita, K.: "A study of cross flow fan with inner guide apparatus". Bull. Jap. Soc. Mech. Engrs, 21, Apr. 1978, pp 681-688.

8. Ikegami, H. and Murata, S.: "A study of the cross flow fan: Part 1, A theoretical analysis". Technology Rep. Osaka Univ., 16, 1966, No. 731.

9. Eck, B.: " Fans". Oxford, Pergamon Press, 1973, pp 156-182.

10. Ikegami, H. and Murata, S.: "Experimental study of the cross flow fan". Science of Machine, 18, 3, 1966, pp 557-566. (In Japanese)

11. Porter, A.M. and Markland, E.:"A study of the cross flow fan". Jour. Mech. Eng. Sci., 12, 6, 1970, pp 421-431.

12. Preszler, L. and Lajos, T.:"Experiments for the development of the tangential flow fan". Proc. 4th. Conf. on Fluid Machinery (Budapest, 1972), Akadémiai Kiadó, pp 1071-1082.

13. Clayton, B.R. and Massey, B.S.: "Flow visualization in water: a review of techniques". J. Sci. Instrum., 44, 1967, pp 2-11.

14. Tuckey, P.R. and Clayton, B.R.: Ph.D Thesis, University of Durham, in preparation.

15. Coester, R.: "Theoretische und experimentelle untersuchungen an querstromgeblasen". Mitt. aus dem Institut für Aerodyn., E.T.H., Zurich, No. 28, 1959. (In German)

16. Ilberg, H. and Sadeh, W.Z.: "Flow theory and performance of tangential fans". Proc. Inst. Mech. Engrs, London, 180, 1965-66, pp 481-496.

17. Moore, A.: "The tangential fan - analysis and design". Conference on Fan Technology and Practice, Institution of Mechanical Engineers, London, April 1972.

Table 1 Rotor geometry

Blade angles; $\beta_1 = 90°$, $\beta_2 = 26°$
Blade profile; circular arc
Number of blades; N = 24
Diameter ratio; $D_1/D_2 = 0.78$
Length to diameter ratio; $L/D_2 = 1.6$

Table 2 Summary of photographic records

α (deg)	Throttle (increases with more*)	Arc$_{in}$ (deg)	V$_{in}$	V$_{jet}$	h$_{jet}$	θ$_{vortex}$ (deg)	vortex size	θ$_d$ (deg)	V$_{int}$	Arc$_{out}$ (deg)	V$_{out}$	outflow quality (the more* the better)
0	*	154	$0.75u_2$	$1.0u_2$	$0.2r_2$	275	$0.17r_2$	81	-	96	$3.0u_2$	****
0	**	131	$0.50u_2$	$1.5u_2$	$0.4r_2$	295	$0.30r_2$	62	$1.7u_2$	84	$2.0u_2$	*****
0	***	116	$0.63u_2$	$1.0u_2$	$0.51r_2$	289	$0.50r_2$	61	$3.0u_2$	71	$1.7u_2$	**
20	*	158	$0.48u_2$	$1.0u_2$	$0.19r_2$	279	$0.37r_2$	95	$3.0u_2$	91	$3.0u_2$	***
20	**	128	$0.58u_2$	-	$0.25r_2$	290	$0.50r_2$	65	$1.5u_2$	80	$2.5u_2$	**
20	***	101	$0.57u_2$	$2.0u_2$	$0.31r_2$	292	-	75	$1.0u_2$	72	$3.0u_2$	***
50	*	153	$0.70u_2$	$0.35u_2$	v. small	281	-	75	-	91	$3.6u_2$	**
50	**	121	$0.63u_2$	$0.60u_2$	$0.21r_2$	290	-	57	-	84	$3.0u_2$	***
50	***	99	$0.70u_2$	$2.5u_2$	$0.38r_2$	292	-	29	-	71	$3.0u_2$	*

Fig. 1 Layout of aerodynamic test rig
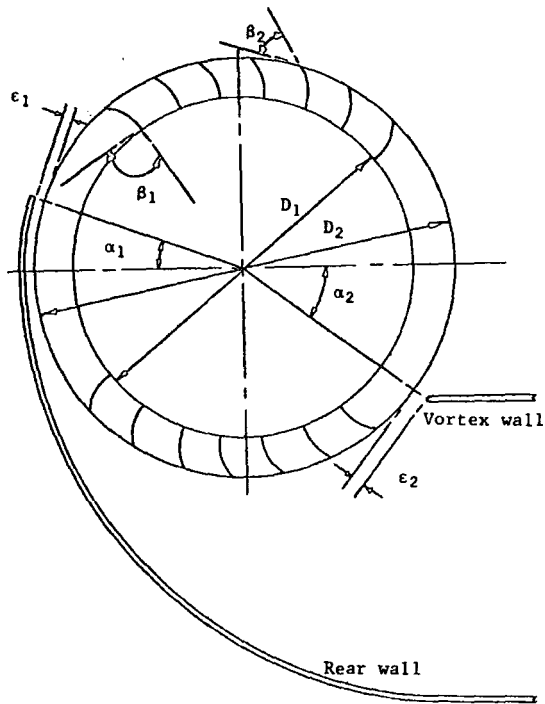
Fig. 2   Geometry of the cross flow fan
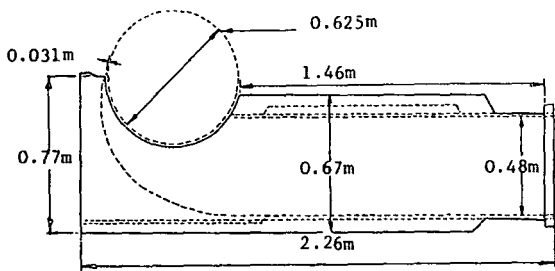
Fig. 3   Geometry of fan under test
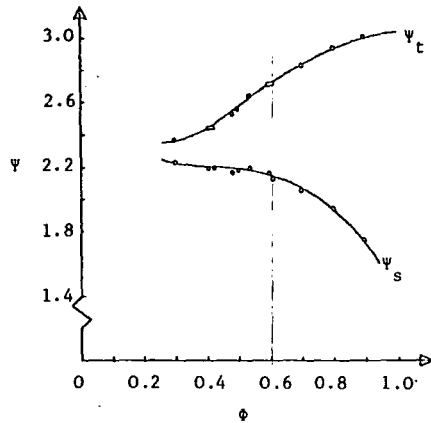
Fig. 4   Fan performance curves
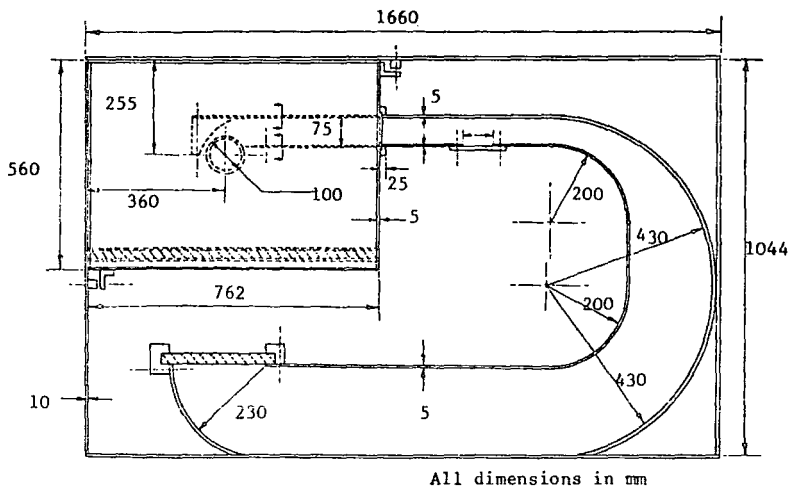
Fig. 5   Layout of hydro-
dynamic rig

All dimensions in mm

419
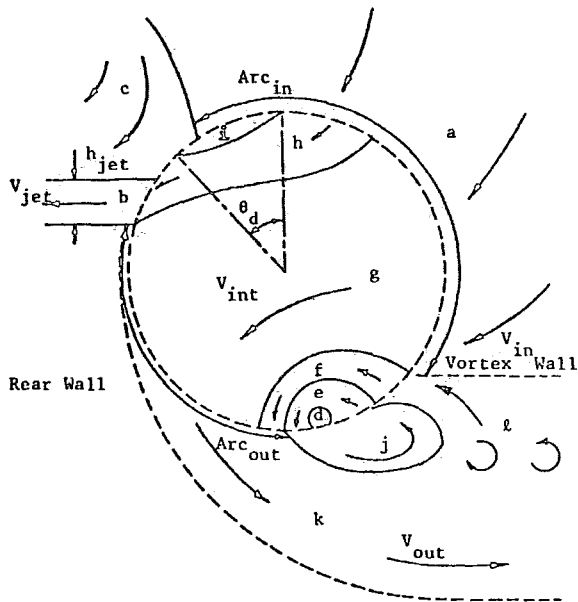
Fig. 6 Regions of flow
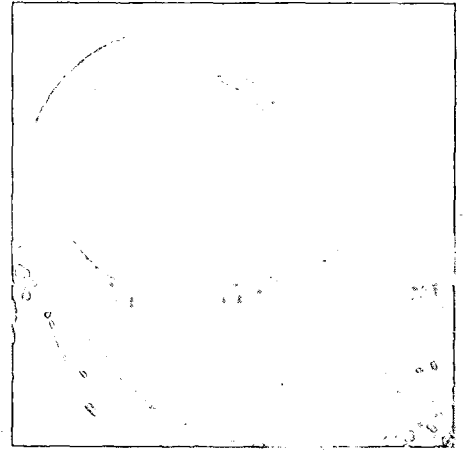
Fig. 7

Fig. 8

Fig. 9
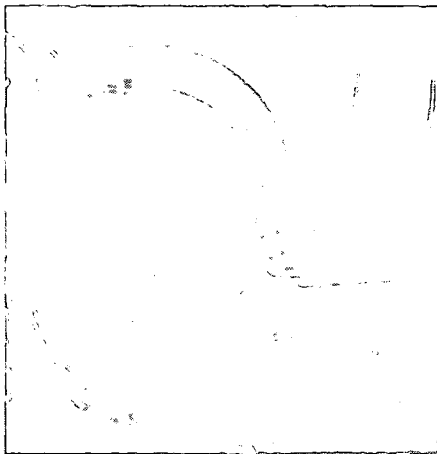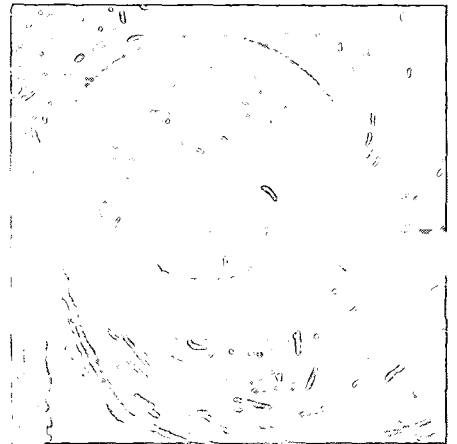
Fig. 10
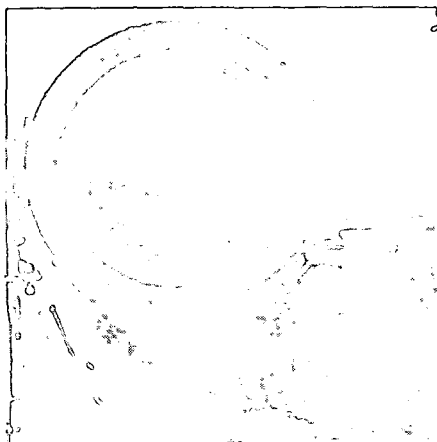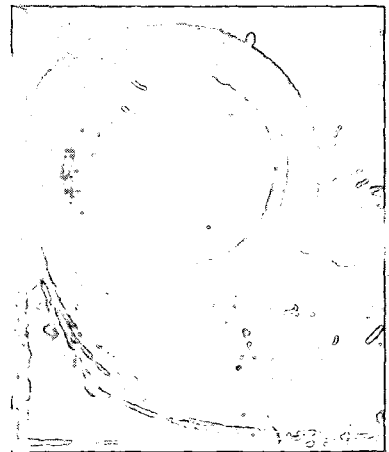
Fig. 11

Figs. 7-11 Show flow behaviour under different throttle conditions as described in text

420
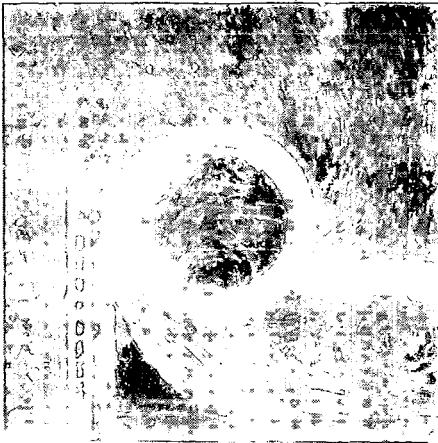
Fig. 12 General flow condition
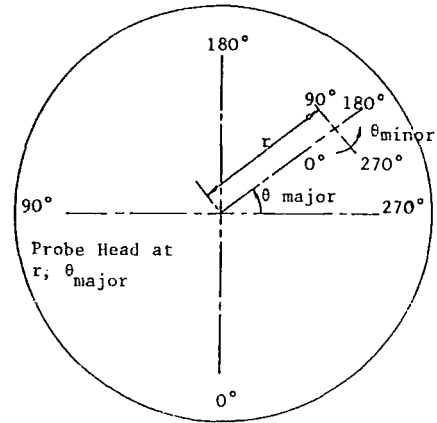
Fig. 13 Coordinate system
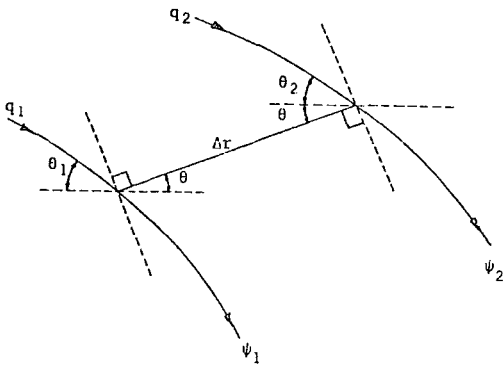
Fig. 14 Streamline geometry
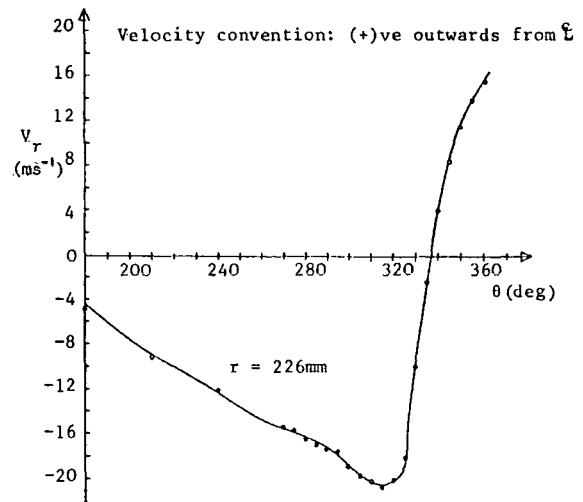
Fig. 15 Variation of radial velocity for $\Phi = 0.8$
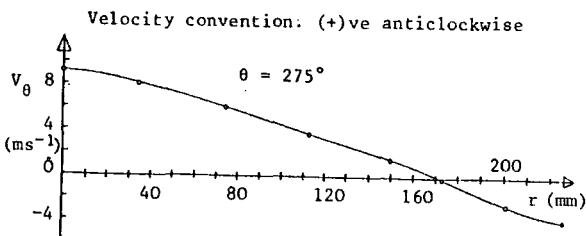
Fig. 16 Variation of tangential velocity for $\Phi = 0.8$
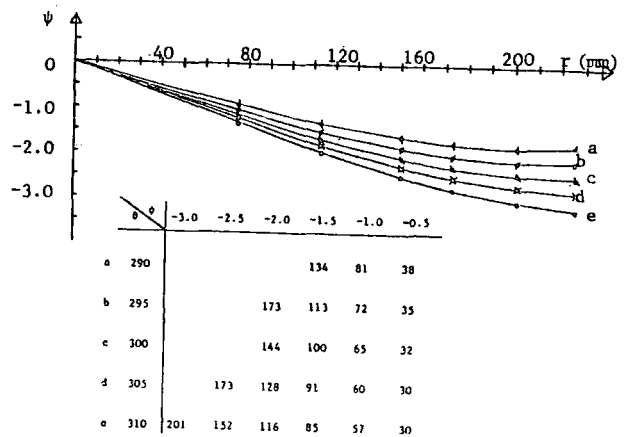
Fig. 17 Variation of ψ with r for given angle θ; $\Phi = 0.8$

421

Fig. 18 Variation of ψ with θ for
given radius r; Φ = 0.8

(a)

Φ = 0.8

(b)

Φ = 0.7

(c)

Φ = 0.6

(d)

Φ = 0.5

(e)

Φ = 0.4
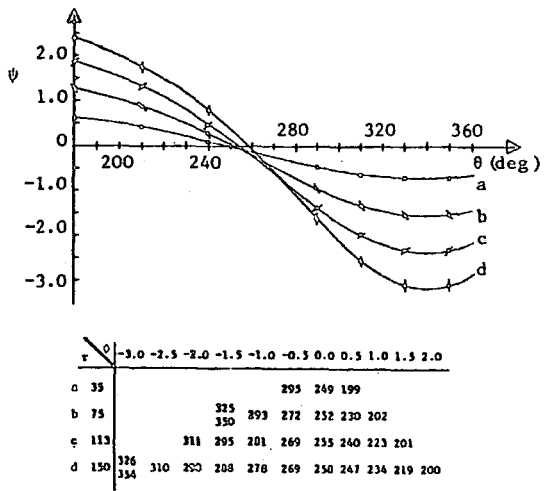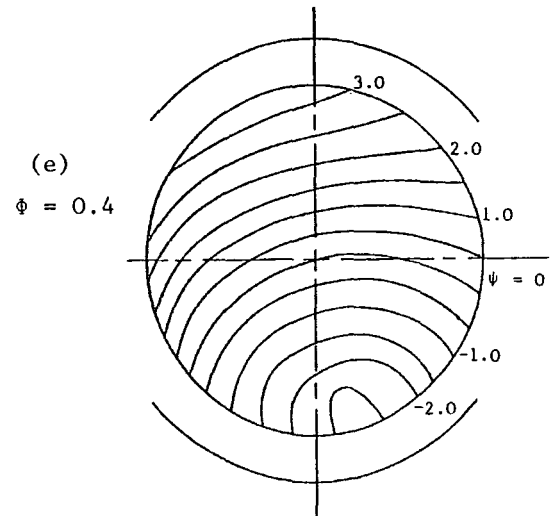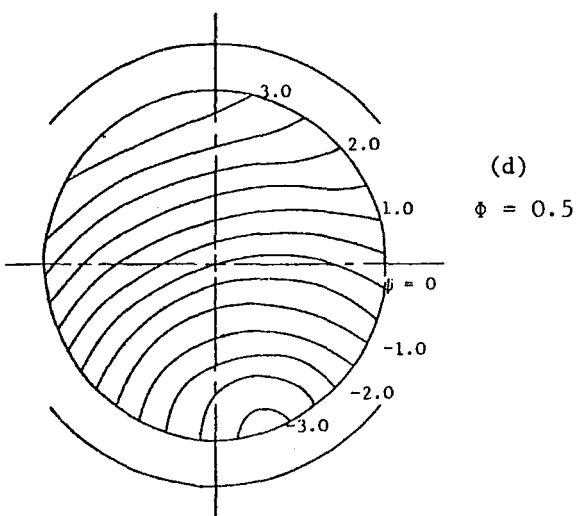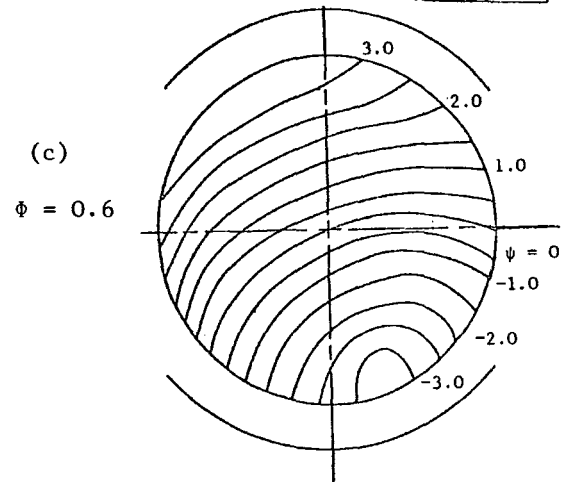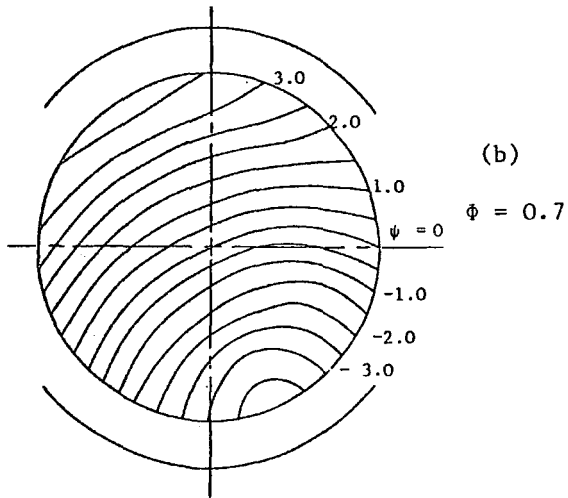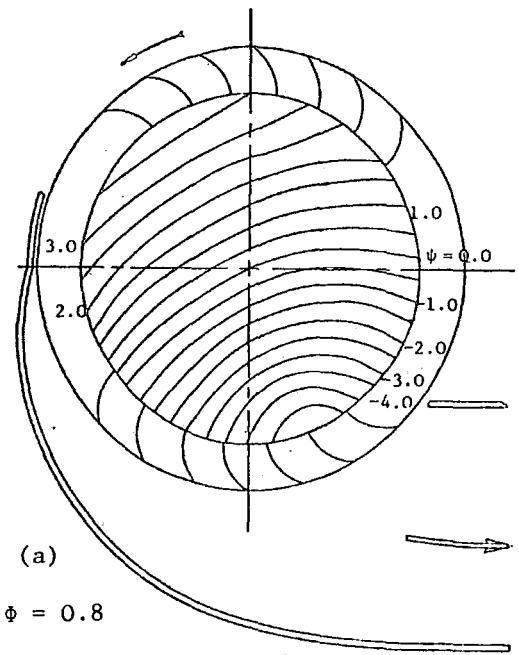
Fig. 19 (a) - (e) Streamline patterns   deduced from pitot traverses

(a)

$\phi = 0.8$

Vortex Wall

(b)

$\phi = 0.6$

Vortex Wall

(c)

$\phi = 0.4$

Vortex Wall
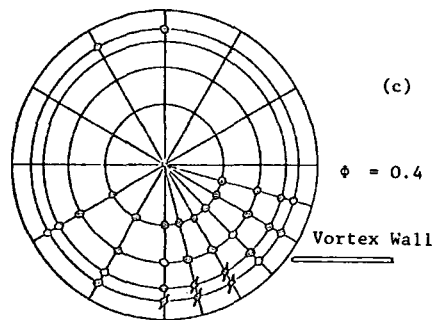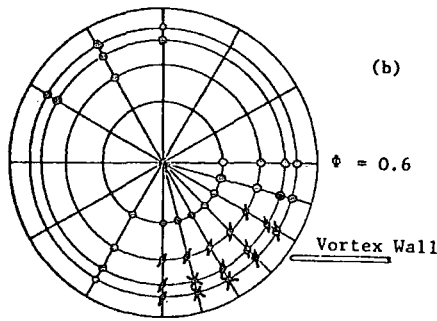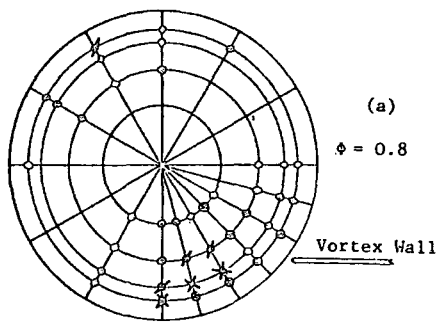
Symbol	$\tilde{t}$ Range
Nothing	0
o	-2 to 0
ϖ	-4 to -2
$\varkappa$	-6 to -4
$\circledcirc$	-8 to -6

Fig. 20 Distribution of total pressure coefficient $\tilde{t}$
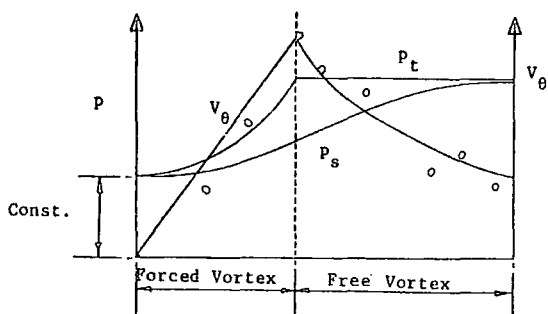
Fig. 21 Theoretical velocity and pressure distributions in a Rankine vortex
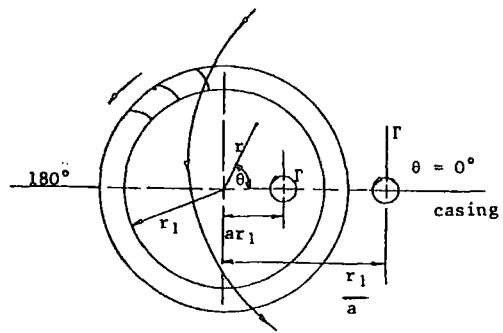
Fig. 22 Flow model used in Ref. 8
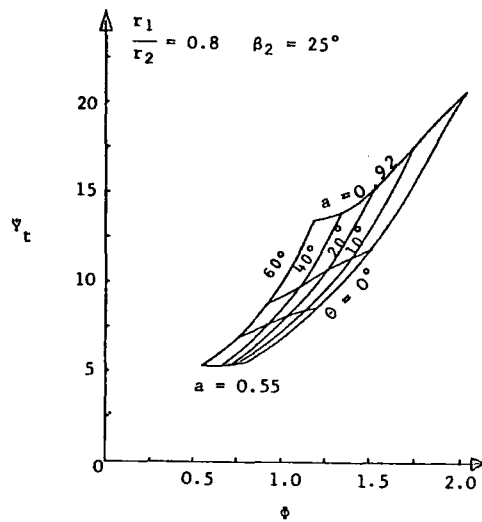
Fig. 23 Theoretical performance
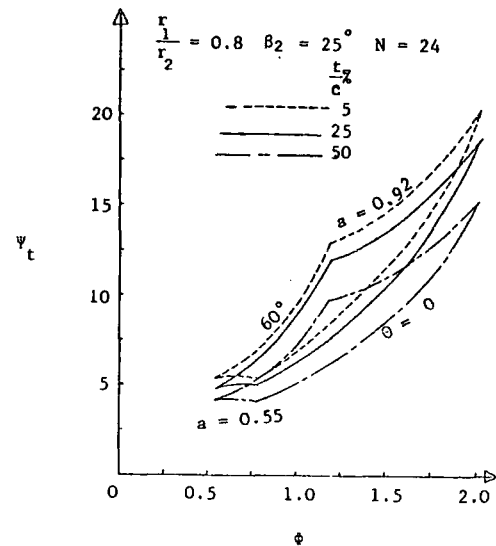
Fig. 24 Effect of blade thickness on theoretical performance

423
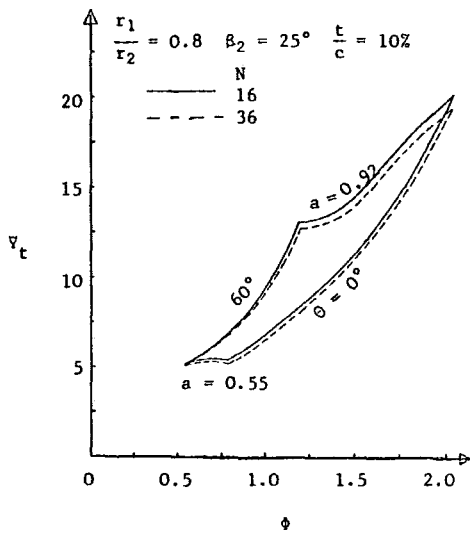
Fig. 25 Effect of blade number on theoretical performance
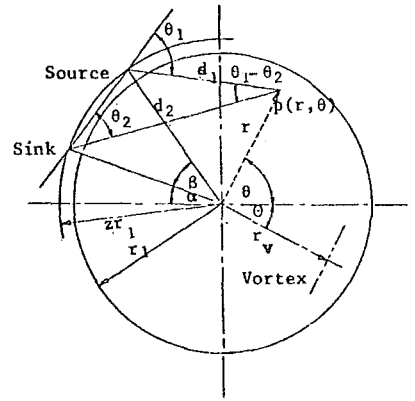

Fig. 26 Added source and sink to modify theoretical internal flow
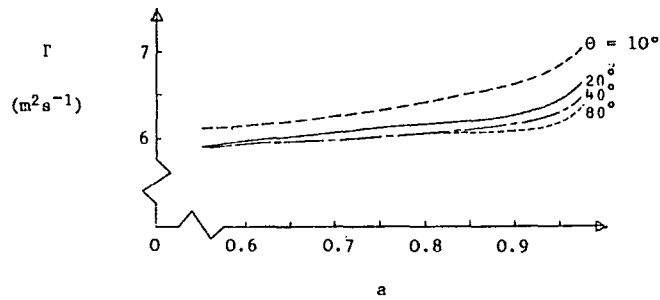
Fig. 27 Variation of vortex strength in rotor
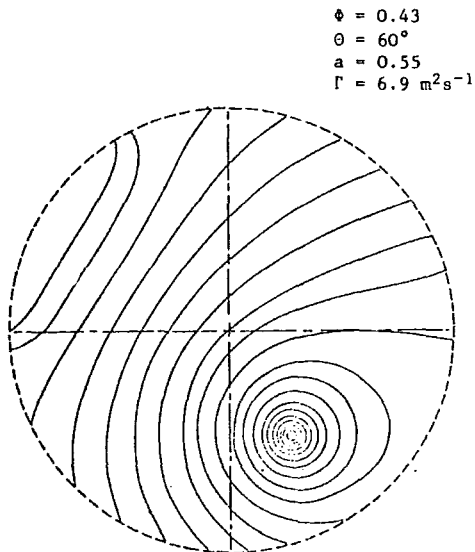
Fig. 28 Flow field with modific-
ations of Fig. 26
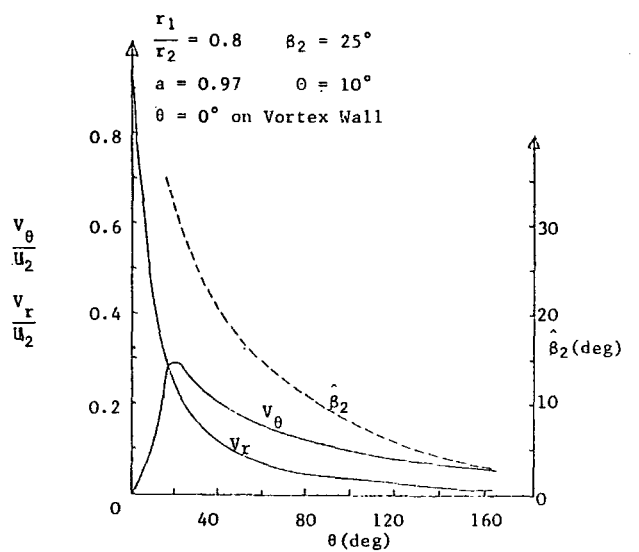
Fig. 29 Variation of velocity and
deviation in suction region